Department of Radio Science and Engineering

Microwave radiometry of snow covered terrain and calibration of an interferometric radiometer

Juha Lemmetyinen

Aalto University

DOCTORAL DISSERTATIONS

Aalto University publication series
DOCTORAL DISSERTATIONS 142/2012

Microwave radiometry of snow covered terrain and calibration of an interferometric radiometer

Juha Lemmetyinen

A doctoral dissertation completed for the degree of Doctor of Science (Technology) to be defended, with the permission of the Aalto University School of Electrical Engineering, at a public examination held at the lecture hall S1 of the school on 27 November 2012 at 12.

Aalto University
School of Electrical Engineering
Department of Radio Science and Engineering

Supervising professor
Prof. Martti Hallikainen, Aalto University

Thesis advisor
Prof. Jouni Pulliainen, Finnish Meteorological Institute

Preliminary examiners
Prof. Paolo Pampaloni, Consiglio Nazionale delle Richerche, Instituto di Fisica Applicata "Nello Carrara", Italy.
Prof. Marco Tedesco, City College of New York, USA.

Opponent
Prof. Leung Tsang, University of Washington, USA.

Aalto University publication series
DOCTORAL DISSERTATIONS 142/2012

ISBN 978-952-60-4843-7 (printed)
ISBN 978-952-60-4844-4 (pdf)
ISSN-L 1799-4934
ISSN 1799-4934 (printed)
ISSN 1799-4942 (pdf)
http://urn.fi/URN:ISBN:978-952-60-4844-4

Unigrafia Oy
Helsinki 2012

Finland

441 697
Printed matter

Aalto University

Aalto University, P.O. Box 11000, FI-00076 Aalto www.aalto.fi

Abstract

Author
Juha Lemmetyinen

Name of the doctoral dissertation
Microwave radiometry of snow covered terrain and calibration of an interferometric radiometer

Publisher School of Electrical Engineering

Unit Department of Radio Science and Engineering

Series Aalto University publication series DOCTORAL DISSERTATIONS 142/2012

Field of research Remote Sensing and Space Technology

Manuscript submitted 15 May 2012 **Date of the defence** 27 November 2012

Permission to publish granted (date) 8 August 2012 **Language** English

☐ **Monograph** ☒ **Article dissertation (summary + original articles)**

Abstract

Remote sensing of the Earth using microwave radiometers is an important tool for the monitoring of diverse environmental processes from space. Passive microwave instruments are used, amongst other applications, for the monitoring of ocean processes, the properties of soil and vegetation, and different aspects of the Earth's cryosphere. Compared to optical instrumentation, passive microwaves provide the advantage of being largely insensitive to atmospheric and lighting conditions. However, the radiometers typically suffer from a poor spatial resolution, which makes the interpretation of observations of heterogeneous areas challenging. An important part in understanding passive microwave signatures of the Earth's surface is the development of emission models, linking the observations to the physical properties of the target. Advanced models can be further applied to account for the effects of varying vegetation and land cover in the observation.

The first part of this thesis dissertation describes the development, validation and application of a radiative transfer based model for the simulation of microwave emission from snow covered terrain. The model is an improvement of an existing model published in literature, introducing the possibility to account for the vertical layering of snow and ice structures in the simulation. The modified model is verified against experimental observations from ground based and airborne radiometer instruments, and finally applied for the retrieval of snow cover parameters from space.

Calibration of radiometer instruments is a prerequisite for reliable observations. Calibration of space-borne radiometers is particularly challenging due to the typically high sensitivity of instrumentation to changes in environmental conditions. In the second part of this dissertation, the calibration method for a novel type of radiometer instrument, the first interferometric radiometer using aperture synthesis in space, is presented. Specifically, on-ground characterization of the calibration subsystem of the instrument is described, including an analysis of the effects of the characterization errors on the final performance of the instrument.

Keywords Passive microwave remote sensing, radiometer calibration, snow cover

ISBN (printed) 978-952-60-4843-7 **ISBN (pdf)** 978-952-60-4844-4

ISSN-L 1799-4934 **ISSN (printed)** 1799-4934 **ISSN (pdf)** 1799-4942

Location of publisher Espoo **Location of printing** Helsinki **Year** 2012

Pages 250 **urn** http://urn.fi/URN:ISBN:978-952-60-4844-4

A? Aalto-yliopisto

Aalto-yliopisto, PL 11000, 00076 Aalto www.aalto.fi

Tiivistelmä

Tekijä
Juha Lemmetyinen

Väitöskirjan nimi
Lumipeitteen kaukokartoitus mikroaaltoradiometreillä ja interferometrisen radiometrin kalibrointi

Julkaisija Sähkötekniikan korkeakoulu

Yksikkö Radiotieteen ja tekniikan laitos

Sarja Aalto University publication series DOCTORAL DISSERTATIONS 142/2012

Tutkimusala Kaukokartoitus ja avaruustekniikka

Käsikirjoituksen pvm 15.05.2012 **Väitöspäivä** 27.11.2012

Julkaisuluvan myöntämispäivä 08.08.2012 **Kieli** Englanti

☐ **Monografia** ☒ **Yhdistelmäväitöskirja (yhteenveto-osa + erillisartikkelit)**

Tiivistelmä

Maapallon kaukokartoitus mikroaaltoradiometreillä on käyttökelpoinen menetelmä eri ympäristötekijöiden seurannassa. Passiivisten mikroaaltolaitteiden mittauksia käytetään mm. valtamerten, kasviston sekä lumi- ja jääpeitteen havainnointiin. Verrattuna optisiin kaukokartoitusinstrumentteihin mikroaaltolaitteiden etuina ovat ilmakehän heikko vaikutus sekä riippumattomuus valaistusolosuhteista. Passiivisilla mikroaaltolaitteilla on kuitenkin vaatimaton spatiaalinen erottelukyky, mikä tekee heterogeenisten alueiden havaintojen tulkinnasta haastavaa; tähän tarvitaan maanpinnan tuottaman mikroaaltosäteilyn mallinnusta. Kehittyneiden mallien avulla voidaan myös kompensoida esimerkiksi heterogeenisten kasvillisuuden tai maaston vaikutusta havaintoihin.

Väitöskirjatyö kuvaa lumipeitteen mikroaaltoemissiota selittävän mallin kehitystä, malliennusteiden oikeellisuuden tarkastelua kokeellisin mittauksin sekä mallin soveltamista kaukokartoitushavaintojen tulkintaan. Kehitetty malli laajentaa aiempaa emissiomallia kuvaamaan myös eri kerrosrakenteiden vaikutusta lumen emissioon, mahdollistaen mm. lumipeitteisten järvien mikroaaltovasteen mallinnuksen. Laajennetun mallin ennusteita vertaillaan työssä sekä maan pinnalta että lentokoneesta mitattuihin radiometrihavaintoihin, sekä käytetään lopulta lumipeitteen ominaisuuksien tulkintaan satelliittihavainnoista.

Tärkeä edellytys kaukokartoitushavaintojen käytölle on niihin käytettyjen laitteiden kalibrointi. Satelliittiradiometrien kalibroinnin erityisenä haasteena on laitteiden suuri lämpötilariippuvuus. Väitöstyössä esitellään uudenlaisen kuvaavan radiometrijärjestelmän kalibrointimenetelmä. Osana väitöstyötä kehitettiin malli kalibrointijärjestelmän ominaisuuksien kuvaamiseen eri lämpötiloissa, sekä tutkittiin mallin epävarmuuksien vaikutusta radiometrin kuvanmuodostuksen luotettavuuteen.

Avainsanat Passiivinen mikroaaltokaukokartoitus, lumen vesiarvo, radiometrien kalibrointi

ISBN (painettu) 978-952-60-4843-7 **ISBN (pdf)** 978-952-60-4844-4

ISSN-L 1799-4934 **ISSN (painettu)** 1799-4934 **ISSN (pdf)** 1799-4942

Julkaisupaikka Espoo **Painopaikka** Helsinki **Vuosi** 2012

Sivumäärä 250 **urn** http://urn.fi/URN:ISBN:978-952-60-4844-4

Preface

The writing of this thesis, and completing the work that led to it, proved to be a considerable challenge for myself. However, I was lucky to be able to conduct my work in a resourceful environment, and benefit from the support of leading experts in the field of remote sensing. The structure and title of the thesis reflect the fact that the work consists of two separate, although interlinked subjects of radiometer calibration and the use of these instruments for the remote sensing of snow. The former part was conducted at the Laboratory of Space Technology of the Helsinki University of Technology (presently, the Remote Sensing and Space Technology Group at Aalto University), whereas the latter part was begun at the laboratory but finalized at the Finnish Meteorological Institute. This work was also supported by the Jenny and Antti Wihuri foundation, the Walter Ahlström foundation and Emil Aaltonen foundation.

I have received the help and assistance of numerous people in my research work, for which I wish to express my sincere gratitude. Firstly, I thank Professor Leung Tsang for taking up the task of reviewing my work and acting as the official opponent at the defense. I also wish to acknowledge Prof. Paolo Pampaloni and Prof. Marco Tedesco for their valuable and encouraging comments during the review process. I am deeply grateful to Prof. Martti Hallikainen for his supervision and help with this thesis, but also for creating an inspiring research atmosphere in the Laboratory of Space Technology, where I was hired first as a research assistant in 2001, and later as a researcher in 2004. In equal part, I thank Prof. Jouni Pulliainen for introducing me to the subject of remote sensing of snow cover, for acting as the principal advisor for the thesis and for many useful discussions on radiative transfer modeling.

I thank all my former colleagues at the Laboratory of Space Technology; in particular I wish to acknowledge Dr. Juha Kainulainen, Dr. Andreas Colliander and Dr. Janne Lahtinen for their support during the SMOS calibration subsystem test campaign, as well as extensive help and advice in writing my first journal articles; Mr. Jörgen Pihlflyckt, Mr. Pekka Rummukainen and Mr. Tuomo Auer for their considerable technical support; Lic. Sc. Simo Tauriainen for safe rides on the university research aircraft, and Dr. Marko Mäkynen, Lic. Sc. Juha-Petri Kärnä, Mr. Sami Kemppainen and Mr. Jaakko Seppänen for assistance in several research projects related to this thesis. Several people from the former company Ylinen Oyj. also supported this work during the time-consuming but

interesting SMOS CAS test campaigns, including Mr. Josu Uusitalo, Ms. Heli Greus, Mr. Nestori Fabritius, Mr. Mikael Levander and Mr. Ville Kangas.

I warmly thank my present colleagues Mr. Kimmo Rautiainen, Mr. Matias Takala, Dr. Kari Luojus, Mr. Juho Vehviläinen, Dr. Ali Nadir Arslan, Mr. Tuomo Smolander, Dr. Kirsti Kauristie and many others for a dynamic and supportive work environment at the FMI Helsinki office. I also thank Mrs. Anna Kontu, Ms. Hanne Suokanerva, Mrs. Riika Ylitalo, Mr. Markku Kivioja, Mr. Jyrki Mattanen and Mr. Markku Ahponen from the FMI Arctic Research centre in Sodankylä for their continuing scientific and technical support and enduring patience, as well as our able secretaries Mrs. Kirsi Kari, Mrs. Eeva Henttinen and Mrs. Riitta Aikio for assistance in practical and financial matters.

I am very grateful for the support I received from several international research associates, including Dr. Chris Derksen, Mr. Peter Toose, Dr. Claude Duguay, Dr. Andrew Rees and Mr. Grant Gunn, with whom I have had the pleasure of co-authoring several journal articles, three of which are also included as a part this thesis work. Special thanks go to Dr. Yubao Qiu, who volunteered to assist me in field work which led to publication no. 4 of this thesis. In addition I wish to acknowledge Dr. Manuel Martín-Neira, Dr. Dirk Schüttemeyer, Dr. Michael Kern, Dr. Matthias Drusch and Dr. Tania Casal from the European Space Agency for the numerous opportunities in participating in several SMOS- and snow remote sensing projects, which have both directly and indirectly helped to finalize this thesis. I also thank Dr. Andreas Wiesmann and Dr. Christian Mätzler for their expert advice and profound discussions on the microwave properties of snow.

I also thank my parents and my friends for their support, which has enabled and encouraged me to pursue a career in research. Finally, I thank my loving wife Sanna and our two boys for providing me with a true purpose in life.

In Helsinki, 17 October 2012

Juha Lemmetyinen

Table of Contents

Acronyms

AMSR-E	Advanced Microwave Scanning Radiometer for EOS
CAS	Calibration Subsystem
DMRT	Dense Media Radiative Transfer
ESA	European Space Agency
FMI	Finnish Meteorological Institute
FTR	Flat Target Response
LICEF	Light Weight Cost Effective (receiver)
MIRAS	Microwave Imaging Radiometer using Aperture Synthesis
NIR	Noise Injection Radiometer
NS	Noise Source
PD	Power Divider
PMS	Power Measurement System
SMOS	Soil Moisture and Ocean Salinity (ESA satellite mission)
SSM/I	Special Sensor Microwave/Imager
SWE	Snow Water Equivalent
TKK, HUT	Helsinki University of Technology

Symbols

α, β	Empirical parameters	-
β_μ	Fractional coverage of land cover μ	-
δ	Dirac delta function	-
$\Delta\theta_{kp}$	Uncertainty of baseline phase difference of receivers k and j	[deg]
Δf	Bandwidth	[Hz]
ΔG	RMS variation of system gain	-
ΔS_{jy}	Uncertainty of calibration network gain from source y to receiver j	[dB]
ΔT	Radiometer sensitivity	[K]
ΔT_G	Brightness temperature uncertainty due to receiver gain fluctuations	[K]
ΔT_N	Brightness temperature uncertainty due to noise fluctuations	[K]
ε	Permittivity	[F/m]
$\varepsilon_{i,t}$	Sum of model and observation errors	-
ϵ	Emissivity	-
θ, θ_s	Propagation angle	[deg]
θ_i	Incident angle	[deg]
θ_{qi}, θ_{qj}	Quadrature error of radiometers i and j.	[deg]
θ_{kq}, θ_{jq}	CAS signal path phase from source q to receivers k and j	[deg]
$\theta_{kj}^{'}$	Measured phase difference of correlated noise	[deg]
μ	Permeability	[N/A^2]
μ_{ij}	Normalized correlation coefficient	-
ξ, η	Direction cosines	-

λ	Wavelength	[m]
$\lambda^2_{d_{0,ref}}$	Variance of grain size value	[mm²]
κ_a	Absorption coefficient	-
κ_e	Extinction coefficient	-
κ_s	Scattering coefficient	-
ϱ	Charge density	[C/m³]
σ_d	Differential scattering cross section	[m²]
σ_i	Standard deviation of random errors	-
σ_s	Scattering cross section	[m²]
$\sigma_{ref,j}$	Standard deviation of model a priori parameters $\hat{x}_{ref,j}$	-
τ	Integration time	[s]
Ψ	Scattering phase function	-
ω	Angular frequency	[rad/s]
Ω_s	Solid angle for emitted power	[srad]
Ω_r	Solid angle for received power	[srad]
A_r	Receiver aperture	[m²]
A_s	Area of power source	[m²]
B	Bandwidth	[Hz]
$\mathbf{B}$	Magnetic flux density vector	[T]
B_f	Spectral brightness	[J/m²]
$B_{f,bb}$	Brightness, blackbody	[J/m²]
c	Speed of light in vacuum	[m/s]
$d_{0,ref}$	Reference snow grain size	[mm]
$d_{0,\mu}$	Reference snow grain size for land cover μ	[mm]
$\mathbf{D}$	Electric flux density vector	[C/m²]
D_i, D_j	Directivities of antennas i and j	-
D_{obs}	Observed snow grain size	[mm]
$\mathbf{E}$	Electric field vector	[V/m]

$E_{0,\mathrm{x}}$, $E_{0,\mathrm{y}}$	Electric field amplitude	[V/m]
f, f_0	Frequency, radiometer centre frequency	[Hz]
$f_i(\mathbf{x})$	Model giving using vector of variables **x**	-
$\mathbf{f}(\hat{\mathbf{0}}, \hat{\mathbf{i}})$	Normalized scattering amplitude vector	-
F_n	Normalized antenna beam pattern	-
F_{ni}; F_{nj}	Normalized beam patterns of antennas of radiometers i and j.	-
G_j	Gain of receiver j	-
G_s	Average system power gain	-
h	RMS height variation of rough surface	[m]
h	Planck's constant	[Js]
h_n	Thickness of layer n	[m]
$\mathbf{H}$	Magnetic field vector	[A/m]
$\mathbf{J}$	Total current density vector	[A/m^2]
J	Emission source function	-
k	Wave number	[m^{-1}]
k_B	Boltzmann's constant	[J/K]
l_n	Loss factor of layer n	-
M_{ij}	Quadrature-corrected correlation Coefficient for radiometers i and j.	-
N_v	Number of scatterers in volume V	-
q	Ratio of forward and total scattered radiation coefficients	-
P	Noise power	[W]
P_{in}	Receiver input power	[W]
P_r	Received power	[W]
P_s	Emitted power	[W]
$\tilde{r}_{ij}$	Fringe-washing factor of radiometer pair i, j.	-
r_n	Reflection coefficient of layer n	-

r_p	Modified reflection coefficient for polarization p	-
$r_{p,Fresnel}$	Fresnel reflection coefficient for polarization p	-
S_{av}	Power of electrical field	[J/sm^{-2}]
S_i	Power of incident field	[J/sm^{-2}]
S_{jy}	Gain of calibration network from source y	
	to receiver j	[dB]
S_n	Geometric sum of multiple reflections	
	in layer n	-
S_s	Power of scattered field	[J/sm^{-2}]
T	Temperature	[K]
T_A	Antenna temperature	[K]
T_B	Brightness temperature	[K]
$T_{B,n,\uparrow}$	Upwelling brightness temperature	
	of layer n	[K]
$T_{B,n,\downarrow}$	Downwelling brightness temperature	
	of layer n	[K]
T_c	Noise temperature of cold calibration load	[K]
T_{CAL}	Calibration source noise temperature	[K]
T_h	Noise temperature of hot calibration load	[K]
$T_{ij}^{'}$	Modified brightness temperature	[K]
t_n	Transmission coefficient of layer boundary n	-
T_N	Noise injection noise temperature	[K]
$T_{N,j}^{C1}, T_{N,j}^{C2}$	Noise levels measured at NIR outputs	
	for calibration signals 1 and 2	[K]
T_R	Receiver noise temperature	[K]
T_{REF}	Reference source noise temperature	[K]
T_s	Physical temperature of snow	[K]
T_{sys}	System noise temperature	[K]
u_{off}	Receiver offset	[V]

U_c	Receiver output voltage for cold calibration load	[V]
U_h	Receiver output voltage for hot calibration load	[V]
v_{j1}, v_{j2}	LICEF PMS output voltages of receiver j for noise injection levels 1 and 2 [V]	
V	Volume	[m^3]
V_{ij}	Visibility measured with radiometers i and j	[K]
V_{out}	Output voltage	[V]
W_μ, W	Snow water equivalent	[mm]
W_A	Beam energy loss due to absorption	[J/m]
W_{AS}	Beam energy loss due to scattering	[J/m]
W_f	Increase of beam radiation energy	[J/m]
W_E	Increase of radiation energy by thermal radiation	[J/m]
W_{IS}	Increase of radiation energy by scattering	[J/m]
x	Vector of variables x	-
x_j	Geophysical variables 1…m	-
$\hat{x}_{ref,j}$	A priori values of variables x_j -	
y	Vector of observations y	-
y_i	Remote sensing observations 1…n	-

List of appended papers

The research performed for this dissertation was carried out at the Laboratory of Space Technology, former Helsinki University of Technology (TKK), presently Aalto University, and at the Finnish Meteorological Institute (FMI) Arctic Research unit. The first part of the thesis concerns remote sensing of the cryosphere by means of passive microwave remote sensing, including forward modeling of snow-covered terrain and the application of inversion techniques to estimate snow properties from observations. This work was performed in part at Aalto University, and partly at FMI. The second part deals with the testing and analysis of an advanced calibration network for a space-borne interferometric radiometer; this work was conducted at Aalto University.

The work has been published in six peer-reviewed papers, which are included in full in the Appendix. This thesis summary gives a description of the conducted work and places it into context with other recent studies and advances in the field of remote sensing using microwave radiometry.

The roles of the participating authors of the appended papers are described in the following.

[P1] Lemmetyinen J., C. Derksen, J. Pulliainen, W. Strapp, P. Toose, A. Walker, S. Tauriainen, J. Pihlflyckt, J.-P. Kärnä, and M. Hallikainen, 2009. A comparison of airborne microwave brightness temperatures and snowpack properties across the boreal forests of Finland and Western Canada. IEEE Trans. Geosci. Remote Sens., 47(3), 965-978.

J. Lemmetyinen was responsible for data collection, instrument calibration and data analysis for the data collected in Finland, and for writing the manuscript. C. Derksen was responsible for detailed planning and execution of data collection, instrument calibration and data analysis for the data collected in Canada, and for assisting in the writing of the manuscript. J. Pulliainen initiated the original study plan and was responsible for developing the applied emission model. He also assisted in data collection, data analysis and writing of the manuscript. W. Strapp and P. Toose assisted in data collection and radiometer calibration in Canada. A. Walker was responsible for the overall campaigns conducted in Canada. S. Tauriainen, J. Pihlflyckt and J.-P. Kärnä assisted in data collection in Finland. M. Hallikainen was responsible for campaign operations in Finland.

[P2] Lemmetyinen, J., J. Pulliainen, A. Rees, A. Kontu, Yubao Qiu, C. Derksen, 2010. Multiple-layer adaptation of HUT snow emission model: comparison with experimental data. *IEEE Trans. Geosci. Remote Sens.,* 48(7), 2781-2794.

J. Lemmetyinen was responsible for development of the emission model, model simulations and collection and analysis of reference data from Finland. J. Pulliainen devised the original study plan and assisted in data collection, analysis, emission model development and writing of the manuscript. A. Rees, A. Kontu and Yubao Qiu assisted in data collection and data analysis. C. Derksen was responsible for data collection and analysis in Canada.

[P3] Gunn, G. E., C. R. Duguay, C. Derksen, J. Lemmetyinen, and P. Toose, 2011. Evaluation of the HUT modified snow emission model over lake ice using airborne passive microwave measurements. *Remote Sens. Environ.,* 115(1), 233-244.

G. E. Gunn was responsible for data analysis and writing of the manuscript. C. R. Duguay is credited with the original study plan, and assisted in data analysis and writing of the manuscript. C. Derksen assisted in data collection, data analysis and writing of the manuscript. J. Lemmetyinen assisted in writing of the manuscript and was responsible for emission model development for lake ice and model simulations. P. Toose assisted in data collection and instrument calibration.

[P4] Lemmetyinen, J., A. Kontu, J.-P. Kärnä, J. Vehviläinen, M. Takala, J. Pulliainen, 2011. Correcting for the influence of frozen lakes in satellite microwave radiometer observations through application of a microwave emission model. *Remote Sens. Environ..* 115(12), 3695-3706.

J. Lemmetyinen was responsible for the study plan, retrieval algorithm implementation, model simulations, analysis, and writing of the manuscript. A. Kontu, J.-P. Kärnä, J. Vehviläinen and M. Takala assisted in data collection and writing of the manuscript. J. Pulliainen assisted in retrieval algorithm implementation and writing of the manuscript.

[P5] Rautiainen, K., J. Lemmetyinen, J. Pulliainen, J. Vehviläinen, M. Drusch, A. Kontu, J. Kainulainen, J. Seppänen, 2012. L-Band radiometer observations of soil processes at boreal and sub-arctic environments. *IEEE Trans. Geosci. Remote Sens.,* 50(5), 1483-1497.

K. Rautiainen was responsible for data analysis and writing of the manuscript, and took part in data collection and instrument calibration. J. Lemmetyinen was responsible for emission model implementation, model simulations, planning of the experimental campaign, and assisted in data collection and writing of the manuscript. J. Pulliainen laid out the original outline for the study, assisted in data analysis, model implementation and writing of the manuscript. J. Vehviläinen assisted in data collection and writing of the manuscript. M. Drusch assisted in study planning and writing of the manuscript. A. Kontu was responsible for data collection and instrument calibration. J. Kainulainen and J. Seppänen were responsible for airborne data collection.

[P6] Lemmetyinen, J., J. Uusitalo, J. Kainulainen, K. Rautiainen, N. Fabritius, M. Levander, V. Kangas, H. Greus, J. Pihlflyckt, A. Kontu, S. Kemppainen, A. Colliander, M.T. Hallikainen, and J. Lahtinen, 2007. SMOS Calibration Subsystem. *IEEE Trans. Geosci. Remote Sens.,* 45(11), 3691-3700.

J. Lemmetyinen was responsible for planning and conducting the characterization tests on the CAS subsystem, analysis of results and writing of the manuscript. J. Uusitalo was responsible for CAS instrument design and development. J. Kainulainen performed the analysis of CAS error propagation and related SEPS simulations, and assisted with the writing of the manuscript. K. Rautiainen assisted in the planning and execution of CAS characterization measurements. N. Fabritius, M. Levander, V. Kangas and H. Greus assisted in instrument development and the characterization tests. A. Kontu and S. Kemppainen assisted in the planning and conduction of characterization tests and data analysis. A. Colliander assisted (a lot!) in writing of the manuscript. M.T. Hallikainen bore overall responsibility for the characterization tests. J. Lahtinen laid out the original study plan and assisted in the execution of the tests and writing of the manuscript. He was also responsible for the development of the CAS subsystem.

1. Introduction

Remote sensing is a term which can be applied broadly to describe any observation of an object from a distance by means of electromagnetic waves. The term is also applied to describe observation of the surface of the Earth from either space or an aircraft. Remote sensing can be conducted either by observing the emission of radiation from the object of interest (*passive remote sensing*), or by measuring the scattering properties of the object by exposing it to radiation and measuring the properties of the returned signal (*active remote sensing*). The focus of this thesis is on *passive microwave remote sensing*, i.e. the study of the microwave emission properties of natural objects, such as the surface of the Earth, and the instrumentation used to perform these measurements.

Microwave radiometry provides a powerful tool for purposes of Earth Observation (EO) from space. Due to the relatively low loss of microwave radiation in the atmosphere at certain frequency bands, microwaves can be used to obtain information of the Earth surface with only a small interference from atmospheric conditions (e.g. Tedesco and Wang 2006a). *Radiometers* are devices which measure the naturally emitted microwave radiation from an object, typically restricting observations to a defined frequency band, polarization and spatial area on the observed object. Since the emergence of the first satellite missions carrying microwave radiometers in the 1970's, these devices have been applied for a variety of purposes in Earth observation. In recent studies over sea surfaces, radiometers have been applied in e.g. detection of sea ice concentration (Comiso *et al.*, 1997; Spreen *et al.*, 2008; Mills and Heygster, 2010) and ocean salinity (e.g. Reul *et al.*, 2009; Font *et al.*, 2010). Over land surfaces, the relatively coarse spatial resolution of passive microwave instrumentation restricts applications to those presenting relatively homogeneous properties over a wide area; these include, for example, the observation of vegetation properties in the boreal forest zone (e.g. Grandell *et al.*, 1998), measurement of soil moisture (e.g. Njoku and Kong, 1977; Njoku *et al.*, 2003; Kerr *et al.*, 2010) and seasonal snow cover (e.g. Chang *et al.*, 1987; Goodison *et al.*, 1995; Kelly *et al.*, 2003). The monitoring of atmospheric properties from space is also possible by using microwave radiometry through the detection of wavelengths sensitive to atmospheric gases and particles, such as precipitation (e.g. Fox and Illingworth, 1997; Solheim *et al.*, 1998). Contrary to observations at optical wavelengths, microwave observations are possible regardless of lighting conditions, which is an important factor when monitoring polar regions. For many natural objects, microwaves also exhibit a larger penetration depth than optical frequencies, allowing to obtain information from beyond the surface of the object under scrutiny. Due to these features, microwave radiometry is an essential mean for monitoring of the Earth's cryosphere, such as the properties of sea ice, soil and seasonal snow cover.

1.1. Monitoring of the cryosphere using microwave radiometry

The cryosphere forms an integral part of the climate system of the Earth. It consists of diverse components including seasonal snow, mountain glaciers, ice sheets, seasonally frozen soils, sea ice and freshwater ice. Together, the cryosphere contains up to 75-80 % of the freshwater supply, the largest mass being contained in ice sheets (Fitzharris *et al.*, 1996, Lemke *et al.*, 2007). In the Northern Hemisphere, seasonal snow cover ranges from 3.8 km^2 in August to 46.5 million km^2 in January (Robinson *et al.*, 1993), covering 49% of the total land surface in midwinter. On the other hand, permafrost occurs over approximately 24 % of the land surface (Zhang *et al.*, 1999), with seasonal soil freezing affecting a total of 51 % (Zhang *et al.*, 2003). The cryosphere affects the climate system through its influence on surface energy balance, moisture flux and atmospheric circulation over both seas and land surfaces. In particular, a strong feedback is generated by the high reflectivity of snow cover, which controls the total surface albedo in the Northern Hemisphere during winter months, and the low thermal conductivity of snow which affects the heat transfer between soil and the atmosphere (Groisman *et al.*, 1994, Clark *et al.*, 1999, Zhang *et al.*, 2005). Monitoring of seasonal snow cover properties is therefore essential in understanding interactions and feedback mechanisms related to the cryosphere.

In addition to its extent, a key variable defining seasonal snow cover is the Snow Water Equivalent (SWE), which defines the total water content held in a snow pack as a product of snow depth and density. Together with glacier meltwater, the total water content of seasonal snow is the main driver considering spring runoff of rivers in Eurasia and North America (Barnett *et al.*, 2005). The total mass of the snow pack also determines its insulating properties, affecting soil processes such as freezing and thawing during the winter and the total energy transfer between the atmosphere and the surface of the Earth. Although snow cover properties such as snow depth and SWE can be monitored by the means of *in situ* monitoring networks (Ye *et al.*, 1998, Brown and Braaten, 1998, Dyer and Mote, 2006, Jonas *et al.*, 2009), observations with global coverage at a sufficient revisit time are only feasible by means of remote sensing from space. This holds especially for polar regions where monitoring networks are sparse and difficult to maintain.

The monitoring of Snow Water Equivalent and other properties of seasonal snow cover from space became possible with the launch the first operational multiple channel satellite microwave radiometers (e.g. Gloersen and Barath, 1977; Hollinger *et al.*, 1990). The basis of the detection of SWE lies in the inverse relationship of the observed intensity of microwave radiation and the total snow mass. This relationship is due to extinction of microwave radiation in the snow medium; radiation originating from the ground surface is both absorbed and scattered by snow, the total energy loss depending on snow properties and the amount of snow in the signal path. In dry snow, absorption effects dominate the extinction behavior in the lower end of the microwave spectrum, while scattering is dominant for higher frequencies, where scattering particles are comparable in size to the wavelength (Ulaby *et al.*, 1981). Increased scattering at higher frequencies can be exploited to detect the mass, or water content of snow (Rango *et al.*, 1979). For wet snow, however, the increasing liquid water content quickly causes the dominance of absorption effects over scattering throughout the microwave spectrum. This prevents the retrieval of snow mass properties from wet snow using passive microwave systems. On the other hand, the same effect enables the application of microwave radiometry for detection of, for example, snow melt onset and melt-refreeze areas (Künzi *et al.*, 1982; Cagnati *et al.*, 2004; Macelloni *et al.*, 2005), while the high contrast of emission signature from wet snow compared to snow-free terrain can be exploited to retrieve the instance of snow clearance (Takala *et al.*, 2009).

The first algorithms proposed for snow water equivalent retrieval typically relied on empirical formulae relating snow properties to the detected microwave emission (Rango *et al.* 1979; Foster *et al.*, 1980; Künzi *et al.*, 1982). As already indicated in these first studies, passive microwave snow cover estimates are prone to inaccuracies originating from spatial heterogeneity of the ground surface in the satellite's large field of view. These effects have been mitigated in past studies by applying e.g. compensation factors for the effect of vegetation (e.g. Foster *et al.*, 1991), or by deriving regional or land-cover specific regression coefficients to the inversion algorithms (e.g. Tait, 1998; Derksen *et al.*, 2010). Other sources of error arise from spatially and temporally varying snow conditions; regression coefficients defined for certain snow conditions may not be inter-annually consistent (Derksen *et al.*, 2003). This is due to the scattering in snow being dependant not only on the amount of snow, but also on e.g. the size and shape of the scattering (snow) particles. The density and vertical structure of the snowpack are other factors which vary spatially and evolve over time, deteriorating the capability of static inversion algorithms in detecting snow properties (Hall, 1987; Kelly *et al.*, 2003).

Consequently, an essential factor to understanding the observed microwave emission from space is the development of analytical models for describing the emission properties of snow covered terrain. Such models have to take into account e.g. the effects of land cover, soil, vegetation and atmosphere, as well as the snow cover itself. As an alternative to purely empirical algorithms, applying the inversion of these models to observations potentially allows the estimation of snow properties in diverse snow and land cover conditions; for example, Chang *et al.* (1987) proposed a discrete inversion algorithm based on radiative transfer calculations for certain snow conditions. Development and validation of forward models simulating microwave emission requires the use of extensive experimental datasets. Purely theoretical models have been formulated based on basic theory of microwave propagation (e.g. Tsang *et al.*, 2000; Strogyn, 1986). On the other hand, measurements conducted in controlled conditions have also provided information on the basic structural and dielectric properties of snow and its interaction with microwaves (e.g. Hallikainen *et al.*, 1987; Wiesmann *et al.*, 1998); this has allowed the development of semi-empirical models, i.e. models based on, for example, radiative transfer theory but adjusted with empirical fitting parameters (e.g. Wiesmann and Mätzler, 1999; Pulliainen *et al.*, 1999). Furthermore, passive microwave experimental datasets collected from natural landscapes from either ground-based or airborne instruments, accompanied by various *in situ* observations of the target properties, allow the verification of models in natural surroundings (e.g. Tedesco and Kim, 2006b).

1.2. Radiometer calibration

All remote sensing observations include an error element. The observation errors can typically be separated into random and systematic errors;

random errors arise e.g. from random thermal noise originating from the instrument components. Systematic errors, on the other hand, depend most on calibration accuracy of the instrument and subsequent drift after the calibration. Achieving good calibration accuracy, and on the other hand, instrument stability, are thus elemental factors when attempting to reduce the systematic errors of observations.

Calibration of space-borne microwave radiometer instrumentation is a challenging task; reliable operation of radiometers typically requires frequent calibration as the stability of the instrumentation may vary strongly with changing ambient conditions, such as physical temperature. Traditional calibration of radiometers relies on measuring two or more calibration targets or loads, the properties of which are accurately known. The calibration loads can be internal, allowing calibration of the radiometer receiver but excluding the antenna and some adjoining components, or external, in which case the whole instrument can be calibrated. The use of natural targets, such as the cosmic background can be used either for verification of calibration stability or as an external calibration load. Concerning artificial calibration loads, the main difficulty with space instrumentation is designing reliable and mechanically feasible solutions; external calibration loads typically consist of absorptive surfaces and mirror solutions to reflect the cold sky background to the radiometer. Internal calibration loads typically consist of passive loads at varying physical temperatures, or more recently, active microwave sources such as noise diodes.

1.3. Structure and study objectives

This thesis consists of two parts; in the first part, microwave radiometry is used in the study of snow cover and soil properties in the northern boreal forest and tundra regions. Airborne datasets of radiometer observations are applied to investigate the effect of varying land cover in the microwave signature of snow covered terrain [P1]. The studied effects include those of vegetation, and in particular, the signatures from lakes and other wetlands. Furthermore, an extension to an existing snow emission model (HUT snow emission model, Pulliainen *et al.*, 1999) is presented, allowing the simulation of multiple layered structures in snow [P2]. The model is further extended for the simulation of emission from snow-covered frozen lakes. Data from ground based and airborne observations are used to test the model performance in simulating the brightness temperature characteristics of stacked snow and ice structures [P3].

The emission model for lake ice is further applied used in a study presenting an advanced inversion algorithm for the estimation of Snow Water Equivalent. The developed algorithm allows to compensate for the effect of variable land cover in the estimate, such as the effect of snow covered lakes [P4]. Finally, the microwave signatures of soil in the boreal forest zone are investigated using a season-long experimental dataset of L-band radiometer observations and *in situ* information on soil. Again, an adaptation of the modified emission model is applied to examine the effect of soil freezing processes to the detected microwave signatures ([P5]).

The second part of the thesis deals with calibration of radiometer instrumentation. The design and characterization of a calibration subsystem for a space borne radiometer instrument at L-band is presented. L-band instruments are suitable for observing, for example, soil properties due to a relatively high penetration depth achieved. SMOS, the Soil Moisture and Ocean Salinity mission of the European Space Agency (ESA), was constructed for this purpose (Kerr *et al.*, 2010). The mission hosts an innovative payload, MIRAS (Microwave Imaging Radiometer using Aperture Synthesis; McMullan *et al.*, 2008), the first L-band interferometric radiometer deployed in orbit for Earth observation. Using a conventional radiometer, achieving imaging capability at the nominal resolution of SMOS (~50 km) would have required a prohibitively large antenna. Rather, MIRAS applies a set of small radiometer antennas and receivers that were placed in orbit in a contracted mechanical configuration, thus avoiding the difficulties associated with launching large, rigid mechanical structures in space. After launch, the antennas were extended to form a Y-shape, providing a synthetic aperture. The technique applied with MIRAS, aperture synthesis through interferometry, has been broadly applied in the field of radio astronomy, but MIRAS presented the first example of a space-borne interferometer used for remote sensing of the Earth. Calibration of the radiometer receivers in orbit is a challenging task at best; in the case of MIRAS, the large number of receivers provided a further complication as each receiver had to be provided with an individual but accurately known calibration signal. A design involving a distributed noise injection network was adopted for this purpose (Corbella *et al.*, 2000). The characterization of this Calibration Subsystem, CAS, was an important part of ground characterization of SMOS, as, among other things, the physical temperature of the network affects its properties. As a final part of this thesis work, a study on the characterization of CAS is presented in [P6].

Chapters 2 and 3 provide an overview of the theoretical basis of passive microwave remote sensing and radiometer instrumentation, respectively. A survey of research achievements retrieving snow properties from microwave signatures of snow covered terrain is given in Chapter 4. Chapter 5 details the multiple layer emission model developed during this work ([P2]). Chapter 6 summarizes measured emission signatures of varying snow covered terrain and describes modeling efforts done to simulate these signatures in various studies ([P1] – [P5]). Chapter 7 summarizes the application of the developed lake ice model in the context of SWE retrieval from satellite observations. The characterization of the SMOS calibration subsystem is described in chapter 8. Finally, the contribution of this thesis work to remote sensing of snow cover and on the other hand, radiometer calibration techniques, are summarized in Chapter 9.

2. Theory of microwave radiometry

This chapter gives an overview of the physical basis of microwave radiometry. In the first part, the theoretical basis of electromagnetic wave propagation in lossy media is presented, as well as a description of the basic definition for brightness temperature, the variable measured in microwave radiometry, and it's relation to the physical properties of natural objects. The second section introduces the basics of wave scattering in random media and scalar radiative transfer theory, which are later applied in the context of snow emission modeling. The last part of the section describes the typical measurement environment in microwave radiometry, and gives an overview of the different variables affecting the total observed microwave emission.

2.1. Electromagnetic fields and emissions from natural objects

Maxwell's equations (Maxwell, 1865) form the foundation of the classical theory of electromagnetism. The equations relate the electric and magnetic fields to each other and describe how electrical charges and currents act as sources to these fields. On the other hand, the emission of electromagnetic energy from natural objects can be explained by Planck's radiation law (Planck, 1901). Together, these form the theoretical basis for passive microwave remote sensing.

2.1.1. Maxwell equations for time-harmonic plane waves

For a time harmonic field, i.e. a field in which the time variation of the field phase follows a sinusoidal period, Maxwell's equations can be expressed as (Ulaby *et al.*, 1981)

$$\nabla \times \mathbf{E}(\mathbf{r}) = -j\omega\mathbf{B}(\mathbf{r})$$

$$\nabla \times \mathbf{H}(\mathbf{r}) = -j\omega\mathbf{D}(\mathbf{r}) + \mathbf{J}(\mathbf{r})$$

$$\nabla \cdot \mathbf{D}(\mathbf{r}) = \varrho(\mathbf{r}) \tag{2.1}$$

$$\nabla \cdot \mathbf{B}(\mathbf{r}) = 0,$$

where $\mathbf{E}(\mathbf{r})$ is the electric field, $\mathbf{H}(\mathbf{r})$ is the magnetic field, $\mathbf{B}(\mathbf{r})$ is the magnetic flux density, $\mathbf{D}(\mathbf{r})$ the electric flux density, $\mathbf{J}(\mathbf{r})$ is the total current density, and $\varrho(\mathbf{r})$ is the total charge density in the dimension $\mathbf{r}$. ω denotes the angular frequency ($\omega = 2\pi f$). For isotropic matter the flux densities can be expressed in terms of their equivalent fields so that $\mathbf{D} = \varepsilon\mathbf{E}$ and $\mathbf{B} = \mu\mathbf{H}$, where ε is the permittivity and μ the permeability .

Considering electric and magnetic fields in matter with no charges or currents, i.e. $\varrho(\mathbf{r}) = 0$ and $\mathbf{J}(\mathbf{r}) = 0$, the equations in (2.1) give the following wave equations for the fields (Helmholtz equations):

$$\nabla^2\mathbf{E}(\mathbf{r}) + \varpi^2\mu\varepsilon\mathbf{E}(\mathbf{r}) = 0$$

$$\nabla^2\mathbf{H}(\mathbf{r}) + \varpi^2\mu\varepsilon\mathbf{H}(\mathbf{r}) = 0. \tag{2.2}$$

The above equations describe the propagation of the electric and magnetic fields as a function of all three directions of the Cartesian coordinates ($\mathbf{r}$). In remote sensing, the distance to the observed source of radiation is in most cases large compared to the size of the source $\mathbf{r}$ (e.g. the footprint of a radar or radiometer instrument). Therefore, electromagnetic fields originating from the source can be approximated to be planar at the location of the observer, and vice versa (e.g. Tsang *et al.*, 1985). Plane waves can be expressed using a single Cartesian coordinate denoting the direction of propagation. For a plane wave propagating in the direction z this simplifies e.g. equation (2.2) for the electric field to the form[1]

---

[1] The electrical field now has two solutions: $\mathbf{E}(z) = \mathbf{E}_0 e^{\pm jkz}$; here $k = \omega\sqrt{\mu\epsilon}$ is the wave number, the positive exponential signifies the electrical field propagating in the forward direction and the negative a field propagating in the opposite direction.

$$\frac{d^2}{dz^2}\mathbf{E}(z) + \varpi^2\mu\varepsilon\mathbf{E}(z) = 0. \tag{2.3}$$

In general, all electromagnetic waves can be described as a sum of linearly polarized wave components. For plane waves, the polarization can be described by the sum of two orthogonal, linearly polarized components, both of which are also orthogonal to the direction of propagation so that

$$\mathbf{E}(z) = E_{0,\mathrm{x}}e^{j(\omega t-kz)}\mathbf{u}_{\mathrm{x}} + E_{0,\mathrm{y}}e^{j(\omega t-kz+\varphi)}\mathbf{u}_{\mathrm{y}}\ , \tag{2.4}$$

where $\mathbf{u}_{\mathrm{x}}$, $\mathbf{u}_{\mathrm{y}}$ are unit vectors perpendicular to $\mathbf{u}_{\mathrm{z}}$. Here, the time dependence is noted by $e^{j\omega t}$, and φ is the phase difference between the components.

Lastly, it follows from Maxwell's equations that the average total power density S_{av} of a time-harmonic electromagnetic field can be expressed by the real part of the so-called Poynting vector (Ulaby *et al.*, 1981). In a general direction **r**,

$$\begin{aligned} S_{av}(\mathbf{r}) &= \frac{1}{2}\mathrm{Re}\{\mathbf{E}(\mathbf{r}) \times \mathbf{H}^*(\mathbf{r})\} \\ &= \frac{1}{2}\mathrm{Re}\left\{\frac{k_r + jk_i}{\omega\mu}E_0^2\mathrm{e}^{-2\mathbf{k}\cdot\mathbf{r}}\right\} \\ &= \frac{1}{2}\frac{k_r}{\varpi\mu}E_0^2\mathrm{e}^{2\mathbf{k}\cdot\mathbf{r}}, \end{aligned} \tag{2.5}$$

where from (2.1), $\mathbf{H}(\mathbf{r}) = \frac{\nabla\times\mathbf{E}(\mathbf{r})}{-j\omega\mu}$.

2.1.2. Emission of microwave energy

All natural matter emits energy continuously in the form of electromagnetic radiation. The radiation arises from the thermal energy (heat) within the object. An idealized object, which both absorbs all incident radiation and also emits all of its thermal energy, is called a blackbody. Unlike a blackbody, natural objects emit only a part of their thermal energy; likewise, not all of the incident radiation is absorbed, but some is scattered. The radiated energy of a blackbody is given by Planck's radiation law

(Planck, 1901), which defines the spectral radiance (or, brightness) of an object so that for a blackbody at physical temperature T

$$B_f = \frac{2hf^3}{c^2}\left(\frac{1}{e^{\frac{hf}{k_B T}} - 1}\right), \tag{2.6}$$

where c is the speed of light in vacuum ($2.998 \cdot 10^8$ m/s), f is the frequency, h is Planck's constant ($6.634 \cdot 10^{-3}$ Js), k_B is Boltzmann's constant ($1.38 \cdot 10^{-23}$ J/K). In the microwave frequency range (approximately 300 MHz to 300 GHz) $hf \ll k_B T$. This leads to the Rayleigh-Jeans approximation [2] of Planck's law, which can be expressed as (Ulaby *et al.*, 1981)

$$B_f \approx \frac{2k_B T f^2}{c^2} = \frac{2k_B}{\lambda^2} T . \tag{2.7}$$

The Rayleigh – Jeans approximation holds well for most of the microwave spectrum (until approx. 120 GHz) when the physical temperature is close to Earth-ambient (~300 K). Figure 1 depicts the spectral brightness B_f as given by Planck's law against that given by (2.7) for three exemplary physical temperatures (1 K, 300 K and 1000 K). Planck's law determines the frequency spectrum of emitted radiation; the frequency with the maximal radiative power shifts to higher frequencies as the physical temperature increases. The maximal radiative power for objects at 300 K is close to 17 THz in the infrared region of the spectrum. For objects at 1 K temperature, the peak power is emitted already at 59 GHz; the validity of the Rayleigh-Jeans approximation at 1 K deteriorates quickly with increasing frequency at this temperature. For objects at 1000 K temperature, the peak spectral brightness occurs at 59 THz. At this temperature, the Rayleigh-Jeans approximation can be considered as valid for the whole microwave spectrum.

[2] The exponential term in (2.6) can be approximated by $e^{\frac{hf}{k_B T}} \approx 1 + \frac{hf}{k_B T}$.

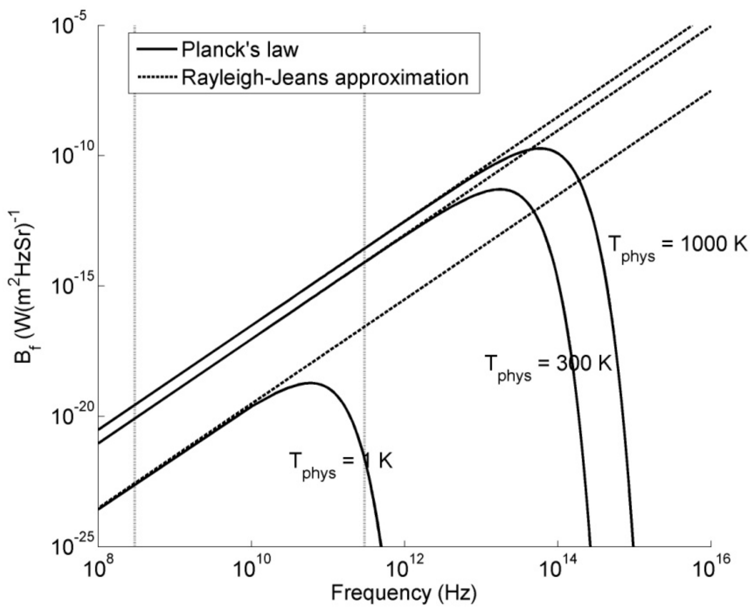

Figure 1. Comparison of Planck's law and the Rayleigh – Jeans approximation over the frequencies above 100 MHz for three values of blackbody physical temperature (1 K, 300 K and 1000 K). The nominal microwave frequency range of 300 MHz to 300 GHz indicated by vertical lines.

The emissivity ϵ of an object can now be defined as the ratio of the brightness B_f of the object to the brightness $B_{f,bb}$ of a blackbody at the same physical temperature (Ulaby *et al.*, 1981) so that

$$\epsilon = \frac{B_f(f,T)}{B_{f,bb}(f,T)}\,. \tag{2.8}$$

By applying the Rayleigh-Jeans approximation, we can define the brightness temperature T_B , i.e. the equivalent physical temperature of a perfect blackbody that would emit the detected amount of electromagnetic energy as a real object at physical temperature T. It follows, using (2.8), that the emissivity can be expressed simply by the relation of T_B and T:

$$\epsilon = \frac{T_B}{T}\,. \tag{2.9}$$

Equation (2.9) forms the basis for microwave measurements; the (apparent) brightness temperature T_B is the quantity measured by microwave radiometers, which can be directly related to the emissivity if the physical temperature is known. The emissivity, in turn, can be related, for example, to the dielectric properties of the observed object. The emissivity of natural objects typically varies with observation angle, polarization and frequency. Thus, inversion algorithms used to interpret brightness temperature observations may apply measurements at a number of frequencies or both horizontal and vertical polarizations, depending on the application.

2.2. Radiative transfer theory

Radiative transfer theory is an integral part of modeling the behavior of microwave frequencies in lossy (natural) media. Radiative transfer theory attempts to describe the propagation of electromagnetic intensity in a media characterized by absorption, emission and scattering properties. In this section, the basic theory behind scattering of electromagnetic radiation in random media is presented. The radiative transfer equation is described in terms of its different components. An adaptation for horizontally planar media, typically applied in the context of remote sensing, is presented.

2.2.1. Scattering and absorption in random media

For strongly scattering random media, various approximations have been developed to model the interaction of microwaves with the scattering particles. A defining factor in the choice of the scattering model is the size of the scattering particles when compared to the wavelength. Amongst the most common cases are (Ishimaru, 1978)

- Rayleigh scattering; when particles are small compared to the wavelength
- Physical optics approximation: when particles are large compared to the wavelength

- Application of Mie theory; scattering particles of various sizes are considered as spheres (the scattering of which can be modeled accurately)

In a general case, the scattering cross section of an object defines the relation of incident and scattered radiation from a particle or surface. At a distance R approaching infinity, the differential scattering cross section can be defined as (Ishimaru, 1978)

$$\sigma_d(\mathbf{r},\mathbf{r}') = \left|\mathbf{f}(\hat{\mathbf{0}},\hat{\mathbf{i}})\right|^2 = \lim_{R\to\infty} \frac{R^2 S_s(\mathbf{r})}{S_i(\mathbf{r}')}, \qquad (2.10)$$

where $\mathbf{f}(\hat{\mathbf{0}},\hat{\mathbf{i}})$ is the normalized scattering amplitude, S_i is the incident field power and S_s the power of the scattered field. The scattering cross section is obtained by integrating the normalized scattering amplitude $\mathbf{f}$ over 4π (Ishimaru, 1978):

$$\sigma_s = \int_{4\pi} \left|\mathbf{f}(\hat{\mathbf{0}},\hat{\mathbf{i}})\right|^2 d\Omega. \qquad (2.11)$$

The scattering coefficient can now be defined as (Ishimaru, 1978)

$$\kappa_s = \frac{N_v \sigma_s}{V}, \qquad (2.12)$$

where N_v is the number of scatteres in volume V, and σ_s is the scattering cross section of individual scatterers. The extinction coefficient the sum of the absorption and extinction coefficients, representing total loss of energy in the medium; $\kappa_e(s) = \kappa_s(s) + \kappa_a(s)$.[3]

[3] $\kappa_a = -2k|\mathrm{Im}\{\sqrt{\epsilon_r}\}|$; where ϵ_r is the complex permittivity of the media. e.g. Ulaby *et al.*, 1981.

2.2.2. General form of scalar radiative transfer equation

The radiative transfer equation in its scalar form can be written in terms of the energy balance of an infinitesimal unit of volume as depicted in Figure 2. The medium is characterized by the absorption coefficient κ_a and the scattering coefficient κ_s. A wave with brightness B_f propagates in direction **r** along the path s.

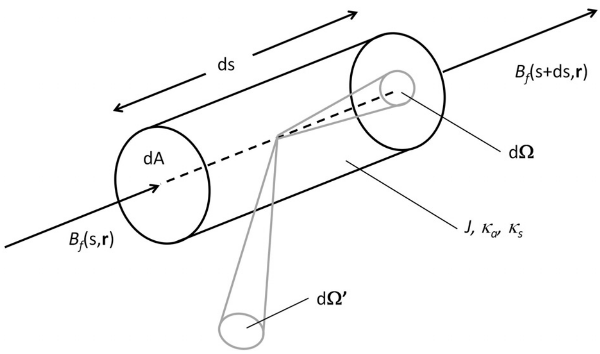

Figure 2.Factors of radiative transfer equation affecting brightness B_f along propagation path s at infinitesimal distance ds. The medium is characterized by the emission source function J, absorption $\boldsymbol{\kappa_a}$ and the scattering $\boldsymbol{\kappa_s}$. Incident scattering from all directions in angle dΩ' is scattered in direction r at solid angle dΩ as determined by the scattering phase function.

In this case, the increase of the beam radiation energy in the distance ds, denoted by W_f, can be expressed as (Sharkov, 2009)

$$\frac{dB_f(\mathrm{s}, \mathbf{r})}{ds} = W_f = W_E - W_A + W_{IS} - W_{AS}. \qquad (2.13)$$

The term W_E represents the increase of radiation energy caused by thermal radiation of the medium and attenuated by absorption. In a local thermal equilibrium, W_E is obtained from the intensity of radiation of a perfect blackbody (Sharkov, 2009)

$$W_E = \kappa_a(s)J(\mathrm{s}), \qquad (2.14)$$

where J the emission source function. The term W_A represents losses caused by absorption to the propagating radiation. This can be expressed by (Sharkov, 2009)

$$W_A = \kappa_a(s) B_f(s, \mathbf{r}). \tag{2.15}$$

The term W_{IS} represents the increase of energy, from radiation directed at the unit volume from all directions $\mathbf{r}'$ of a surrounding sphere, and scattered in the direction of propagation $\mathbf{r}$. This can be expressed as (Sharkov, 2009)

$$W_{IS} = \kappa_s(s) \frac{1}{4\pi} \int\limits_{4\pi} \Psi(\mathbf{r}, \mathbf{r}') \; B_f(s, \mathbf{r}') d\Omega\,, \tag{2.16}$$

where $\Psi(\mathbf{r}, \mathbf{r}')$ is the scattering phase function. The last term W_{AS} represents radiation losses due to scattering (Sharkov, 2009):

$$W_{AS} = \kappa_s(s) B_f(s, \mathbf{r}). \tag{2.17}$$

Using equations (2.14) to (2.17) enables one to write the radiative transfer equation in the form (Ishimaru, 1978)

$$\begin{aligned} \frac{dB_f(s, \mathbf{r})}{ds} \\ = -\kappa_e(s) B_f(s, \mathbf{r}) \\ + \kappa_s(s) \frac{1}{4\pi} \int\limits_{4\pi} \Psi(\mathbf{r}, \mathbf{r}') \; B_f(s, \mathbf{r}') d\Omega + \kappa_a(s) J(s). \end{aligned} \tag{2.18}$$

2.2.3. Radiative transfer equation for planar media

In its general form given by (2.18), solving of the radiative transfer equation can be challenging. For remote sensing applications, it is often useful to express (2.18) for a case of plane waves propagating in a media homogeneous in the azimuth direction, representing, for example, the atmosphere. For a plane wave propagating in the direction θ_i in respect to the z-axis in Cartesian coordinates, equation (2.18) can be simplified to

$$\frac{dB_f(z,\theta_i)}{dz} = -\kappa_e(z)\sec\theta_i\, B_f(z,\theta_i) + \kappa_s(z)\frac{\sec\theta_i}{2}\int_0^{\pi}\Psi(\theta')\; B_f(z,\theta')\sin\theta'\,d\theta' + \kappa_a(z)\sec\theta_i\, J(z). \tag{2.19}$$

2.3. Microwave radiometry in remote sensing

This section presents the factors affecting a practical observation in passive microwave remote sensing, and describes the connection between the electromagnetic field theory presented in previous sections and the measured quantity of brightness temperature.

2.3.1. Passive microwave observations

A schematic of the typical observation scenario in passive microwave remote sensing is depicted in Figure 3. The figure demonstrates the typical components contributing to the brightness temperature emitted in the direction of the observer in Earth orbit. These components include

a – the upwelling emission of the atmosphere

b – cosmic background (and/or solar) radiation reflected from the atmosphere

c- cosmic background (and/or solar) radiation reflected from the ground surface and attenuated in the atmosphere

d- downwelling emission of the atmosphere, reflected by the ground and attenuated in the atmosphere

e- upwelling emission from the ground surface, attenuated by the atmosphere

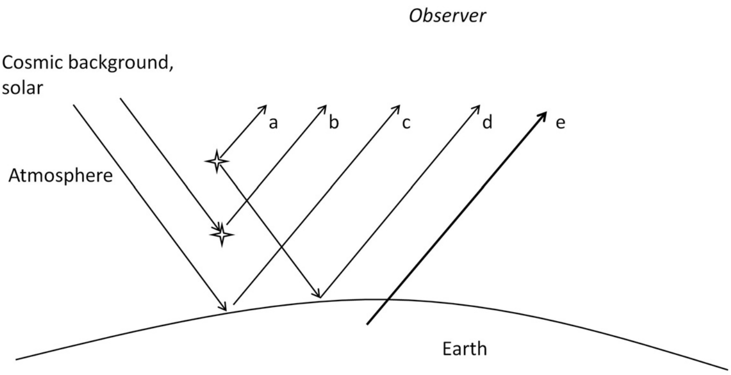

Figure 3. Schematic of passive microwave remote sensing scenario. The observed brightness temperature is a sum of components a-e.

A complication to passive microwave remote sensing is that the wanted parameter is typically only one of these factors, typically *e*. For a measurement occurring at a low altitude within the atmosphere (e.g. from a tower or from an aircraft), the components a and b may be neglected, as well as the atmospheric transmissivity affecting *e*. However, additional complications will arise when *e* consists of several components, only one of which is the wanted brightness temperature. For example, this study deals for the most part with observations of snow covered terrain; the emission from snow is the parameter sought after, whereas emission sources from the snow background and e.g. vegetation influence the observation in addition to the atmosphere and cosmic background components.

2.3.2. Antenna temperature

A schematic of the radiometer observation of brightness B_f is depicted in Figure 4. B_f in the direction θ_s of the receiver is given by (Ulaby *et al.*, 1981)

$$B_f = \frac{P_s}{\cos\theta_s \, A_s \Omega_s}, \qquad (2.20)$$

where P_s is the emitted power and A_s the infinitesimal area of the power source. On the other hand, the power P_r captured by the antenna aperture A_r at the solid angle Ω_r is (Ulaby *et al.*, 1981)

$$P_r = B_f A_r \Omega_r, \tag{2.21}$$

where A_r is the antenna aperture area and Ω_r the solid angle of observation covering A_r. Note that due to the invariant nature of radiance in the radiation path, B_f is independent of the distance *R* (Ulaby *et al.*, 1981).

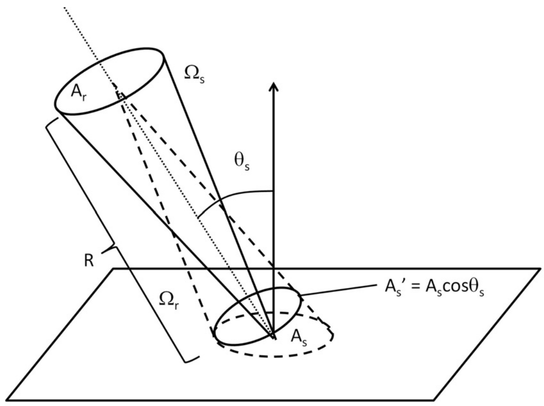

Figure 4. Schematic of measurement of radiance from surface *As* at distance *R*.

Now, considering an antenna with a normalized beam pattern[4] in an electric field with brightness $B_f(\theta, \phi)$, the total power detected by the antenna in the frequency range $\Delta f = f_2 - f_1$ can be expressed by (Ulaby *et al.*, 1981)

$$P = A_r \int_{f_1}^{f_2} \iint_{4\pi} B_f(\theta, \phi)\, F_n(\theta, \phi) d\Omega df. \tag{2.22}$$

---

[4] $F_n(\theta, \phi) = \frac{F(\theta,\phi)}{F_{max}(\theta,\phi)}$

Again considering the entire antenna beam pattern is surrounded by a blackbody at temperature T, using the Rayleigh-Jeans approximation for $B_f(\theta, \phi)$ the resulting power detected by the antenna is (Ulaby *et al.*, 1981)

$$P = k_B T \Delta f. \tag{2.23}$$

In this case, the power induced to the antenna by the blackbody is thus independent of the antenna gain or other parameters, and depends only the bandwidth and the physical temperature of the blackbody. For an observation of a non-blackbody target, the physical temperature is replaced by the *antenna temperature* so that $T = T_A$. T_A consists of the total brightness temperature in the scene observed by the radiometer, weighted by the antenna beam pattern $F(\theta, \phi)$. If the entire beam pattern is covered by a target emitting a brightness temperature T_B, then $T = T_A = T_B$ in (2.23).

2.3.3. Radiative transfer equation for passive microwave remote sensing

For the case of microwaves, the radiative transfer equations (2.18), (2.19) can be expressed in terms of the brightness temperature. This is useful in terms of most practical situations simulating the total brightness temperature emission of a media. In the microwave regime the emission source function J can now be substituted by either Planck's law or the Rayleigh-Jeans approximation ((2.6), (2.7)), so that in the spectral band Δf,

$$J = \frac{2k_B}{\lambda^2} T \Delta f. \tag{2.24}$$

Now, equation (2.19) for planar media can be expressed as

$$\frac{dT_B(z, \theta_i)}{dz} = -\kappa_e(z) \sec\theta_i \, T_B(z, \theta_i) + \kappa_s(z) \frac{\sec\theta_i}{2} \int_0^{\pi} \Psi(\theta') \; T_B(z, \theta') \sin\theta' \, d\theta' + \kappa_a(z) \sec\theta_i \, T(z). \tag{2.25}$$

From this, it is possible to solve the magnitude of the brightness temperature T_B at distance H in the media:

$$T_B(H) = T_B(0)e^{-\kappa_e H\sec\theta_i} + \sec\theta_i \int_0^H \left[\frac{\kappa_s(z')}{2}\int_0^\pi \Psi(\theta')\,T_B(\theta',z')\,\sin\theta'\,d\theta' + \kappa_a(z')T(z')\right] e^{-\kappa_e(z')\sec\theta_i}\,dz' \qquad (2.26)$$

3. Radiometers

Radiometers are used to measure the electromagnetic energy emitted by an object or area of interest. Radiometers designed for Earth observation are built to measure microwave radiation emitted by the Earth surface (or, atmosphere) from space or from aircraft, usually restricting observations to a defined frequency band, incident angle and optionally, polarization. Antennas with a high directivity are applied to enable spatial discrimination of the detected brightness temperatures. Radiometer receivers are designed to be very sensitive; contrary to, for example, radar signal receivers, the signal level received by the radiometer is typically smaller than the local noise level of the receiver. Care must be taken in the calibration of the radiometers, as this is typically the main factor defining radiometer accuracy. The stability of the radiometer in-between calibrations is also typically sensitive to changes in ambient conditions such as temperature and supply voltage to the receiver components. This sensitivity can be addressed to some degree with instrument design. This section describes some of the basic radiometer designs, as well as a description of the more complex imaging interferometric radiometer. A description of radiometer calibration methods is also given. Finally, a radiometer system applied for parts of this work is described.

3.1. Receiver architectures and sensitivity

The task of the radiometer receiver is to measure the antenna temperature T_{A}, which was presented in the previous section, and express the detected power as a quantifiable parameter (usually, voltage over the detector) at the receiver output. The output voltage is then integrated over a certain time period to reduce the effect of random variations in the signal, and calibrated with *a priori* calibration parameters to provide a measure of T_{A}. The general characteristics of the receiver can be summarized as being the receiver gain G, the receiver noise temperature T_R, and the receiver bandwidth B; the antenna temperature at the input of the receiver is amplified by the total gain G and restricted to the bandwidth B. T_R is a measure of thermal energy (noise) added by the receiver components to the signal at the antenna reference frame (i.e. T_A). The front end of a receiver may also include downconversion to a lower frequency (superheterodyne receivers). After amplification, band selection and possible downconversion, the signal is detected by the square-law detection and integrator stages.

The power available at the input of the receiver in the bandwidth B can be understood as a sum of receiver temperature and the receiver noise temperature, reduced to the receiver input; together these form the system noise temperature T_{sys}. Using (2.23), the input power is then (Ulaby *et al.*, 1981)

$$P_{in} = \mathrm{k_B}(T_A + T_R)B = \mathrm{k_B}T_{sys}B. \qquad (3.1)$$

Reduced to the system output, this results in the detected voltage

$$V_{out} = G\mathrm{k_B}BT_{sys}\,. \qquad (3.2)$$

The performance of a radiometer can be characterized in terms of its accuracy and precision (Ulaby *et al.*, 1981). The (absolute) accuracy of the receiver is mostly determined by the achievable calibration accuracy (see next section). The precision of the radiometer is determined by the receiver architecture, choice of components and measurement parameters. The precision ΔT, or sensitivity of the radiometer, is the smallest change in system noise temperature which can be determined by the receiver. The precision uncertainty consists of two components, that are statistically independent of one another: the uncertainty due to noise fluctuations ΔT_N and the uncertainty due to gain fluctuations of the receiver, ΔT_G. These can be summed so that (Ulaby *et al.*, 1981)

$$\begin{aligned}\Delta T &= \sqrt{[(\Delta T_N)^2 + (\Delta T_G)^2]} \\ &= T_{sys}\left[\frac{1}{B\tau} + \left(\frac{\Delta G}{G_s}\right)^2\right]^{1/2},\end{aligned} \qquad (3.3)$$

where τ is the integration time in seconds, ΔG is the effective RMS variation of the system power gain, and G_s the average system power gain. As seen from (3.3), the system noise temperature is an integral factor affecting the radiometer sensitivity. Minimization of the noise temperature is thus a major driver for radiometer design. The noise temperature is largely determined by the first amplification stage of the front end; therefore, the first amplifier is typically optimized for low noise rather than amplification, and all losses in components before the amplifier are minimized. A straightforward way to improve the sensitivity is also to increase of integration time τ; the method is applied widely in radio astronomy. For Earth observation purposes, this method is typically constrained by sampling frequency requirements, the chosen integration time being a tradeoff between spatial and temporal resolution and radiometric precision.

Equation (3.3) applies for the most basic radiometer design, termed the total power radiometer. In the following, a few other radiometer designs are briefly discussed. The motivation of the more advanced designs is typically the improvement of the radiometer precision, i.e. the minimization of ΔT_N and ΔT_G

Dicke radiometer

The so-called Dicke-switch radiometer (Dicke, 1946) introduces a switch as a first component after the antenna; the usually two-way switch adds a terminated load with noise temperature T_{REF} as a reference input to the antenna temperature (Skou and Le Vine, 2006). The measurement sequence is timed so that the observation time is divided between the antenna and the reference load in a single integration. The switch action frequency is typically fast, in the order of 1000 Hz, exceeding the typical gain variations ΔG in the receiver amplifiers; in this way, the system gain remains quasi-constant over the measurement cycle. The switching signal also drives a voltage inverter after the detector, which allows subtraction of antenna and the reference load duty cycles.

Dividing the observation time between the antenna and reference load effectively doubles the achievable noise uncertainty ΔT_N. However, under certain conditions the gain uncertainty ΔT_G can be completely eliminated. It can be shown that adding the reference load leads the radiometer sensitivity to be described as (Ulaby *et al.*, 1981)

$$\Delta T = \left[\frac{2(T_A + T_R)^2 + 2(T_{REF} + T_R)^2}{B\tau} + \left(\frac{\Delta G}{G_s}\right)^2 (T_A - T_{REF})^2\right]^{1/2}. \quad (3.4)$$

From (3.4), it is obvious that a minimum of ΔT (i.e. best sensitivity) is achieved when $T_{REF} = T_A$. T_{REF} should thus be chosen to match closely the expected measured brightness temperature. Several designs also exist to artificially match the reference load to the antenna temperature. These designs are discussed in the next section.

Balanced Dicke radiometer using noise injection

The concept of noise injection improves the Dicke receiver design presented in the previous subsection by artificially matching the reference duty cycle to the antenna temperature. Several methods exist to perform the balancing, including reference channel noise injection (Machin *et al.*, 1952), antenna channel noise injection (Goggins, 1967) and gain modulation (e.g. Orhaug and Waltman, 1962).

The reference channel noise injection method uses a feedback loop to control directly the reference load T_{REF} , e.g. by adjusting a variable attenuator which couples a noise source (diode) to the reference noise temperature channel, so that the radiometer remains balanced (i.e. $T_{REF} = T_A$). The antenna channel noise injection does the same but for the antenna channel. Figure 5 presents a schematic of the antenna noise injection method, which is of relevance concerning the presented work. In the design, the receiver output is set at V=0 through negative feedback driving a noise diode coupled to the antenna receiver input, giving the noise temperature T_I. Knowledge of the required T_I thus gives the antenna temperature, considering that T_{REF} remains stable. Compared to the reference channel noise injection, this method has the advantage that all conceivable antenna temperatures in Earth observations are fairly simple to match to the reference load, which can be kept at a relatively high ambient temperature. In the reference channel method, balancing low antenna temperatures with an equivalent reference would require either cryogenic cooling of the reference or, for example, the application of Active Cold Loads (e.g. Sobjaerg *et al.*, 2009).

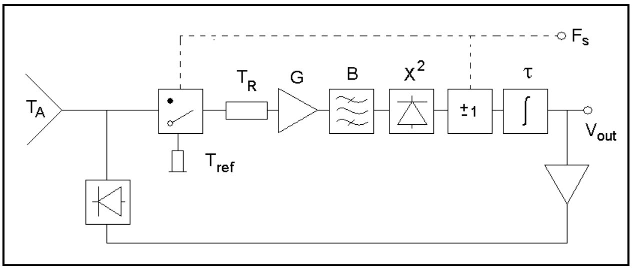

Figure 5. The noise injection radiometer (after Skou and Le Vine, 2006).

The sensitivity of the antenna channel noise injection radiometer can be expressed as (Ulaby *et al.*, 1981):

$$\Delta T = \frac{2(T \quad + T_R)}{\sqrt{B\tau}}, \tag{3.5}$$

where $T \quad = T_{REF}$ is in the ambient temperature of the reference load to which the antenna temperature is matched. For the concept to work in practice T has to be set higher than the largest measured antenna temperature.

3.2. The interferometric radiometer

Applying interferometry to Earth observing satellites is a fairly new concept although it has been applied in radio astronomy for decades. The motivation for interferometry is to achieve a synthetic aperture, matching a physical antenna aperture that would not be feasible mechanically or otherwise. In radio astronomy, applications typically employ narrow-beam antennas allowing high-resolution imaging of point-like targets. For purposes of remote sensing of the Earth, following a concept first proposed by Ruf *et al.* (1988), wide-beam antennas can be applied to achieve imaging capability over large surfaces without mechanically or electrically pointing the antenna beam.

Aperture synthesis is achieved by applying multiple antennae and receivers in a constellation; the multiple radiometers form each an interferometric pair with all the other receivers. These so-called baselines are correlated with one another. Both signals are divided before correlation; one divided signal is delayed using a phase shifter (analogue or digital) by 90 degrees, forming the so-called quadrature (Q) signal. The remaining two in-phase (I) signals are correlated to create the real part of the correlation coefficient; correlating the I and Q signals of different receivers forms the imaginary part. Also, the real part can be obtained by correlating the two quadrature signals, and the imaginary part from both of the two different combinations of in-phase and quadrature signals. Ideally, the two complex signals formed are each other's complex conjugates (Skou and Le Vine, 2006).

The correlated interferometric pairs form so-called visibilities, which can be expressed as (Corbella *et al.*, 2004)

$$V_{ij}(u,v) = \iint_{\xi^2+\eta^2\leq 1} T'_{ij}(\xi,\eta)\tilde{r}_{ij}\left(-\frac{u\xi+v\eta}{f_0}\right)e^{-j2\pi(u\xi+v\eta)}d\xi d\eta, \qquad (3.6)$$

where V_{ij} is the visibility measured by radiometers i and j; u and v denote the physical coordinates of the antennas of i and j in the interferometric system, and f_o is the central frequency. The direction cosines are given by $\xi = \sin\theta\cos\phi$ and $\eta = \sin\theta\sin\phi$. $\tilde{r}_{ij}$ is the fringe washing factor of the radiometer pair. The modified brightness temperature T'_{ij} is given by (Corbella *et al.*, 2004)[5]

$$T'_{ij}(\xi,\eta) = \frac{\sqrt{D_iD_j}}{4\pi}\frac{T_B(\xi,\eta)-T_r}{\sqrt{1-\xi^2-\eta^2}}F_{ni}(\xi,\eta)F^*_{nj}(\xi,\eta). \qquad (3.7)$$

where D_i and D_j are directivities and F_{ni} and F_{nj} the normalized field patterns of the antennas i and j, respectively, T_B is the apparent brightness

5 [1]Modification by Corbella *et al.* (2004) replaced brightness temperature T_B in the classical equation with the difference of brightness temperature and the physical temperature of the receiver (T_r). For an analysis of the effects of the modification, see e.g. Moreno-Galbis *et al.* (2007).

temperature and T_r is the physical temperature of the receivers (assumed here to be identical for i and j). T_B can be obtained from the visibilities using an image reconstruction technique based on inverse Fourier transform (Camps *et al.*, 1997).

In practice, the measured correlator counts are affected by the (usually non-identical) system noise temperatures of the receivers and the relative phase differences of the transmission path from antenna to receiver. In order to acquire V_{kj} as defined by the visibility equation, the measured correlator counts are first preprocessed to account for quadrature errors inherent to each receiver (the quadrature error is defined as the deviation from 90 degrees of the I and Q channels of the receiver), forming quadrature-corrected correlation coefficients M_{ij}. The visibility function can then be expressed in terms of the correlation coefficients, taking into account the system noise temperatures $T_{sys,i}$ and $T_{sys,j}$ of the receiver pair and the value of the fringe-washing function in the origin $\tilde{r}_{ij}(\tau = 0)$, so that (Corbella *et al.*, 2005)

$$V_{ij}(u,v) = \frac{\sqrt{T_{sys,i}T_{sys,j}}}{\tilde{r}_{ij}(0)} M_{ij} \tag{3.8}$$

where

$$M_{ij} = \frac{1}{\cos\theta_{qi}} \left(\mathrm{Re}\left[M_1 \mu_{ij}\right] + j\mathrm{Im}\left[M_2 \mu_{ij}\right]\right) \tag{3.9}$$

where $\mu_{ij} = \mu_{ij}^{ii} + j\mu_{ij}^{qi}$ is the normalized correlation coefficient, and M_1 and M_2 are parameters derived from the quadrature error θ_{qi} of the receiver i (Corbella *et al.*, 2005)[6].

[6] $M_1 = \cos\Theta'_{ij} - j\sin\Theta_{ij}$, $M_2 = \cos\Theta_{ij} + j\sin\Theta'_{ij}$, $\Theta'_{ij} = \frac{\theta_{qj}}{2} - \frac{\theta_{qi}}{2}$; $\Theta'_{ij} = \frac{\theta_{qj}}{2} + \frac{\theta_{qi}}{2}$

3.3. Radiometer calibration

Calibration of microwave radiometers is an essential part of their operation. Radiometer calibration is performed by measuring well-know calibration loads T_{CAL} with a noise temperature range equivalent to the expected range of antenna temperatures measured. The accuracy by which the calibration loads are known determines the accuracy of the radiometer, if these can be measured ideally (Ulaby *et al.*, 1981).

3.3.1. Two-point calibration

Calibration usually assumes a linear behavior of the receiver and square-law detection with changes in detected power. This is a good approximation in most cases, although non-linearities can be observed by accurate measurements (e.g. Hoer *et al.*, 1976). Additional calibration points can be applied to compensate for detector non-linearity (Skou and Le Vine, 2006). Assuming linear behavior, however, the relation of the measured output voltage at the detector can be related to the calibration noise temperature using the simple equation

$$V_{out} = G\left(T_{CAL} + u_{off}\right) \quad , \qquad (3.10)$$

where G is the gain or gradient of the calibration line and u_{off} the offset. Now, measuring two known calibration loads T_h and T_c enables one to solve the gain and offset using the corresponding output voltages U_h and U_c, so that (see Figure 6)

$$G = \frac{U_h - U_c}{T_h - T_c} \qquad (3.11)$$

$$u_{off} = \frac{U_c T_h - U_c T_c}{T_h - T_c}. \qquad (3.12)$$

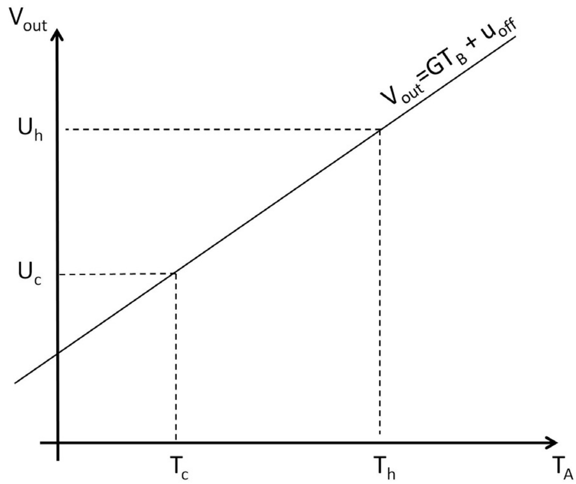

Figure 6. The calibration line formed by T_c and T_h (for "cold" and "hot" calibration loads).

In some cases, it may be preferable to calibrate also the small deviation from linearity of the detector (e.g. Hoer *et al.*, 1976). This may be especially be required if the range of measured brightness temperatures is large. The calibration can be performed by, for example, increasing the number of calibration points to four by injecting the noise temperature T_N from a stable noise source and coupling this with the hot and cold calibration loads, creating loads T_c , T_c+T_N, T_h and T_h+T_N.

3.3.2. Receiver and antenna calibration

Radiometer calibration can be made at 1) the antenna reference plane, or 2) at the receiver input reference plane (i.e. excluding the antenna). In the first case, the entire radiometer is calibrated. The calibration loads for the antenna reference plane typically consist of highly absorptive materials either at ambient temperature or materials cooled using a cryogenic substance (e.g. liquid nitrogen or helium). For space-borne instruments, the cryogenic load may also be replaced by observing the radiometrically cold cosmic background at ca. 2.7 K. This may be realized by using a reflecting microwave mirror (e.g. Imaoka *et al.*, 2010) or by periodically pointing the entire antenna at the cold sky. As a special case concerning ground-based radiometers, the so-called tip curve calibration method can be used (Han and Westwater, 2000). In the tip curve calibration method, the brightness temperature of the sky is observed from zenith to increasingly smaller elevation angles. This enables the establishment of a relationship between the brightness temperatures at different elevations angles and the optical thickness of the atmosphere; this, in turn, can be used to extrapolate the receiver output for a cold sky (without atmosphere). The method is suitable for wavelengths with relatively high transmissivity in the atmosphere; furthermore, the method assumes the atmosphere to be stratified and homogeneous in the horizontal direction, which restricts its use to clear-sky conditions.

When performing the calibration at the receiver input reference plane, the calibration loads are typically coupled to the receiver through a directional coupler or an additional input switch. The loads can consist of terminated waveguides at certain temperatures (at receiver ambient temperature or cryogenically cooled) or of active noise sources delivering a defined level of noise to the receiver. This simplifies the construction of calibration loads compared to antenna calibration. However, the antenna and connecting components must either be characterized *a priori* and assumed stable, or subtle changes in ambient conditions (i.e. temperature) of the antenna must be measured and taken into account through calculation. Furthermore, the measured calibration path is not entirely the same as is measured by the antenna. Therefore, in order to achieve optimal accuracy, impedance mismatches in the front end selection switch must be measured beforehand and taken into account in the calibrations. (Ulaby *et al.*, 1981).

3.4. The airborne radiometer system HUTRAD

A significant part of this work was made by applying measurements of the airborne HUTRAD (Helsinki University of Technology Radiometer) system; data collected using HUTRAD was used in [P1] and [P2]. The system consists of dual-polarized radiometer receivers at six frequencies (6.8, 10.7, 18.7, 23.8, 36.5, and 94 GHz). The 36.5 GHz system is fully polarimetric (Lahtinen *et al.*, 2003). The complement of frequencies closely corresponds to those available on past and present satellite microwave sensors (e.g. AMSR-E, the Advanced Microwave Scanning Radiometer for EOS). The radiometers are usually installed on a backward-profiling configuration, with a nominal incidence angle of ~50°. The characteristics of four receivers applied in this study are listed in Table 1.

TABLE 1: CHARACTERISTICS OF THE HUTRAD RADIOMETER SYSTEM.

	HUTRAD			
Frequency (GHz)	6.8	18.7	36.5	94
Bandwidth (MHz)	310	1000	400	2000
Receiver noise temperature (K)	400	640	1570	1100
Integration time (s)	defined by user; typical 0.5			
Sensitivity[1)] (K)	0.11	0.08	0.26	0.04
$\theta_{3\delta B}$ (°)	5	3	4	4

1) Theoretical value with 300 K antenna temperature

The calibration of the HUTRAD system is performed using a typical two-point calibration. Absorptive material at ambient temperature is used to cover the entire aperture of antennas to create a warm calibration target. The cold target is achieved using similar material cooled to ~77 K using liquid nitrogen. In addition, the 36.5 GHz system uses a polarimetric calibration standard (Lahtinen and Hallikainen, 2003). The system does not include a possibility for internal (receiver) calibration; therefore, emphasis has been put on the thermal stabilization of the receivers in order to minimize receiver gain and noise temperature variations in between calibrations.

4. Overview of SWE retrieval algorithms

A summary of investigations reported in the literature regarding the monitoring of snow water equivalent using passive microwave observations is provided. Although the subject has been studied for decades, there still remains ambiguity in particular related to the applicability of rigid, linear regression algorithms inter-annually and for varying land cover. Several early studies point out the necessity of accounting for snow metamorphosis and the natural variability of snow properties due to land cover and vegetation. One possibility for address this issue is through the application of physically-based emission models for snow cover.

The monitoring of snow depth and water equivalent can be performed on ground by means of manual or automated point-wise measurements by applying appropriate interpolation methodologies (e.g. Brasnett, 1999). However, in northern regions measurement networks can be sparse, and the representativeness of point-wise measurements of snow cover over large distances can be questioned (Atkinson and Kelly, 1997). Satellite microwave radiometry provides an appealing opportunity in this regard due to the spatial and temporal coverage of present satellite instruments and its applicability in polar regions.

Retrieval of Snow Water Equivalent from passive microwave observations dates back three decades to initial studies made using the first operational radiometers in space (Rango *et al.*, 1979; Foster *et al.*, 1980; Tiuri and Hallikainen, 1981; Künzi *et al.*, 1982). These studies define the basic methodology behind most present SWE retrieval algorithms from passive microwave observations. The hypothesis behind the algorithms is that the relatively high brightness temperature of the soil surface is scattered and thus attenuated by snow. The intensity of the scattering is depends on the wavelength, the amount of snow in the signal path and the scattering properties of snow; the latter are assumed to be affected especially by the size and shape of the scattering particles, i.e. ice crystals within the snow. Snow also provides a contribution to the detected signal through self-emission, but this contribution is considered to be small when compared to the (attenuated) ground emission.

The scattering intensity increases as the wavelength approaches the size of the scattering particles (e.g. Mätzler *et al.*, 1982). Considering that individual snow particles are measured in millimeters, high microwave frequencies (short wavelengths) will be attenuated more than low frequencies (long wavelengths). For this purpose, the first algorithms proposed for snow water equivalent and snow cover detection employ the scattering properties of a 37 GHz ($\lambda \approx 8.1$ mm) channel available on satellite instruments at the time. However, in order to account for the effect of varying brightness temperature of the soil background and snow, a lower frequency channel at ca. 19 GHz ($\lambda \approx 15.8$ mm) is applied as a reference. The scattering of a 19 GHz signal in snow is considerably smaller when compared to 37 GHz, while the emissivity of frozen soil and snow is largely similar at both frequencies. Thus observing the brightness temperature difference of the two channels, instead of only 37 GHz, allows one to establish a relation with the detected signal and snow depth with the additional benefit that the effect of variations in physical temperature on the measured brightness temperature are reduced. Similarly, observing a channel difference reduces or even cancels out systematic errors of the observation, provided that the errors in the two observations are similar (e.g. due to using common calibration targets). The first algorithms assume a linear regression dependence between the channel difference and snow depth (or, water equivalent). The algorithms take the general form

$$SWE = f(x) = \alpha + \beta \cdot x, \qquad (4.1)$$

where α and β are empirically derived parameters and $x = \Delta T_B = (T_{B,f1,p} - T_{B,f2,p})$ is the channel difference of frequency bands f_1 and f_2 at polarization p. Moreover, other frequency pairs than 19 and 37 GHz have been proposed (e.g. Derksen, 2008).

Already the first studies note that a general parameterization of (4.1) is unlikely to be applicable over the whole range of heterogeneous scenes observed by coarse-resolution passive microwave radiometers. In order to account for varying land and snow cover, several parameterizations and modifications to (4.1) have been proposed in the literature. In investigations by Hallikainen (1984), Hallikainen and Jolma (1986) and Hallikainen and Jolma (1992) the effect of varying local soil conditions and vegetation is compensated by applying a reference value for ΔT_B measured just before the first snowfall. Empirical parameterizations of the ΔT_B value are then calculated by using training data from small test areas. The study by Hallikainen (1984) also indicates substantial differences by land cover type to the sensitivity of ΔT_B with SWE; forested areas show considerably lower sensitivity when compared to bogs, farmland and freshwater surfaces (lakes and rivers). It is noted by Hallikainen and Jolma (1986), that although relatively good correlations between channel differences can be found in particular for the vertically polarized 19-37 GHz channel difference, the optimal parameterizations for the algorithm vary from year to year. Thus the study suggests applying yearly new parameterizations using training data.

Based on theoretical calculations of radiation extinction in the snow, Chang *et al.* (1987) proposed the first hemispherical parameterization of (4.1). The parameterization is validated over several regions using Nimbus-7 SMMR (Scanning Multichannel Microwave Radiometer) observations. The study notes that the algorithm is applicable to level snow cover with a mean grain radius of 0.3 mm, density of 0.3 g/cm^3 and a maximum depth of 1 meter. In agreement with results by Hallikainen and Jolma (1984), it was noted that the algorithm by Chang *et al.* (1987) tends to underestimate the SWE value for forested areas; this is due to the snow cover being virtually masked out by the emission from vegetation for densely forested areas, decreasing the channel difference ΔT_B and thus decreasing the sensitivity to changes in the underlying snow cover. Foster *et al.* (1991) use a correction of the form

$$SWE = \frac{\beta \cdot \Delta T_B}{1 - ff}, \tag{4.2}$$

where ff is the fractional forest cover; thus it is assumed that the sensitivity decreases in a linear fashion, approaching zero for grid cells with 100 % forest cover. However, this may be an oversimplification of the problem, as forest vegetation type (tree species) and the total vegetation biomass have a larger correlation with emission rather than a simple fractional forest cover figure (e.g. Hallikainen *et al.*, 1988).

Snow characteristics are rarely uniform over large areas. Therefore, static algorithm parameterizations following (4.1) are of limited accuracy when applied on a hemispherical scale. In order to overcome this, Foster *et al.* (1997) first proposed a modification to the original algorithm by applying regionally varying parameters in (4.1) for Eurasia and North America, following recorded snow densities and grain growth estimates. As an extension to this, empirical fits of (4.1) based on training data have been proposed on a regional basis (e.g. Hallikainen *et al.*, 1988). A further example of an empirical approach, applying *in situ* measured SWE values against satellite data in different regions, is the land cover sensitive algorithm suite developed by Environment Canada, consisting of different parameterizations for open prairie environments, deciduous forests, coniferous forests and sparse forests (Goodison and Walker, 1995; Derksen, *et al.*, 2002; Goita *et al.* 2003). When performing the retrieval, the algorithm weighs each algorithm by the fractional content of the respective land cover type in an observation grid cell, similarly to Hallikainen (1984).

An emerging approach is the use of snow emission models to account for dynamic changes in snow properties due to snow metamorphism and spatial variations due to land cover effects. Kelly *et al.* (2003) propose an algorithm which employs a non-linear brightness temperature difference between ΔT_B and snow mass, calculated using a radiative transfer model (Tsang *et al.*, 2000).The model is used in a deterministic way, i.e. values predicted by the model for different situations are predefined for different snow states using a polynomial fit. The algorithm also applies a temporally dynamic effective snow grain size and density, accounting for natural metamorphosis. However, the authors note an increase in RMS error when compared to reference data when the dynamic algorithm is used.

A study presented by Pulliainen and Hallikainen (2001) is of particular relevance to this thesis work. The study presents the use of a semi empirical snow emission model (Pulliainen *et al.*, 1999) in a numerical inversion algorithm of satellite observations. Separate modules account for atmospheric and vegetation effects. Several *a priori* parameters are required by the model (e.g. temperature, snow density, snow grain size, and soil properties) in order for the inversion to be successful. However, the study demonstrates that these parameters can be found to be regionally consistent; in order to allow for spatial variations in snow properties, the (effective) snow grain size is considered as a variable parameter constrained by a reference value and its statistical variability. Retrieval errors when compared to a linear regression algorithm are significantly decreased.

A further improvement extends the applicability of the method of Pulliainen and Hallikainen (2001) to a hemispherical scale. A main driver in the applied emission model and thus retrieval accuracy is the (effective) value for snow grain size; this determines largely the sensitivity of scattering to snow volume. In an improved algorithm (Pulliainen, 2006), the snow grain size is used to fit the model to observations in locations where snow information is available (e.g. from a weather station network). The obtained values for effective grain size are then extended over the whole area of observations using kriging interpolation (see e.g. Isaaks and Srivastava, 1989). The obtained map of effective grain size and grain size uncertainty is then applied in the numerical inversion of the emission model following Pulliainen and Hallikainen (2001). As a last step, the satellite-retrieved SWE estimates and weather station observations are combined in a Bayesian assimilation scheme. In a recent study (Takala *et al.*, 2011), the assimilation method is shown to considerably improve SWE estimates on a hemispherical scale when compared to typical algorithms based on linear regression. Table 2 summarizes the most notable characteristics of the discussed SWE retrieval algorithms as reported in literature.

TABLE 2: SUMMARY OF SNOW WATER EQUIVALENT RETRIEVAL ALGORITHMS FROM PASSIVE MICROWAVE OBSERVATIONS

Study	Applicable sensor	Algorithm type	Specifics
Künzi *et al.* (1982)	SMMR	Linear regression of horizontally polarized brightness temperature gradient*	Empirical algorithms based on limited training data
Hallikainen (1984) Hallikainen and Jolma (1986)	SMMR	Linear regression of horizontally polarized brightness temperature difference	Use of snow free reference brightness temperature
Chang *et al.* (1987)	SMMR	Linear regression of horizontally polarized brightness temperature difference	Parameterization based on theoretical calculations of extinction in dry snow
Foster *et al.* (1991)	SMMR	Linear regression of horizontally polarized brightness temperature difference	Fractional forest cover correction
Goodison and Walker (1995)	SSM/I	Linear regression; vertically polarized brightness temperature difference	Region-specific parameterization for North American prairies
Foster *et al.*, (1997)	SMMR	Linear regression; horizontally polarized brightness temperature difference	Fractional forest cover correction Region-dependant parameterization for North America and Eurasia
Goïta *et al.* (1997)	SSM/I	Linear regression; vertically polarized brightness temperature difference	Fractional forest type consideration
Pulliainen and Hallikainen (2001)	SSM/I	Radiative transfer model inversion of spectral and polarization difference	Dynamic effective grain size restricted by statistical variance Vegetation/atmosphere effect compensation.
Kelly *et al.* (2003)	SSM/I (AMSR-E)	Non-linear regression algorithm based on radiative transfer model parameterization	Temporally varying empirical grain growth and density expressions
Takala *et al.* (2011)	SMMR SSM/I AMSR-E	Radiative transfer model inversion of spectral difference. Combined with assimilation of *in situ* derived snow depth	Radiative transfer model parameterization using *in situ* data. Assimilation of passive MW SWE estimates with kriging-interpolated snow depth maps

*gradient $GT = \frac{T_{B,f1} - T_{B,f2}}{f_1 - f_2} \left[\frac{K}{GHz}\right]$

5. Multiple layer modification of HUT snow emission model

A multiple-layer adaptation of the HUT snow emission model (Pulliainen *et al.*, 1999) was developed in the frame of this thesis work. The original model considers the snowpack as a single homogeneous layer of snow with effective scattering and absorption properties. In most cases, this is a simplification of the complex stratigraphy of snowpacks (e.g. Colbeck, 1991). However, the motivation of the original formulation was to provide a simple enough model which would allow inversion of satellite observations, based on the type of limited knowledge of snowpack structure available for a large scale retrieval (Pulliainen and Hallikainen 2001). Also, it is arguable that the effect of snow stratification on retrieval accuracy is minimized in the typical comparative algorithms relying on brightness temperature difference of two channels on the same polarization (Foster *et al.*, 2005). The effect is further reduced with coarse scale observations covering large areas, and when the vertical polarization is employed (e.g. Hallikainen, 1984). Indeed, satisfactory retrieval results on a hemispherical scale have been achieved recently using a method based on inversion of the original one-layer model (Takala *et al.*, 2011). In the method, the emission model is first used to assign effective values for the size of scattering particles in the snow, where reference information on snow depth is available. These effective values, essentially compensating also for effects of snow layering, are then applied over a larger area using interpolation.

However, it is clear that natural snowpacks form layered structures that affect the microwave emission (e.g. Boyarskii and Tikhonov, 2000). As such, layered emission models on a point scale can yield superior results when compared to one-layer models (e.g. Hall, 1987, Durand *et al.* 2008, Rees *et al.*, 2010). The question concerning practical retrieval applications on a satellite scale remains on how to acquire the necessary information on stratification to drive the forward models. Physical snow models of varying complexity (e.g. Sun *et al.*, 1999, Brun *et al.*, 1989) can be used to predict snow stratification to a good degree of accuracy if adequate input information is available. Coupling these models with layered forward emission models has been shown to yield reasonable results (Andreadis *et al.*, 2008, Durand *et al.*, 2008) on point scales. Furthermore, clear, layered structures in winter landscapes are formed by sea, lake and river ice covered with snow. Moreover, lake ice growth can be predicted using either weather station or atmospheric reanalysis information to drive a physical lake ice model (Duguay *et al.*, 2003). Therefore, the HUT model was modified to accommodate simulation of emission from several stratified layers of ice or snow (Lemmetyinen *et al.*, 2010, [P2]). This section presents the physical basis of the HUT model and the modification made to accommodate multiple layers in the simulation. A section describing model inversion methods is also included.

5.1. Original HUT snow emission model

The original HUT snow emission model (Pulliainen *et al.*, 1999) is a radiative transfer-based, semi-empirical model which calculates the emission from a single homogenous snowpack. The HUT model assumes that most scattering of radiation propagating in a snowpack is concentrated in the forward direction (of propagation). This assumption is based on studies by Hallikainen *et al.* (1987); similar results for the scattering phase matrix have also been obtained using the DMRT (Dense Media Radiative Transfer) model (Tsang *et al.*, 2007)[7]. Based on the consideration of dominant forward scattering, the HUT model applies the delta-Eddington approximation (Joseph *et al.*, 1976) to the radiative transfer equation, applying an empirical constant to determine the forward scattered intensity of snow.

The absorption coefficient in the HUT model is determined from the complex dielectric constant of dry snow, applying the Polder-van Santen mixing model for the imaginary part (Hallikainen *et al.*, 1986). The calculation of the real part of the dielectric constant for dry snow is presented by Mätzler (1987). Emission from the snow layer is considered as both up-and downwelling emission. These are, in turn, reflected from interfaces between layers (air-snow, snow-ground). The transmission and multiple reflections between layers interfaces are calculated using the incoherent power transfer approach presented by Ulaby *et al.* (1981).

[7] DMRT is a theoretical model based on vector radiative transfer theory, modified for dense media, taking into account the full polarized nature of electromagnetic radiation (contrary to scalar radiative transfer, which models only the propagation of intensity). The model thus allows the calculation of effects such as correlative scattering between particles.

The extinction coefficient of snow, dependant on snow grain size and frequency, is calculated empirically following Hallikainen *et al.* (1987). Snow wetness and salinity content can be simulated if required; the modified dielectric constants for wet or saline snow are described through empirical formulae. Reflection and transmission coefficients and the refraction angle between layer interfaces are calculated using an incoherent approach (Ulaby *et al.*, 1981) following Fresnel's law.

For radiation propagating in a snowpack at depth *d'* at the angle θ, the HUT snow emission model expresses the transfer equation in eq. (2.25) so that (Pulliainen *et al.*, 1999)

$$\frac{\partial T_B(d',\theta)}{\partial d'} = \kappa_a \sec\theta\, T_s$$

$$+\kappa_s \sec\theta \frac{1}{4\pi} \iint_{4\pi} \Psi(\mathbf{r},\theta',\phi')\, T_B(d',\theta',\phi') \sin\theta'\, d\theta' d\phi' \tag{5.1}$$

$$-\kappa_e \sec\theta\, T_B(d',\theta),$$

where T_B is the brightness temperature, T_s the physical temperature (of snow), κ_a the absorption coefficient, κ_e the extinction coefficient, κ_s the scattering coefficient, Ψ the scattering phase function and **r** the unit vector to the angle of observation.

The most challenging problem in solving the radiative transfer equation in (5.1) can be said to be determination of the scattering phase function, which determines the increase or decrease in radiated intensity due to multiple scattering. The HUT model assumes that most of the scattered radiation in a snowpack is concentrated in the forward direction (of propagation) due to multiple scattering within the snow media. This assumption is based on previous studies by Hallikainen *et al.* (1987). The HUT model applies the delta-Eddington approximation to the radiative transfer equation; in the case of dominant forward scattering the scattering phase function can be expressed in terms of the differential scattering cross section σ_d and the particle scattering cross section $\sigma_s(\hat{\mathbf{r}})$ so that (following Ishimaru, 1978)

$$\Psi(\hat{\mathbf{r}},\hat{\mathbf{r}}') = \frac{4\pi\sigma_d(\hat{\mathbf{r}},\hat{\mathbf{r}}')}{\sigma_s(\hat{\mathbf{r}})}\, \delta(\theta-\theta')\delta(\phi-\phi'). \tag{5.2}$$

Now, assuming that the ratio between forward scattered and total scattered radiation coefficients is expressed by a constant q so that

$$q = \frac{\sigma_d(\hat{\mathbf{r}}, \hat{\mathbf{r}}')}{\sigma_s(\hat{\mathbf{r}})}. \tag{5.3}$$

Equation (5.1) can be now simplified to

$$\frac{\partial T_B(d', \theta)}{\partial d'} = \kappa_a \sec\theta \, T_s + \sec\theta \, (q\kappa_s - \kappa_e) T_B(d', \theta). \tag{5.4}$$

The emission of the snow medium with thickness d_0 just below the medium boundary can be then obtained from (Pulliainen *et al.*, 1999):

$$T_B = T_s \frac{\kappa_a}{\kappa_e - q\kappa_s} \Big(1 - \exp\big((-\kappa_e + q\kappa_s) \cdot d_0 \cdot \sec\theta\big)\Big), \tag{5.5}$$

where $1/L$ is the attenuation. An empirical equation is used to relate the snow extinction coefficient to frequency and snow grain size (Hallikainen *et al.*, 1987), so that for frequencies 1 to 60 GHz;

$$\kappa_e = 0.0018 f^{2.8} D_{obs}^2 \,, \tag{5.6}$$

where f is the frequency in GHz and D_{obs} is the observed scattering particle (snow grain) diameter in millimeters. The empirical parameter q in (5.5) has been defined for snow by fitting the HUT model to experimental snow slab emission data (Pulliainen *et al.*, 1999). The emission data, presented by Weise (1996), represents several snow types and spans a frequency range from 11 to 94 GHz. A common value of q=0.96 was found to be applicable for all frequencies in this range.

It should be noted that the parameter q includes effects from multiple scattering in the snowpack, and is as such relatively high compared to a case of singular scattering following e.g. the Rayleigh scattering approximation. As pointed out by Hallikainen *et al.* (1987), in snow the losses due to scattering are approximately equal to generation of incoherent intensity by scattering. This is supported also by recent theoretical studies of multiple scattering in snow, which predict that at microwave frequencies, the largest part of total volume scattering to be in the forward direction (Tsang *et al.*, 2007).

5.2. Multiple layer adaptation

The original HUT snow emission model (Pulliainen *et al.*, 1999) was expanded to allow the simulation of emission from a vertically stacked structure of multiple snow and ice layers. The original formulation of radiation scattering and absorption in individual snow layers was not altered (Lemmetyinen *et al.*, 2010, [P2]).

5.2.1. Emission from a system of stacked layers

The treatment of multiple layers is based on calculating the transfer of incoherent radiation intensity between layers (Ishimaru, 1978); coherent effects are neglected[8]. Snow and ice layers are considered as stacked, smooth planar layers, infinite in the horizontal direction (Figure 7).

---

[8] The omission of wave coherence effects between layer reflections originates in part from the original purpose of the HUT model as a simple, computationally light model for large scale inversion and retrieval of snow properties (see e.g. Pulliainen and Hallikainen, 2001). Although the omission of coherence effects may degrade the performance of the model on the point scale in cases where a discrete thin layer is present (e.g. Rees *et al.*, 2010), it is unclear whether the variable nature of natural snowpacks allows coherence effects to persist on the scale of satellite applications.

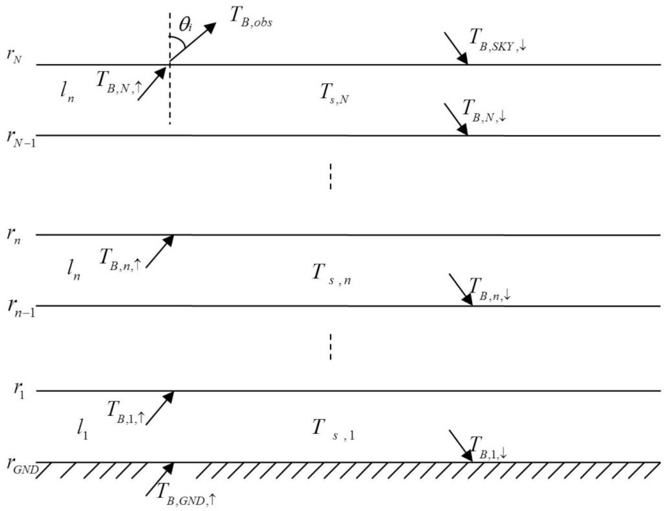

Figure 7. Schematic overview of the new multiple layer HUT snow emission model, with N layers of snow or ice, each with brightness temperature $T_{s,n}$, reflection r_n and attenuation l_n. Air and ground layers (layers N+1 and "0", respectively) contribute their respective up- and downwelling brightness temperatures $T_{B,SKY}$ and $T_{B,GND}$. *Lemmetyinen et al. (2010) [P2].* © 2010 IEEE.

The resulting emission is calculated based on the emissivity and attenuation properties of individual layers, and the reflection and transmission coefficients at layer interfaces. The upwelling emission flux $T_{n,\uparrow}$ of layer n of a system as depicted in Figure 7 can be determined as

$$T_{n,\uparrow} = S_n \left(T_{s,n} + T_{n+1,\downarrow} \frac{t_n r_{n-1}}{l_n^2} + T_{n-1\uparrow} \frac{t_{n-1}}{l_n} + T_{s,n} \frac{r_{n-1}}{l_n} \right), \qquad (5.7)$$

where t_n r_n and l_n are the Fresnel transmission and reflection coefficients, and the loss factor of layer n, respectively. S_n is the geometric sum of multiple reflections in layer n, so that

$$S_n = \frac{1}{1 - r_n r_{n-1}/l_n^2}. \qquad (5.8)$$

In (5.7), the first term inside the parenthesis is the internal upwelling emission, the second term the downwelling emission from layer n+1, reflected from layer n-1, and attenuated twice by l_n. The third term is the upwelling emission from layer n-1, reduced to interface n, and the last term is the internal downwelling emission, reflected from r_{n-1} and reduced to r_n. Similarly, the downwelling emission is expressed as

$$T_{n,\downarrow} = S_n \left(T_{s,n} + T_{n+1,\downarrow} \frac{t_n}{l_n} + T_{n-1\uparrow} \frac{t_{n-1} r_n}{l_n^2} + T_{s,n} \frac{r_n}{l_n} \right). \qquad (5.9)$$

The up- and downwelling fluxes of each layer can then be expressed as a group of linear equations, from which the total upwelling emission $T_{n,\uparrow}$ beneath the topmost layer can be solved. The mathematical solution is presented in [P2]. The multiple layer adaptation can also be directly employed in the simulation of a water-ice-snow system, such as snow covered lake ice.

5.2.2. Simulation of ice layers

For a layer consisting of pure ice, the HUT model considers scattering to be negligible. Therefore, it is assumed that the proportion of scattering is completely directed in the forward direction (q=1). In other words, the extinction in an ice layer is considered to be dependent only on the absorption, simplifying (5.1) to

$$T_B = T_s \left(1 - \exp\big((-\kappa_a) \cdot d_0 \cdot \sec\theta\big) \right). \qquad (5.10)$$

Stacked layers, which can be considered to be pure ice and therefore applicable to (5.10), are present in nature mainly in the case of frozen lakes and sea ice. Even with these, bubble formation by upwelling gases and, on the other hand, impurities and trapped particles may induce scattering effects. Another possible application may be a rain-induced ice lens (Rees *et al.*, 2010). For simulation of reflections from the soil-snow interface, the empirical model by Wegmüller and Mätzler (1999) has typically been applied (e.g. Pulliainen *et al.*, 1999, Pulliainen, 2006, Takala *et al.*, 2011). However, in the case of snow-covered lake ice, the model is not applicable to the simulation of reflections from the interface between water and ice. While this interface can be considered with good precision to be a specular surface, even small roughness variations are likely to cause notable deviations from specular reflection due to the high contrast in dielectricity between water and ice. Therefore, a relation between the small scale RMS variation of surface height h and the reflection coefficient of the ice/water interface was adopted following Choudhury *et al.* (1979)

$$|r_p|^2 = |r_{p,Fresnel}|^2 \exp(-4k^2h^2 \cos^2\theta)\,, \tag{5.11}$$

where $r_{p,Fresnel}$ is the Fresnel (specular) reflection coefficient for polarization p, k is the wave number, h the height variation (rms) of the rough surface and θ the incidence angle. This approach can be considered to be applicable when surface roughness variations are small compared to the wavelength. However, it may be difficult to assign a relation between measurable physical properties of the surface (correlation length, rms height variation) and h (Ulaby *et al.*, 1982). Therefore, h should be considered as an empirical fitting parameter.

5.3. Model inversion

Remote sensing observations can be interpreted as geophysical parameters by inverting physical forward models, e.g. models simulating microwave emission. The inversion of complex, non-linear models driven by multiple channels of observational data often leads to numerical solutions. In the following, the use of these methods is briefly discussed.

In general, the outcome of a satellite observation can be expressed with a model f so that

$$\mathbf{y} = f(\mathbf{x}) + \boldsymbol{\varepsilon}\,, \tag{5.12}$$

where $\mathbf{y} = [y_1, \ldots, y_\mathrm{n}]^T$ is a vector field of remote sensing observations on channels n, $\mathbf{x} = [x_1, \ldots, x_\mathrm{n}]^T$ is a vector of the value of a geophysical variable driving the model f, and $\boldsymbol{\varepsilon} = [\varepsilon_1, \ldots, \varepsilon_\mathrm{n}]^T$ is a vector describing the summed modeling and observation errors. The errors include both 1) systematic errors, e.g. due to errors in instrument calibration and physical basis of the model, and 2) random errors, e.g. due to random noise of observations. However, when applied as a basis of an inversion algorithm, the systematic errors are considered to be zero. The inversion (i.e. retrieving x from the observations y) can be based on empirically derived, linear or non-linear regression relations between the observation and x. The inversion of linear regression is relatively simple once the regression relations have been established by sufficient training data.

For more complex models f, a numerical solution may be required. If the modeling error is assumed to be unbiased and normally distributed, statistical inversion theory can be applied (Pulliainen, 2006). Following Bayes' theorem, the parameters x, y and ε are all considered to be random variables characterized by their probability distributions. The inverse solution of the probability distribution function is given by minimizing the so-called cost function

$$J(\mathbf{x}) = \sum_{i=1}^{n} \frac{1}{2\sigma_i^2} \left(y_i - f_i(\mathbf{x})\right)^2 , \qquad (5.13)$$

where σ_i denotes the standard deviation of the random errors ε. The modeling errors include all uncertainties related to the expected behavior of the brightness temperature with x, including the effect of variables inaccurately accounted for and physical inaccuracies inherent to the model itself.

Considering the practical use of (5.13), σ_i should be understood to include also observation errors related to the instrument. These, in turn, are dependant mostly on the calibration accuracy and subsequent calibration drift of the instrument. In order to reduce the systematic errors of the observation, the observations y_i can also consist of a channel or polarization difference; assuming that the systematic errors are similar for both channels, analyzing the difference instead of individual channels largely cancels out the errors. In a practical remote sensing application, however, the model errors in σ_i may typically outweight systematic errors caused by instrument calibration.

Furthermore, if *a priori* information of one or more of the geophysical parameters x_j is available, (5.13) can be expanded using the constrained minimization approach, so that

$$J(\mathbf{x}) = \sum_{i=1}^{n} \frac{1}{2\sigma_i^2} \left(y_i - f_i(\mathbf{x})\right)^2 + \sum_{j=1}^{m} \frac{1}{2\sigma_{ref,j}^2} \left(\hat{x}_{ref,j} - x_j\right)^2 , \tag{5.14}$$

where $\hat{x}_{ref,j}$ denotes the *a priori* values of parameters x_j and $\sigma_{ref,j}$ their standard deviation. This constrains the solution of the minimization towards $\hat{x}_{ref,j}$, the relative weigh of each reference value depending on their standard deviations.

6. Simulation of microwave signatures of snow-covered terrain

The main motivation for work presented in this chapter was the known variability of microwave emission signatures in the winter landscape of boreal forests. In this regard, the boreal forest zone presents a challenge to the coarse scale passive microwave observations of snow cover, in particular due to the highly variable and partly dense vegetation. Vegetation affects the emission signatures both directly through attenuation, scattering and emission from the forest canopy (e.g. De Roo *et al.*, 2007), and indirectly by affecting snow distribution and metamorphosis, compared to open areas such as tundra (e.g. Sturm *et al.*, 1995). Land cover features such as bogs and other wetlands, as well as lakes and rivers provide further complexity to the observed scene. The snow background in general has a substantial effect on the detected emission. This is emphasized in the lower end of the microwave spectrum, where increasing wavelength results in higher penetration depth into the ground surface, whereas snow has a decreasing influence.

Airborne observations reported in [P1], measured by separate groups in Finland and Canada, provided data at high spatial resolution (< 100 m) on the passive microwave signatures of snow cover in the boreal forest zone. The measurements complement earlier studies (e.g. Mätzler, 1994; Kurvonen and Hallikainen, 1997; Goita *et al.*, 2003; Roy *et al.*, 2004), but also provide new insight in particular into the differing signatures of wetlands when compared to forested areas. The datasets also enabled independent verification of the original HUT snow emission model (Pulliainen *et al.*, 1999) over varying terrain. Further airborne observations of lake ice emission signatures in [P3] provided data for validation of the multiple layer model (Lemmetyinen *et al.*, 2010, [P2]) when applied for snow covered lake ice. This enabled to apply the modified model also to simulate the complete satellite scene in lake rich areas in [P4].

Furthermore, L-band radiometer observations from a tower-based experimental campaign enabled the examination of the effect of ground freezing and thawing processes on the microwave signature; as the ground freezes, the soil permittivity decreases as free water content in the soil diminishes. This can have a detectable effect also at higher frequencies, but the signature is in part masked by the presence of snow cover. However, the snow has a minimal effect at L-band frequencies and the changes in emission due to soil processes can be reliably isolated. For this study, a layered emission model was defined to simulate the emission from partially frozen soils [P5]. Modeled emission signatures were compared to measured emission at L-band during the freezing period at the experimental site.

The results presented in this section summarize the main findings from [P1] - [P5], placing these into context with one another and the overall goals of the thesis work. Specifically, the following issues are addressed

- Effect of land cover and vegetation on brightness temperature of snow-covered terrain ([P1])
- Capability of HUT snow emission model to estimate these effects ([P1])
- Capability of a modified snow emission model to simulate brightness temperature of layered snowpacks at a point scale [P2]
- Capability of a modified snow emission model to simulate the special case of snow-covered lake ice at point scale ([P3]) and on satellite scale ([P4])
- Effect of soil freeze/thaw processes in winter conditions on observed brightness temperature at L-band frequencies ([P5])

6.1. Effect of land cover features on microwave signatures

The study in [P1] describes airborne microwave radiometer datasets collected over the boreal forest regions of Finland and Canada, and application of the original HUT snow emission model in the simulation of the detected microwave emission. The airborne data are complemented by comprehensive *in situ* data on snow conditions, as well as land cover information. The airborne sensors used included typical frequencies applied in microwave remote sensing of snow (19 and 37 GHz), as well as a lower frequency channel (6.9 GHz). The datasets were acquired close to the peak snow season in March/April over two years (2005 and 2006). Maps of the study areas are provided in Figure 8, and a summary of the datasets in Table 3; the data are divided into four sections, or flight lines, labeled A to D. The Finnish 2005 flight line C in Southern and central Finland consists primarily of conifer-dominated boreal forests with a considerable number of bogs and lakes. Flight Line D, flown in Northern Finland in 2006, included a transition from forest to open terrain in the subarctic tundra region. While the Finnish datasets are relatively heterogeneous especially in the case of flight line C, with agricultural fields, wetlands and different forest types, the Canadian data in flight lines A and D are predominated by sparse open-canopy boreal forest, tundra and shallow tundra lakes. The portion of lakes is notable in particular over flight line A in the Canadian Northwest territories, while flight line B is predominantly forested. Consequently, the Finnish land cover was categorized into five classes (dense forests, sparse forests, open (dry) areas, bogs and lakes). For the Canadian data, only three land cover classes were defined (forest, tundra and lakes).

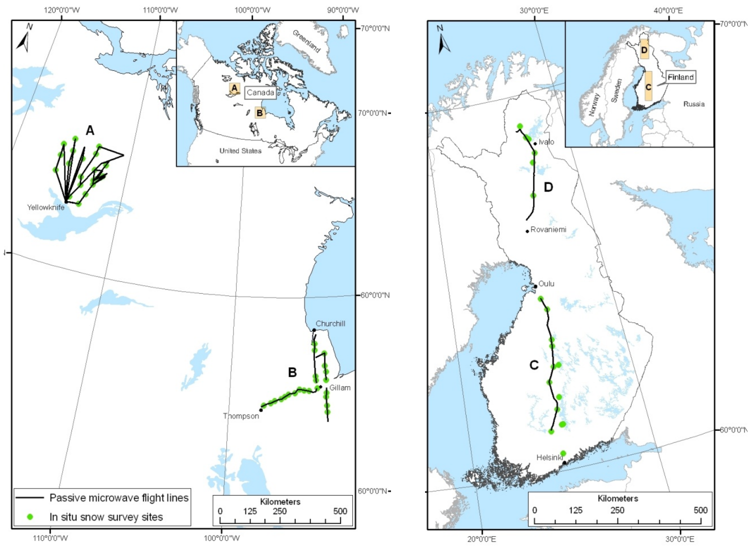

Figure 8. Overview of ground and airborne sampling sites during 2005 and 2006 airborne passive microwave campaigns in Canada (left) and Finland (right). Flight lines A to D indicated. *Lemmetyinen et al. (2009) [P1].* © 2009 IEEE.

TABLE 3: SUMMARY OF AIRBORNE CAMPAIGNS CONDUCTED IN FINLAND AND CANADA. *Lemmetyinen et al. (2009) [P1].*

	Canada		Finland	
Flight line	A	B	C	D
Dates of Deployment	April 3-18 2005	February 28-March 13 2006	March 14 2005	March 16-17 2006
Study Domain	Snare and Yellowknife basins, Northwest Territories. Ground measurements at 15 locations	Nelson watershed, Manitoba. Ground measurements at 25 locations	Southern Finland. 6 snow course observation sites 13 additional observation sites	Northern Finland. 4 snow course observation sites 6 additional observation sites
Dominant ground types	Forested: 48% Tundra: 29% Lakes: 23%	Forested: 60% Tundra: 27% Lakes: 13%	Dense forest: 51% Sparse forest: 7 % Open areas: 9% Bogs: 3 % Lakes: 10%	Dense forest: 46% Sparse forest: 11% Open areas: 12% Bogs: 14% Lakes: 3%
Ground Measurements	Snow depth Snow water equivalent Snow density profiles Snow grain size profiles		Snow, soil, air temperature Snow depth Snow density and moisture profiles Snow grain size profiles and photographs	

6.1.1. Effects of land cover and snow conditions

The investigated transects in Finland and Canada exhibited a range of snow conditions. The extent of measured values for snow depth, SWE, grain size and density are summarized in Figure 9. Several statistical features are noted in [P1] regarding the measured range of brightness temperatures, which can be linked to the prevailing snow and land cover conditions. The Finnish datasets show a high variability in SWE, in particular for flight transect C reflecting also the larger range of land cover types represented in the data. For Canadian data the variability of SWE was smaller for both datasets. The measured snow density was relatively uniform also for the Finnish dataset; therefore, the variability in SWE was mainly a result from the large variability in snow depth.

Bulk grain size in the flight line C dataset (measured grain size averaged over the whole snowpack in the vertical direction) ranged from a typical value of 1 mm in a 5-10 cm surface layer to up to 2 mm in several bottom layers. The data for flight line D showed similar thin surface layers but mostly homogenous snowpacks below the surface, with a mean grain size smaller than 2 mm. The Canadian datasets exhibit significantly larger grain growth, in particular for 2005 (flight line A). As pointed out in [P1], this is due to the significant depth hoar layer present in Canadian snowpacks, which increases the bulk average grain size over the whole snowpack. The differing snow grain properties between Finland and Canada were highlighted previously by Roy *et al.*(2004) as a major factor influencing the applicability of the HUT snow emission model to Canadian boreal snow packs.

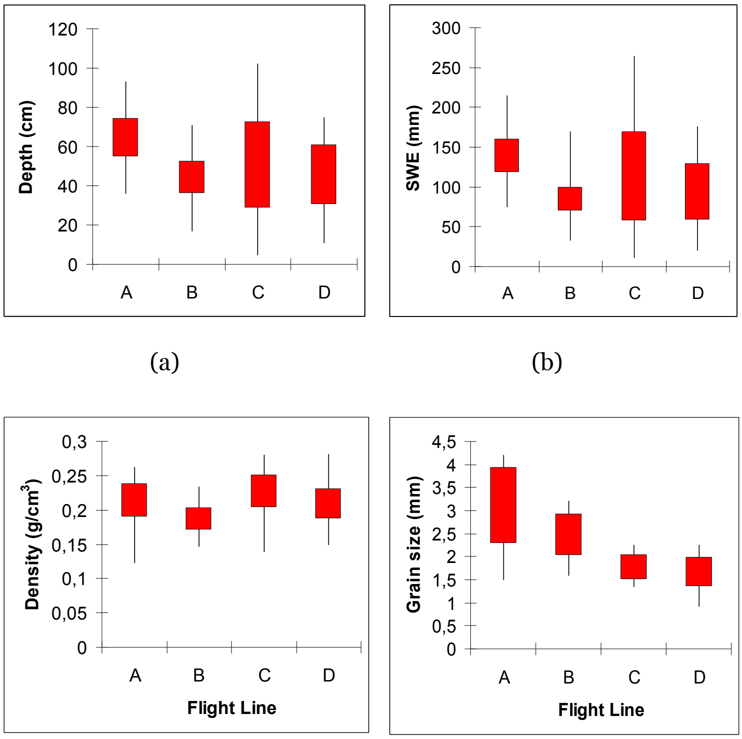

(c) (d)

Figure 9. Boxplots of snowpack properties on flight lines A to D: SWE (a), depth (b), density (c), and grain size (d). *Lemmetyinen et al. (2009) [P1].* © 2009 IEEE.

Figure 10 shows a summary of the airborne brightness temperatures measured over flight lines C and D (in Finland) in 2005 and 2006, respectively. The data are represented as average values over different land cover types (dense forests, sparse forest, open areas, bogs and lakes). Error bars represent the standard deviation of observed values. The 6.9 GHz signature can be seen to be similar over dry land for both flight lines at both polarizations; the amount of vegetation appears to have little effect (< 1K difference in mean values between dense forests and open terrain). However, lakes exhibit a strong (~50K) difference to surrounding dry land. Interestingly, bogs show a ~5K contrast to dry land surfaces for H-polarization over flight line C; a similar contrast is seen at V-polarization over flight line D. The strong influence at 6.9 GHz was noted also in [P1] (Figure 6).

The strong influence of lakes at the lowest frequency was an expected result; the contrast is still discernible at 18.7 GHz in Figure 10 (b) and (e). An 8-10 K contrast to dry land is apparent for both polarizations (note that data for 18.7 GHz V is missing for flight line D). This would already carry a significant impact on SWE estimates based on the 18.7 – 36.5 GHz channel difference, the exact impact depending on the fractional coverage of lakes in the satellite scene. It is worth noting that the snow cover already represented late winter conditions in terms of SWE; for early season estimates, the impact would likely be larger (due to reduced attenuation of snow cover). Other land cover types over dry land show some variability at 18.7 GHz. A 3 K contrast between open terrain and densely forested areas is apparent for vertical polarization. This is likely a combined effect of vegetation and differing snow properties in forests compared to open areas.

At 36.5 GHz, the effect of varying land cover over dry terrain becomes apparent. Densely forested areas show the highest brightness temperatures (mean value 236 K and 323 K for V and H polarizations, respectively), while open terrain emissions are 10-12 K lower. Also the standard deviation of the measured values is much higher than at lower frequencies, reflecting both the influence of varying snow cover and vegetation. The standard deviation is, however, of similar magnitude (11-13 K) for both open and vegetated areas, which would suggest the variability is mostly driven by snow conditions. Interestingly, the snow covered lakes no longer give the lowest emissions over flight line C (although they do so for flight line D in 2006), being of similar magnitude to emission from open terrain. This may reflect the generally denser and thicker snow conditions for flight lines C (in 2005) and D (in 2006), see Figure 9. For 2006, the shallower and less dense snow would allow a larger part of the emission to originate from the medium underneath the snow, thus decreasing brightness temperatures over lakes also at 36.5 GHz. Furthermore, it is notable that bogs show a clear (~15-20 K) contrast in emission compared to other land surfaces, including non-vegetated areas over dry terrain. This suggests that snow conditions over bogs differ significantly from other open areas.

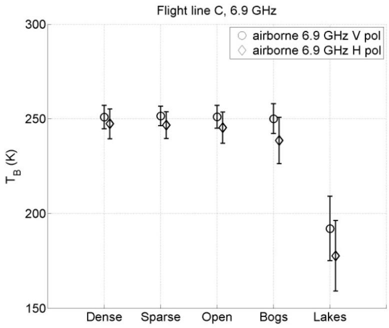

(a)

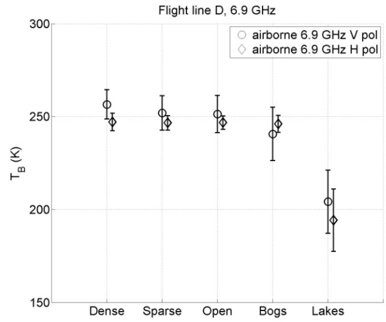

(d)

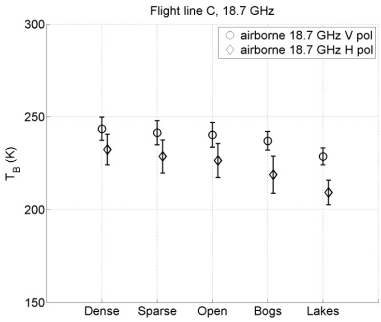

(b)

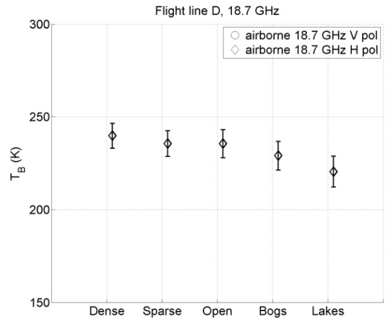

(e)

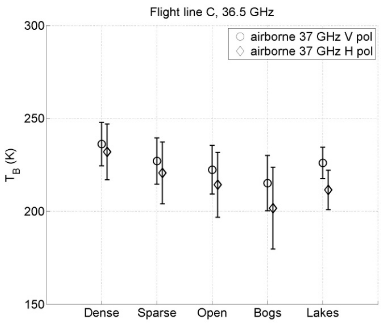

(c)

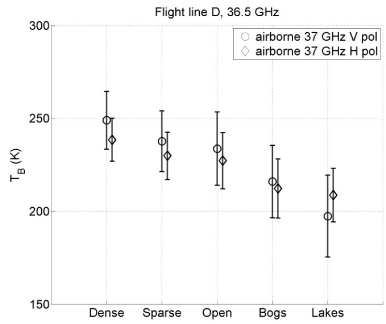

(f)

Figure 10. Brightness temperature distribution per land cover type on Flight transects C and D (Finland). Mean and std (error bars) of H- and V-polarized brightness temperature at 6.9 (a) & (d), 18.7 (b) & (e) and 36.5 (c) & (f) GHz. Note: data for 18.7 GHz V pol on flight line D missing. From data in Lemmetyinen *et al.* (2009).

Figure 11 shows a reanalysis of data for flight line C presented in Figure 5 of [P1], showing the sensitivity of the 18.7-36.5 GHz brightness temperature difference (vertical polarization) to SWE over various land cover types (in place of individual frequencies displayed in [P1]). This frequency combination is typically considered sensitive to increase in SWE (e.g. Chang *et al.*, 1987). As discussed previously, microwave attenuation and emission from a dense vegetation cover may mask out any changes in the snow cover beyond possibility of detection by remote sensing instruments. In Figure 11, densely forested areas can clearly be seen to exhibit the lowest response in the brightness temperature difference to increase in SWE. Sparse forests, in turn, show sensitivity up to 80-100 mm in SWE but not beyond. Open areas (i.e. non-forested) show similarly a sensitivity up to 60-80 mm. However, data collected over bogs show sensitivity up to 100-120 mm, which is close to the traditionally expected saturation limit of the 36.5 GHz signal attenuation in snow. Results over lake ice are in this case ambiguous; for low SWE values, the channel difference is negative, and very little response is seen with increasing SWE. For this study, however, the SWE over lakes was not measured directly. Rather, the SWE was assumed to be identical to that measured over bogs.

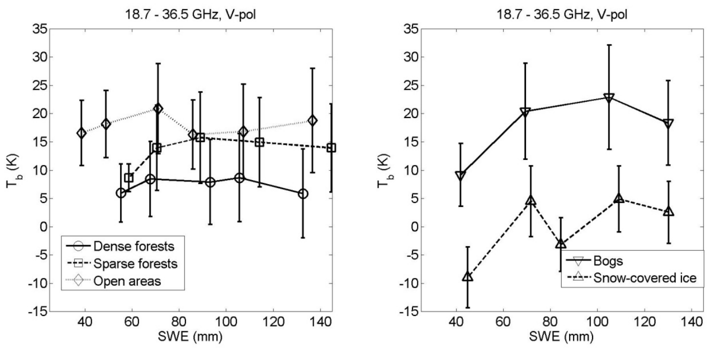

Figure 11. Brightness temperature vs. surface SWE measurements for different land cover types, flight line C in Finland. Difference of 18.7 and 36.5 GHz. Total number of samples was 2213 for dense forests, 312 for sparse forests, 401 for open areas 453 for lakes and 148 for bogs. Accordingly, each data point corresponds on average to 442 (dense forests), 62 (sparse forests), 66 (open areas), 37 (bogs) and 90 samples (lakes). From data in Lemmetyinen *et al.* (2009).

Figures 10 and 11 emphasize the effect of land cover and vegetation on the brightness temperature and its sensitivity to SWE. An emission model describing a heterogeneous scene consisting of several of these land cover types must correctly predict their effect on the total observed emission. In [P1], the original HUT snow emission model was applied to simulate the brightness temperature over areas covered by the airborne observations. The aim was to assess the model performance over varying land cover, vegetation and snow conditions. The airborne dataset in [P1] is particularly useful for assessing the performance of the empirical vegetation compensation component (Kruopis *et al.*, 1999). In the following, the modeling results in [P1] are analyzed by land cover type.

6.1.2. Simulations using original HUT snow emission model

Available snow, land cover and vegetation data were applied to run the HUT snow emission model (Pulliainen *et al.*, 1999), attempting to quantify the model performance in simulating the varying boreal forest landscapes observed in Finland and Canada. The modeling work was limited to vertical polarization, as this is typically the polarization applied for retrieval of SWE due to the smaller sensitivity to layering effects (e.g. Kelly *et al.*, 2003).

Figure 12 demonstrates a summary of the simulation results for flight line C (Finland in 2005), for the three investigated frequencies. Simulations were made for four land cover types; lakes were not included as the original HUT snow emission model was not adapted for water surfaces. The 6.9 GHz channel is largely insensitive to the snowpack, and the simulation result is mostly dependent on the soil emission simulation (applying empirical model by Wegmüller and Mätzler, 1999). One possibility would be to use the 6.9 GHz channel for deriving effective surface parameters by numerically fitting the model to observations, but in [P1] static values for the soil parameters were applied; the permittivity of frozen soil was considered to be 6-j, and the effective surface roughness 3 mm, resulting in a 3-7 K overestimation in the simulation results. At 18.7 GHz, the modeling errors are smaller, ranging from 1 to 4 K (bias error). At 37 GHz, however, larger errors emerge for the non-vegetated areas (bogs and open areas); here the model results show a clear, 10-12 K overestimation, compared to relatively low errors for densely and sparsely forested areas (under 5 K). This indicates a possible underestimation in either the grain size or snow mass.

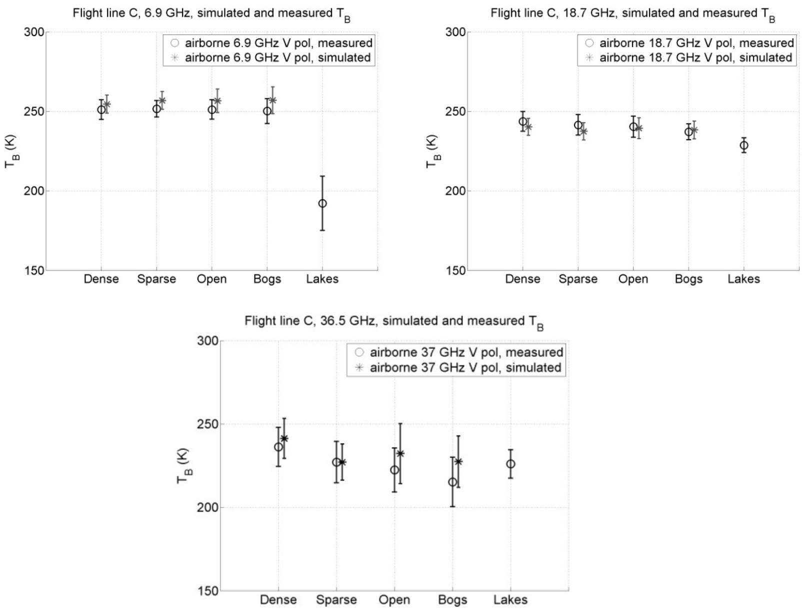

Figure 12. Observed and simulated brightness temperatures over flight line C (Finland), separated by land cover type. Results for vertically polarized emission at 6.9, (a), 18.7 (b) and 36.5 GHz (c). From data in Lemmetyinen *et al.* (2009).

A summary of simulation results is shown in Table 4 for all examined frequencies (vertical polarization) and flight lines.

In forested areas, the model estimates indicate good agreement with airborne measurements at 19 and 37 GHz for transects C and D (in Finland), indicating reasonable performance of the vegetation compensation model component and quality of the vegetation data. However, the model clearly underestimates brightness temperature with both Canadian datasets at these frequencies over forested areas (flight lines A and B, see Table 4). In terms of bias, the model simulations underestimate brightness temperature by 31 and 21 K for 19 and 37 GHz for flight line A, while for flight lines C and D (in Finland) the match is better than 8 K and 7 K, respectively. The better results for Finland may reflect also the more precise forestry data available; the original model formulation for vegetation (Kruopis *et al.*, 1999) was made based on comparing vegetation biomass against measured changes in brightness temperature. As for the Canadian data, a proxy value of forest biomass had to be used, the larger errors may partly be attributed to this.

Non-vegetated areas allow examining the performance of the snow emission model itself, while the observed and simulated microwave emission for forested areas is mostly driven by vegetation. For the 19 and 37 GHz frequencies, the simulation results over flight lines C and D again follow closer the observed airborne values than for flight lines A and B. For the Canadian flight lines, the model simulations again underestimate the measured brightness temperatures. Compared to forested sites, the errors are even larger, with the exception of the 19 GHz simulation over flight line B. The bias errors range up to -14 K and -25K for 19 and 37 GHz, respectively, while RMS errors exceed 24 K for 37 GHz for both flight lines and flight line A for 19 GHz. This is an indication that the single-layer model is not suitable for the simulation of tundra snow type, which is characterized by a distinct depth hoar layer with rough snow grains. The dielectric contrast between the depth hoar layer and the surface snow layer will induce reflection components not captured by the one-layer model. Furthermore, the original empirical formulation of the snow extinction coefficient in the HUT model by Hallikainen *et al.* (1987) is limited to snow grain size below 1.6 mm, which is insufficient for the larger snow grains present in the Canadian dataset. As an empirical solution, e.g. Roy et al (2004) modify the snow extinction calculation for simulation of large grains. In [P1], applying the modified formulation for large grains was seen to decrease the modeling errors.

TABLE 4. RMS AND BIAS OF ERROR FOR MODELED VS. AIRBORNE BRIGHTNESS TEMPERATURES ON FLIGHT LINES A, B, C AND D. VALUES IN KELVIN.

Channel	6.9 GHz		19 GHz		37 GHz	
	RMS	bias	RMS	bias	RMS	bias
A (Canada)						
forest	12.8	12.1	13.2	7.6	13.5	9.0
tundra	12.3	8.6	25.6	13.7	38.5	24.3
B (Canada)						
forest	6.8	5.4	37.0	31.3	24.6	20.5
tundra	1.7	1.7	8.3	7.7	24.9	24.7
C (Finland)						
dense forest	5.7	3.5	5.3	-3.5	12.0	5.1
sparse forest	5.6	5.2	5.5	-4.1	10.9	0.0
open	7.4	5.5	6.5	-1.0	18.0	9.8
bogs	8.4	6.8	5.6	1.2	15.4	12.2
D (Finland)						
dense forest	12.3	11.6	8.8	7.8	11.1	0.3
sparse forest	12.0	11.7	6.8	3.1	14.0	-6.5
open	13.1	11.9	9.9	7.3	17.0	7.8
bogs	12.9	12.3	4.9	0.5	19.6	-12.1

In summary, the original HUT snow emission model, together with the soil surface and vegetation emission model components, was demonstrated to be able to simulate the observed airborne brightness temperatures with reasonable accuracy for boreal forest landscapes. Modeling errors for tundra areas, however, were notably high. Errors originated either from insufficient modeling of physical components affecting the emission (e.g. in the case of bogs for the Finnish dataset), insufficient data (in the case of forested areas, in particular flight line B) or failures in the model itself (in the case of tundra snow at 37 GHz). A clear shortcoming of the model was the lack of a lake ice emission simulation component, as lakes represented c.a. 15 % of the whole dataset. This formed a main incentive to upgrade the emission model to simulate also the brightness temperature of layered snowpacks, including structures such as frozen, snow covered lakes. This is addressed in the following sections.

6.2. Layered snowpacks

The multiple layer modification of the HUT snow emission model (section 5.2) was also evaluated against experimental data from Finland and Canada, in order to quantify the potential improvement of simulation results when accounting for the vertical structure of snow. Such improvement has previously been reported when applying other radiative transfer based models (e.g. Hall *et al.*, 1987, Durand *et al.*, 2008). Snow pit data from a fixed site in Sodankylä, Finland and from several sites in the Canadian Northwest territories were used to run the HUT multiple layer modification, comparing model estimates against ground-based radiometer observations for the sites (Lemmetyinen *et al.*, 2010 [P2]). Errors of the estimated brightness temperatures were evaluated against those produced by the original, single layer model.

6.2.1. Datasets

NWT distributed sites

The first dataset used for evaluation of the multiple layer model was collected from spatially distributed sites. The aim was to assess the model performance over a range of snow and snow background conditions. Measurements performed by Environment Canada at ten tundra sites in the Canadian Northwest Territories (NWT) were used for evaluation of the performance of the layered model. The data were collected over a 5-day period in April 2007. Measurements at each site consisted of radiometer observations over a single location, with a snow pit measurement made directly from the footprint of the instruments. Three of the sites were situated over frozen, shallow tundra lakes. All sites represent a typical tundra snow regime with average densities ranging from 0.3 to 0.4 g/cm^3. The radiometer observations consisted of dual-polarization measurements at 6.9, 19, 37 and 89 GHz; the radiometers were mounted on a mobile sled allowing easy transportation between sites. The radiometers were calibrated with two-point antenna calibration loads before and after the campaign. Calibration drift was estimated to be approximately +/- 8 K at 6.9 GHz, +/- 2 K at 19 GHz, < 1 K at 37 GHz, and +/-4 K at 89 GHz ([P2]).

Snowpit observations at the NWT sites consisted of a bulk depth and density measurement of the snowpack, density and grain size profile measurements and snowpack stratigraphy observations. The snowpit measurements for each site are summarized as a bar chart in Figure 13. Snow layering was determined visually, with grain size estimates made for each layer by examining grains on a visual reference grid. A precipitation event during above-zero conditions had resulted in the formation of a distinct ice lens on top of the snow surface (Rees *et al.*, 2010). The ice lens was observed at all sites, with some sites having a shallow layer of new snow on top of the lens. The physical structure of the lens allowed it to be manually removed with minor disturbance of the snowpack beneath; the NWT dataset contains radiometer observations of the sites both for the undisturbed snowpack (i.e. with the ice lens) and the ice lens removed.

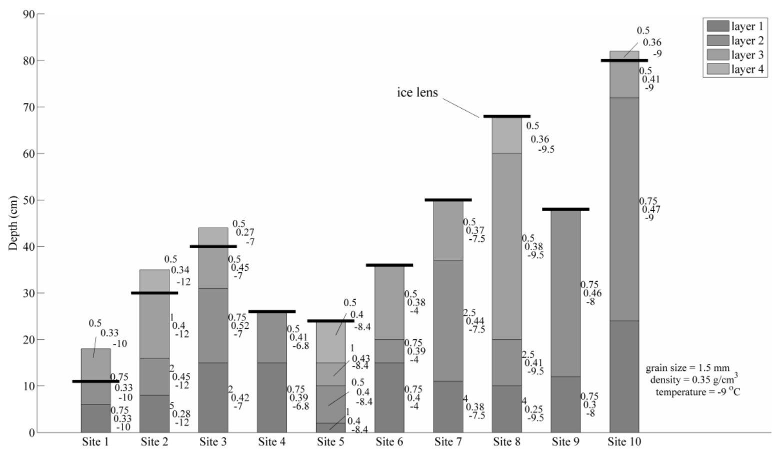

Figure 13: Observed snowpack layering, grain size & density profiles at NWT sites. Sites 4, 5 and 6 are lake sites, remaining sites are tundra. Location of ice lens indicated with thickened horizontal lines. Numbers to the right of each layer correspond to grain size (in mm), density (g/cm3) and temperature (°C). *Lemmetyinen et al. (2010) [P2].* © 2010 IEEE.

Time series observations at fixed site

The second dataset used for model validation was collected at the Arctic Research Centre of the Finnish Meteorological Institute (FMI-ARC) in Sodankylä, Finland, between the 5th and 13th of March, 2008. The site represents typical boreal forest snow conditions and vegetation (coniferous forest); the measurement site itself was located in a forest clearing. The purpose of this dataset was to assess the model performance at a single site, over temporally changing conditions. Radiometer observations consist of dual-polarization observations at 18.7, 36.5 and 94 GHz using the HUTRAD radiometer system (see section 3.4). Instead of the usual aircraft installation, the radiometer receivers were mounted on a ~8 m tower, with antennas observing the chosen study area of approximately 5 x 5 meters at an incidence angle of 55°. The system was calibrated twice per day with a two-point calibration technique at the antenna reference plane. *A posteriori* analysis of the calibration results showed a 1-4 K drift in the calibration, depending on the channel. Although the system was set to measure a continuous time series, the observations used in [P2] were restricted to within +/- 10 minutes from calibrations to minimize errors from the drift. Snow conditions at the site remained stable until March 10th, when rising temperatures caused the onset of snowmelt.

Ground data for the Sodankylä dataset consisted of snow grain size, temperature, layering and density profile measurements. A track of approx. 20 meters, situated 5-10 meters from the test area was designated for the snow pits. A 1-2 m section of snow from the track was removed each time before establishing a new measurement site (snowpit). A total of 18 snow pit measurements were made, all during daytime. In the Sodankylä data, the total amount of observed distinct layers in the snowpack varies between four and nine. Snowpit measurements occurred very close to each other (less than 2 m), and it is difficult to determine whether the large variation in layering was due to interpretation errors or true variations in the snowpack. Some common features can be observed, however, at least for the period of dry snow. Firstly, a bottom layer of 20-40 cm, consisting of large depth hoar grains was identified in all the observed snowpits. This layer was clearly discernible, and the results can be used as an indication of the local variability in depth of the lowest layer. Similarly, all observations report a surface layer with small average grain sizes (0.2 to 1 mm), albeit with varying depth. The amount and structure of intermediate layers varies the most; this may then be both due to variations in the snowpack itself and observation uncertainties. The bulk snow conditions at Sodankylä were comparable to the NWT sites with intermediate levels of SWE (100-150 mm), although the vertical properties were different as the NWT data represent tundra snow (strongly wind influenced) and the Sodankylä data represent boreal forest snow conditions.

6.2.2. Simulations using modified emission model

Both the original single-layer HUT model, as well as the multiple layer adaptation presented in section 5.2, were applied to simulate the microwave emission for the ten NWT sites as well as the time series of the Sodankylä site, comparing simulated values to radiometer observations. The sites represent very different types of snow regimes, the NWT sites representing densely packed tundra snow with varying snow depth, and the Sodankylä site representing a typical boreal forest snow regime with reduced wind effects (densification). Therefore, the simulations allow assessment of the model performance over a wide range of snow conditions.

Simulation results for the Sodankylä time series dataset are shown in Figure 14. A qualitative analysis indicates that trends seen in the observational data during the dry snow are not apparent in the simulated brightness temperatures (e.g. the ~20 K increase of brightness temperature at 18.7 GHz H-polarization, or the drop of brightness temperature on March 9^{th}). This is not necessarily a fault of the model, but may rather reflect the incompleteness of the ground reference data. For example, the model input data did not include a measured component for the downwelling atmospheric contribution (reflected from the snow surface). This may carry a significant effect at higher frequencies (here, 37 and 94 GHz). Rather, the variability seen in simulated values is directly related to the variability of measured snow properties. Snow conditions remained stable during the simulated dry snow period, but the snow pit measurements used to drive simulations show e.g. a range of 52 to 61 mm in the bulk snow water equivalent. Since 1) snow pits were not made directly in the footprints of the radiometer and 2) they were made from a different location each time, this variability reflects the magnitude of random errors related to the snow pit observations.

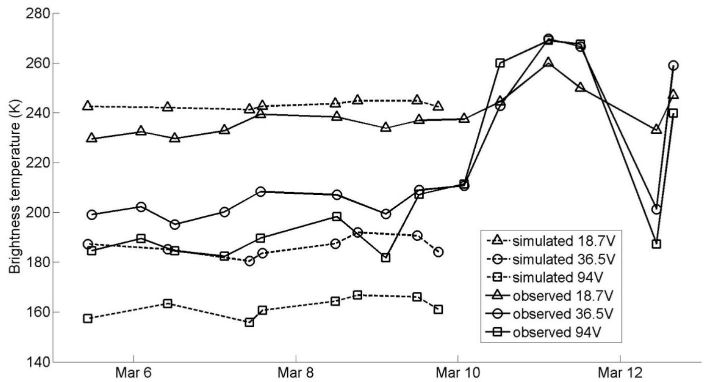

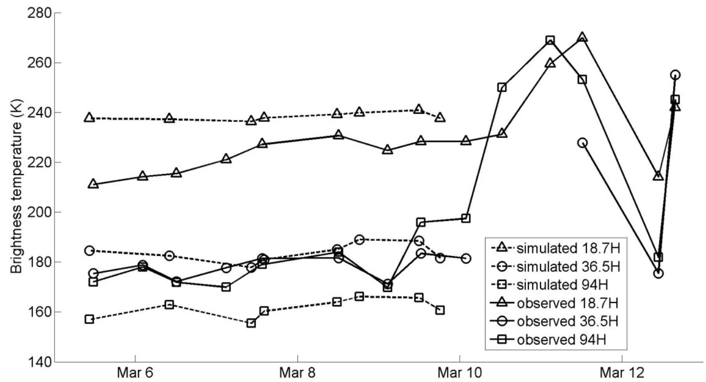

Figure 14: Time series of modeled and observed brightness temperatures from 5th to 12th March, 2008 at FMI-ARC Sodankylä site. Model values calculated using multiple layer adaptation. Dry snow conditions before March 10th. Night-time observations (calibrations) on March 8 and March 12 were not considered due to technical reasons. Two 36.5 H-pol observations between March 10 and 11 are likewise lacking due to a technical failure. *Lemmetyinen et al. (2010) [P2].* © 2010 IEEE.

Figure 15 and Table 5 summarize simulations from both the NWT and Sodankylä sites relative to observations. For the Sodankylä data, the results represent simulations for the dry snow period until March 10th. The uncertainty of the observations, given in Figure 15 as error bars, was derived from the standard deviation of observations during that time period. The uncertainty of simulation was similarly obtained from the standard deviation of simulation results; the uncertainties are again depicted by error bars in the figure.

For the NWT dataset, using the multiple layer model was found to reduce error indicators at almost all of the investigated frequencies and polarizations. At the lower two frequencies the improvement is marginal, being between 0.8 to 3.9 K and 0.1 to 2.8 K for reduction of bias and RMS errors, respectively. At 37 and 90 GHz, however, the bias errors are reduced between 3.3 (37 GHz H) and 13.6 K (90 GHz V), and RMS errors between 5.3 K (37 GHz H) and 12.7 K (90 GHz V). In particular, the attained bias errors are notably low compared to those of the one layer model. Considering individual sites, the sites with the largest SWE values (sites 7-10) show the highest rate of improvement in simulation results. However, in particular for the lowest frequency band of 6.9 GHz, large errors remained especially over the lake sites (sites 4, 5 and 6).

For the Sodankylä time series dataset, use of the multiple layer model adaptation generally improves modeling results at the higher frequencies of 37 and 94 GHz for vertical polarization. However, the layered model induces an increase in bias and RMS errors at the lowest frequency of 18.7 GHz. Also, simulation results for 36.5 GHz, H-pol are deteriorated, albeit marginally (by 1.1 K for bias and 0.9 K for RMS errors). Compared to the NWT dataset, also the simulation errors at vertical polarization remain large (8.4, -17.2 and -30 K compared to 5.3, -2.5 and -5.4 K for 18.7/19, 36.5/37 and 89/94 GHz, respectively). The large errors may be due to the aforementioned protocol used for assessing the snowpack; the snow pit measurements were not made directly from the instrument footprint, and due to the nature of the measurements, had to be made from a different location each time.

The HUT model does not account for wave coherence effects arising in thin layers with a thickness less than about half the observed wavelength. The ~3 mm ice lens present at the NWT sites (see Figure 13) was likely to induce coherent effects at the lower two observed frequencies, the half-wavelength being 21.7 mm and 7.9 mm, respectively. Consequently, in the above analysis of the HUT model evaluation, observations made after manual removal of the ice lens were applied. Simulation results including the effect of the lens are included in [P2]; parts of the same dataset have also been applied by Rees *et al.* (2010), using MEMLS and the original HUT snow emission model.

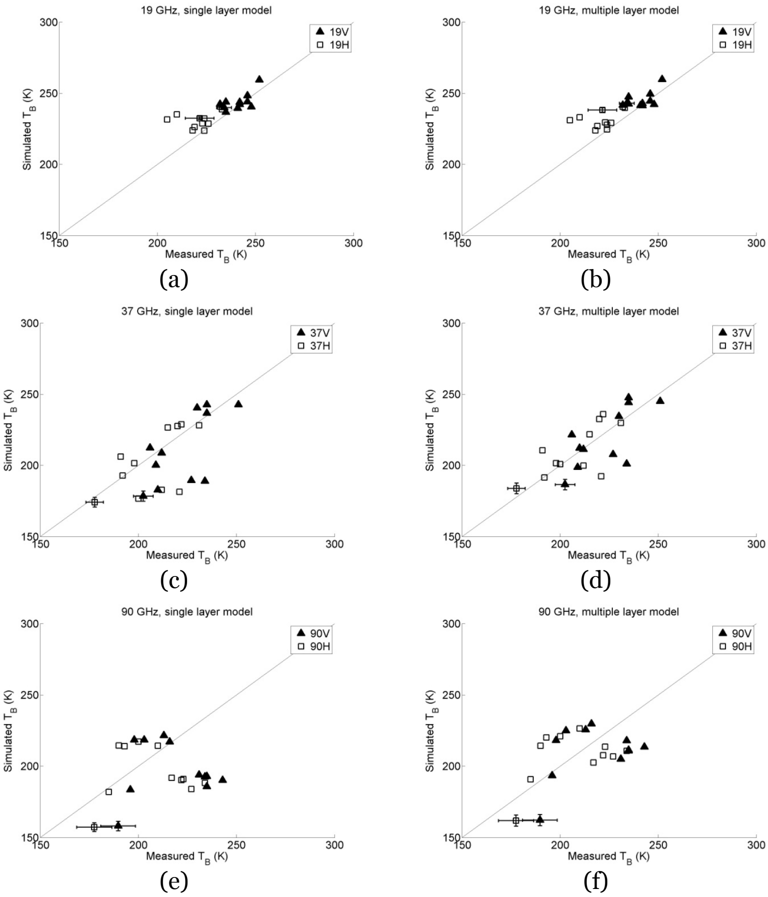

Figure 15: Scatterplots of simulation results in [P2] for Sodankylä and NWT datasets. Comparison of model estimates and observations for single layer model (left) and multiple layer model (right) for 19 GHz (a), (b); 37 GHz (c), (d); and 90 GHz (e), (f). Results from [P4] applied. Errorbars show the standard deviation of observations and model simulations over the dry snow period in the Sodankylä dataset.

TABLE 5: SUMMARY OF SIMULATION ERRORS FROM NWT AND SODANKYLÄ SITES. BIAS, RMSE AND UNBIASED RMSE WHEN USING SINGLE AND MULTIPLE LAYER MODELS, AND CHANGE IN ERROR INDICATOR VALUES (MULTIPLE – SINGLE-LAYER MODEL ERRORS).

	Simulation agreement with observations for single layer model (K)								
	Channel	6.9 GHz		19 GHz		37 GHz		89/94 GHz	
		V	H	V	H	V	H	V	H
NWT distributed sites	Bias	4.3	6.1	4.5	12.3	-10.4	-4.9	-19	-11.4
	RMSE	13.4	14.5	7.7	14.7	21.3	18.6	33.2	28.2
	uRMSE	12.7	13.2	6.2	8.1	18.7	18	27.2	25.8
Sodankylä site time series	Bias	-	-	5.1	10	-25.7	-4.4	-35.2	-23.6
	RMSE	-	-	6.3	12.2	26.5	7	37.1	26.1
	uRMSE	-	-	3.8	7.1	6.4	5.4	11.8	11.3
	Simulation agreement with observations for multiple layer model (K)								
	Channel	6.9 GHz		19 GHz		37 GHz		89/94 GHz	
		V	H	V	H	V	H	V	H
NWT distributed sites	Bias	2.2	2.2	5.3	11.5	-2.5	1.5	-5.4	1.3
	RMSE	10.6	12.9	7.6	13.8	14.5	13.3	20.5	18.8
	uRMSE	10.4	12.7	5.5	7.6	14.3	13.2	19.7	18.7
Sodankylä site time series	Bias	-	-	8.4	15.8	-17.2	5.5	-30	-18.1
	RMSE	-	-	9	17	18.3	7.9	31.6	20.5
	uRMSE	-	-	3.3	6.1	6.1	5.7	10	9.6
	Difference of model errors (multiple - single layer model) (K)								
	Channel	6.9 GHz		19 GHz		37 GHz		89/94 GHz	
		V	H	V	H	V	H	V	H
NWT distributed sites	Bias	-2.1	-3.9	0.8	-0.8	-7.9	-3.4	-13.6	-10.1
	RMSE	-2.8	-1.6	-0.1	-0.9	-6.8	-5.3	-12.7	-9.4
	uRMSE	-2.3	-0.5	-0.7	-0.5	-4.4	-4.8	-7.5	-7.1
Sodankylä site time series	Bias	-	-	3.3	5.8	-8.5	1.1	-5.2	-5.5
	RMSE	-	-	2.7	4.8	-8.2	0.9	-5.5	-5.6
	uRMSE	-	-	-0.5	-1	-0.3	0.3	-1.8	-1.7

6.2.3. Synthesis of HUT model modification for layered snowpacks

The results indicate that the multiple layer modification of the HUT snow emission model produces improved results when compared to those from the original single-layer model, provided that the necessary ancillary information is available. For simulations representing sites in the Canadian tundra region, use of the multiple layer model was seen to decrease modeling RMS errors by 6 to 38 % for horizontally polarized channels and 1 to 38 % for vertically polarized channels, depending on frequency. The overall bias errors were also reduced. Generally, higher frequencies and sites with the largest SWE values showed the highest level of improvement in simulation results. For the second dataset used for model evaluation, results were somewhat more ambiguous. Simulations for the boreal forest site in Finland improved only for some of the examined channels when applying the multiple layer model. This may be related to the quality of the available *in situ* information, which was not collected directly at the footprint of the instrument. Moreover, snow layering was found to be much more complex than for the Canadian site; *in situ* measurements identified up to eight layers within the snowpack, while NWT sites produced a maximum of four distinct layers. Considering the variability of snow even at the short range (e.g. Sturm *et al.*, 2004), it is uncertain if the layering was thus representative of the snow in the footprint of the radiometers. The simulations show that attempting to account for the effects of snow layering using the revised HUT snow emission model may in some cases deteriorate the model results, in particular if the determination of stratigraphy is uncertain.

Nevertheless, the study confirms earlier findings and theory which state that the snow layering carries an increasing effect with increasing frequency, being also more prominent for horizontal polarization. It is demonstrated that these effects can be addressed on a point scale with a relatively simple stacked model representing the vertical stratigraphy of the snow. This has important implications for the use of the model in estimation of snow parameters; it is clear that use of the one layer model may produce erroneous results for cases where snow layering is distinct also at the satellite scale. However, small scale variability in the snowpack will make simulating the overall effect difficult. Special cases where this may be done may arise as with the case of ice lens formation consistent over a large region, as reported by Rees *et al.* (2008). By coupling the emission model with a thermodynamic model predicting snow states (e.g. Brun *et al.*, 1989), the new model could be applied to potentially further improve retrieval of snow properties in model inversion schemes such as reported by Takala *et al.* (2011). One further potential application is the application of the model to account for the presence of snow covered lake ice within observed scenes, which significantly decreases estimation accuracy for lake rich areas. Frozen, snow-covered lakes form distinct layered systems which may be predicted with relative ease compared to snow layering on dry terrain. The application of the model for this purpose is presented in the following sections.

6.3. Brightness temperatures of frozen lakes

In microwave radiometer observations of the Earth, water bodies form a distinct contrast in brightness temperature when compared to dry terrain throughout most of the microwave range. This contrast persists also in winter conditions for wavelengths able to penetrate the snow and ice overlying the lakes, creating a need to account for the diverse emission signatures when simulating the microwave emission of scenes with a significant fractional coverage of lakes. Studies in [P3] and [P4] apply the multiple layer forward model (section 5.2) for this purpose. In [P3] a dataset of airborne observations is used to verify model estimates, while in [P4] the simulations are extended to the scale of satellite observations.

In both studies, several simplifications of the modeled physical ice-snow system are made. A schematic of the simulated structure of snow covered frozen lakes is presented in Figure 16, following Adams and Lasenby (1985). In Figure 16a, a quasi-infinite water layer is considered to be covered by a layer of smooth congelation (black) ice, in turn covered by snow. This is a crude simplification of the properties of natural lakes; an important aspect considering the simulation of emission properties are, for example, slushing events, which cause water to surge above the ice level as the combined weight of accumulated snow and ice overcomes the buoyancy of the ice (Figure 16b). Refreezing of the water after these events results in the formation of a snow-ice (or: white ice) layer between the black ice and snow cover. The layer of white ice differs from congelation ice in terms of density and structure (Adams and Lasenby, 1978); thus, also the dielectric and scattering properties of white ice differ from those of congelation ice. The slushing events themselves drastically change the observed emission signature from the lake before the formation (refreezing) of the white ice layer.

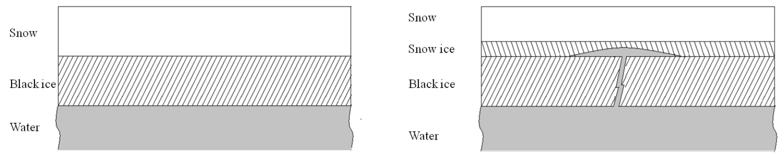

(a) (b)

Figure 16: Schematics of the structure of snow-covered lake ice (following Adams and Lasenby, 1985). Snow cover on top of newly formed congelation (black) ice (a). Slushing of water through cracks in congelation ice layer, and formation of snow ice (b). *Lemmetyinen et al. (2011) [P4]*. © 2011 IEEE.

6.3.1. Simulations against airborne observations

Experimental data collected in April 2008 over several lakes close to the Mackenzie River delta in the Canadian Northwest Territories provided the opportunity to assess the capability of the multiple layer extension of the HUT model for simulation of microwave emission from frozen lakes (Gunn *et al.*, 2011 [P3]). Airborne radiometer data at 6.9, 19, 37 and 89 GHz together with *in situ* measurements of ice and snow on ice properties were gathered from a total of 25 sites. The sites were situated over both freshwater and brackish (saline) lakes; ten of the sites were at locations where backflow from the ocean introduces saline water in the lakes. The type of the lake was seen to have a clear influence on the measured brightness temperature at low frequencies (6.9 and 19 GHz). In the following, simulation results over the freshwater lakes are analyzed as these were of relevance regarding later phases of the study.

A summary of simulation results for the freshwater lake ice sites is shown in Figure 17. For the lowest frequency examined (6.9 GHz in Figure 17a), it is notable that the model was unable to produce the full range of observed brightness temperatures; model simulations from all sites vary within 5 K for both polarizations, while observed values ranged from 160 to 220 K and 156 to 194 K for vertical and horizontal polarization, respectively. This indicates variability in the ice or water conditions between the lake ice sites, which is not reflected by the available *in situ* information. The high penetration depth at 6.9 GHz in dry snow would suggest that the snow layer is not the origin of the observed variability.

For simulations at 19 GHz (Figure 17b), the range of brightness temperature variations is well represented, although model simulations show a slight overestimation (7.1 and 8.4 K bias error for all sites for vertical and horizontal polarizations, respectively). In contrast, the 37 GHz simulations in Figure 17c, most affected by snow conditions over the lakes, show an underestimation for almost all sites with a mean bias error of about -9 K for both polarizations. Considering the channel difference typically used for retrieval of snow water equivalent (19 - 37 GHz) this causes a strong positive bias as depicted in Figure 17d. Error statistics of the simulations are given in Table 6 in section 6.3.3.

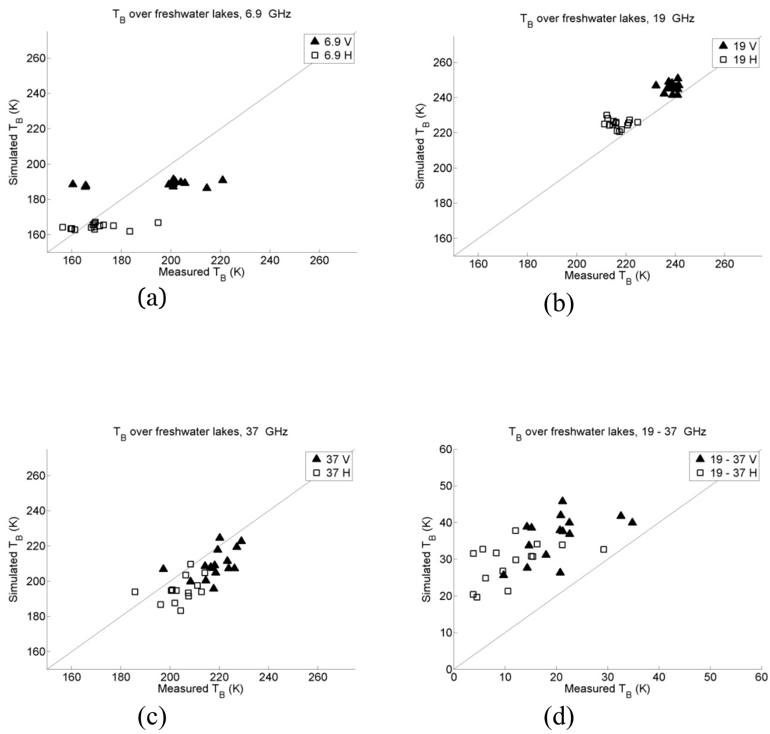

Figure 17: Agreement of simulated brightness temperatures relative to airborne measurements over fresh water lakes in Canada (data from [P3], Gunn *et al.*, 2011).

The simulation experiments in [P3] also examined the effect of several empirical parameterizations of the HUT model on accuracy of lake ice simulations. Regarding the simulations of emission from the ice and water layers, the parameter examined was the roughness of the ice/water interface in simulations (see eq. (5.11)). This parameter was not measured in the field and was thus considered as an empirical correction parameter to the model. A similar roughness consideration could have been chosen, for example, for the ice/snow interface. However, as information on its physical roughness was equally unavailable, the ice/water interface with a large dielectric contrast was chosen. As can be expected, the parameterization for ice roughness most affects the lower two frequencies examined, as on the higher frequencies the modeled penetration depth into snow and ice is insufficient to be significantly affected by the reflection coefficient of the lowest interface between ice and water. In [P3], introducing a roughness element to the simulations (and thus effectively reducing the reflection coefficient) was found to reduce the error of estimates compared to simulations with a completely specular surface. The parameterization was of importance regarding later studies; a similar empirical correction was used in the satellite scale simulations and retrieval in [P4], as it was again noted that for a specular reflection consideration, the simulations produced a persistent underestimation compared to measured emissions, in particular on lower frequencies.

6.3.2. Satellite scale simulations

[P4] presents a forward modelling experiment examining the influence of lakes at the spatial scale of satellite observations. Simulations were made and compared to observations considering two scenarios: first, the influence of lakes was (1) excluded and (2) then included in the forward model of the satellite scene. In the first case, the lakes were modelled simply in the same way as non-vegetated dry ground. In the latter case, lakes were modelled following the method used in [P3] for point-scale simulations (however, taking into account also the influence of atmosphere). Input data to the forward modelling experiments were acquired from snow course observations, as well as measurements of ice thickness and the depth of snow on ice. The available spatially distributed measurements were kriging interpolated to cover the whole study area (see Isaaks and Srivastava, 1989). The simulation results obtained were then compared to reference observations.

This study applied EASE (Equal Area Scalable Earth) -gridded brightness temperature observations (Knowles *et al.*, 2006) from AMSR-E/Aqua as a reference to model simulations. EASE grid cells with significant lake cover (>30%) from Finland were chosen to study the effect of lakes on simulation accuracy. Most of the selected grid cells were situated in the lake district of central Finland (between latitudes 61 and 64°), and several over large lakes in northern parts of the country. Lake coverage was determined simply from land cover information over the nominal spatial extent of each cell. Kriging interpolated maps of snow depth, snow depth on ice and ice thickness, derived from *in situ* information, were used as the primary simulation input. The interpolated maps were calculated from a dataset of daily automated weather station observations of snow depth and air temperature, as well as periodic manual *in situ* observations of lake ice thickness and the depth of snow on lake ice. Several *a priori* model parameters (e.g. snow density, grain size, snow and ground temperature) were set as constant values; as with simulation comparisons to airborne observations in [P3], an empirical correction to the reflection coefficient of the ice/water interface was used (see eq. (5.11)).

Figure 18 presents the results of the forward modelling experiment at the frequency combinations relevant for retrieval of SWE (the channel differences 18.7 – 36.5 GHz (V -pol) and 18.7 V – 18.7 H, as used by Pulliainen and Hallikainen, 2001). The figure demonstrates how, in this case, the inclusion of the effect of lakes improves overall simulation results of both channel differences. Notably, the 18.7 – 36.5 GHz channel difference is significantly overestimated when lake simulations are omitted. This is mainly due to the overestimation of the 18.7 GHz channel component. The inclusion of lakes in the simulation on average reduces the simulated 18.7 GHz channel brightness temperature, thus reducing also the channel difference. The change in the 36.5 GHz channel varies, depending mainly on estimated snow conditions over lakes.

The bias in the 18.7 V – 18.7 H polarization difference similarly is reduced when lakes are included in the simulations; for lakes, the model considers the contrast of polarizations to be greater than over land; thus the inclusion of lakes raises the average polarization difference of a given grid cell. However, the dynamic range of the observed polarization differences is not captured by the model. Thus it can be assumed that either 1) the model is not sensitive enough to reported changes in ice and snow properties or 2) a key parameter affecting the polarization ratio is missing from the *in situ* information.

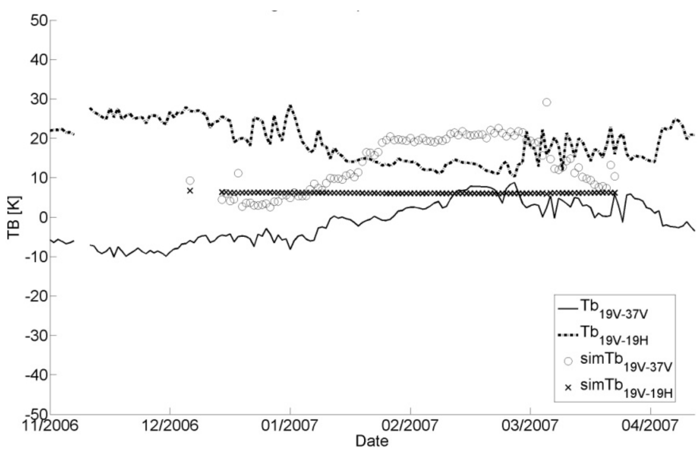

(a)

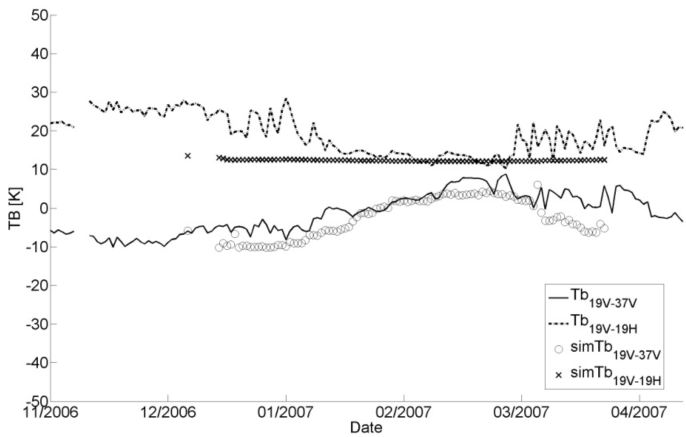

(b)

Figure 18: AMSR-E observations and simulated brightness temperature over lake-rich areas (lake fraction over 30 %) in Finland during winter season 2006-2007. Average of five EASE grid cells presented. Results shown for the channel differences 18.7 – 36.5 GHz (V -pol) and 18.7 V – 18.7 H applied in retrieval. Effect of lakes omitted in simulation (a), and included (b). *Lemmetyinen et al. (2011) [P4]*. © 2011 IEEE.

6.3.3. Synthesis: simulation of microwave emission from frozen lakes

Results for both the simulations of the airborne dataset in [P3] and the satellite scale simulations in [P4] are summarized in Table 6. The airborne results represent simulations made for freshwater lakes (the dataset in [P3] included measurements also over brackish lakes); the satellite scale results represent one winter period (2006-2007, as in Figure 18).

Considering simulation errors of individual channels, the airborne data indicate bias errors below 10 K and (bias corrected) RMS errors of less than 12 K for the investigated frequency range (with the exception of 19 K RMSE for the horizontally polarized 6.9 GHz channel). Satellite scale simulations accounting for lake cover provide even lower error values, being nevertheless of the same magnitude. In terms of modeling bias, the inclusion of lakes in the satellite scale generally reduces simulation errors compared to the case where lakes were simulated similarly to open terrain (with the exception of the horizontally polarized 37 GHz channel). In terms of RMSE errors, simulation results of all channels are improved. The studies in [P3] and [P4] clearly indicated that even the relatively simple forward modeling approach for lakes can be used to simulate the brightness temperature signatures of frozen lakes over a broad frequency range, and thus reduce simulation errors on a large scale, when lakes account only for a part of the modeled scene.

TABLE 6: BIAS, RMS AND UNBIASED RMS ERRORS[9] OF SIMULATION ESTIMATES OF BRIGHTNESS TEMPERATURE AGAINST AIRBORNE AND AMSR-E OBSERVATIONS FOR GRID CELLS WITH LAKE FRACTION OVER 30%, INCLUDING COMPARISON OF SIMULATION ERRORS WHEN OMITTING AND INCLUDING EFFECT OF LAKES.

	Agreement of simulations relative to airborne observations [P3]								
	Channel	6.9V	6.9H	19V	19H	37V	37H	19V – 37V	19V - 19H
	Bias [K]	-5.1	-5.4	7.1	8.4	-8.8	-9.3	15.9	-1.2
	RMSE [K]	18.9	10.5	7.9	9.7	12.0	11.9	17.0	4.3
	uRMSE [K]	18.2	9.1	3.4	4.8	8.1	7.4	6.0	4.1
	Agreement of simulations relative to AMSR-E observations [P4]								
	Channel	10V	10H	19V	19H	37V	37H	19V – 37V	19V - 19H
lakes omitted	Bias [K]	10.9	18.9	6.7	15.5	-3.9	3.8	10.6	-8.8
	RMSE [K]	15.3	22.9	12.7	20.7	11.8	13.7	12.3	10.4
	uRMSE [K]	10.7	13	10.8	13.7	11.2	13.2	6.1	5.6
lakes included	Bias [K]	-8.4	-5.9	1.6	5.3	2.6	6.3	-1	-3.7
	RMSE [K]	12.9	11.1	9.7	12.2	10.2	13.5	3.5	5.5
	uRMSE [K]	9.8	9.3	9.5	11	9.8	11.9	3.4	4.1

However, it can be questioned whether the simplified model can accurately capture the varying emission signatures on lakes at the lower frequencies; this is clearly not the case for 6.9 GHz observations, which show a far larger variability than is captured by the simulations. Similar findings have been made also by e.g. Kontu *et al.* (2008). Also, at the satellite scale, either the model or the available *in situ* information was insufficient to account for the variability in observed brightness temperatures at the lower AMSR-E frequencies. At 19 GHz, simulation results were very sensitive to the empirical parameterization of the ice/water interface reflection coefficient, whereas at 37 GHz, the effect of ice properties on simulation results is of secondary importance compared to snow cover parameters. In this regard, it can be said that the model accurately reflects the observations, as little or no correlation with ice conditions and e.g. the underlying water type (freshwater or brackish water) can be found, for example, in the airborne observational data at 37 GHz in [P3]. A correlation with fractional lake cover at 37 GHz is reported in [P4], but this can be attributed to the aforementioned snow conditions (which, over lakes are typically different from those over dry terrain).

9 $\text{uRMSE} = \sqrt{\frac{\sum_{i=1}^{n}(f(x_i)-x_i-bias)^2}{n}}$

6.4. Monitoring of soil freeze/thaw processes

Areas affected by soil freezing cover more than 50 % of the total landmass of the Earth. This includes both areas with perennial and seasonal soil freezing, with permafrost areas covering approximately 24 % of the landmass (Smith and Brown, 2009). Seasonal freeze thaw cycles have a crucial impact on the energy and moisture balance of soils as well as transpiration of atmospheric gases. Soil freezing affects both the latent heat exchange and surface radiation balance, as well as hydrological factors such as hydraulic conductivity and infiltration of moisture. Information on soil freezing thus affects, for example, the precision of surface runoff estimates (e.g. Willis *et al.*, 1961). A notable effect of soil freezing and thawing is on the exchange of different atmospheric gases such as CO_2 and methane (Skogland *et al.*, 1988; Zhang, 2003).

The applicability of L-band microwave radiometry for monitoring the freeze/thaw properties of soil is studied in [P5]. An extensive dataset of co-incident radiometer observations and *in situ* information on soil and snow properties are applied, as well as airborne observations and the first data collected by the SMOS satellite (see section 8.1). The objective of the study was to assess the potential of L-band in the monitoring of soil-freeze thaw processes, analyzing different factors affecting the microwave signature during the winter season. Finally, the overall aim is to extend the findings to observations with SMOS. Microwave radiometry has previously been applied to observe the soil freeze/thaw states from space (e.g. Zhang *et al.*, 2001), but L-band has the added advantage of increased penetration depth and low sensitivity to dry snow cover.

In [P5], several features from the seasonal behavior of the microwave signal are indentified and discussed. The study also introduces a simple emission model for estimating the effect of progress of soil freezing on microwave emission at L-band. The model formulation is analogous to the one presented in [P2]. Model estimates, derived using the *in situ* information collected from the site, are compared to radiometer observations. The goal of the modeling efforts was to provide an explanation for the detected signal behavior during soil freezing, in particular the dynamic range of the signal from frozen and thawed soil.

6.4.1. Experimental data at L-band

[P5] presents an experimental dataset collected using the L-band Elbara-II radiometer, developed as a reference radiometer for SMOS (Schwank *et al.*, 2010). The instrument was installed on a 5-m tower at a fixed location at the Finnish Meteorological Institute Arctic Research Centre in Sodankylä, Finland (Figure 19). The instrument was set to measure a range of incidence angles (30-70°) at regular intervals of 3 hours, and at a constant incidence angle of 50° between these elevation scans. The instrument was calibrated internally using a reference load at ambient temperature and an Active Cold Load (ACL) unit. The ACL noise temperature (30-50 K), in turn, was calibrated at regular intervals using a cold sky calibration. Instrument stability was monitored with regular observations of the cold sky (every 12 hours).

Figure 19: The Elbara-II radiometer (large conical horn) installed at the FMI Arctic Research Centre. Photo: K. Rautiainen, 2011.

The radiometer observations were supported by extensive observations of soil, snow and atmospheric properties. Automated sensors were used to obtain the soil temperature and moisture profiles, which also serve as an indicator of soil freezing. These were complemented by regular manual measurements of the soil frost depth. Figure 20 presents a time series of brightness temperatures for horizontal and vertical polarizations (a) against measured snow depth and the depth of soil frost (b) during the winter season of 2009-2010. Several seasonal features were identified in [P5]; these included

- Rapid increase and saturation of L-band signal during autumn soil freezing
- Stable signal level for vertical polarization during the cold winter period; slight variability in horizontally polarized signal
- Rapid diurnal changes with spring melt/refreeze cycles of snow cover

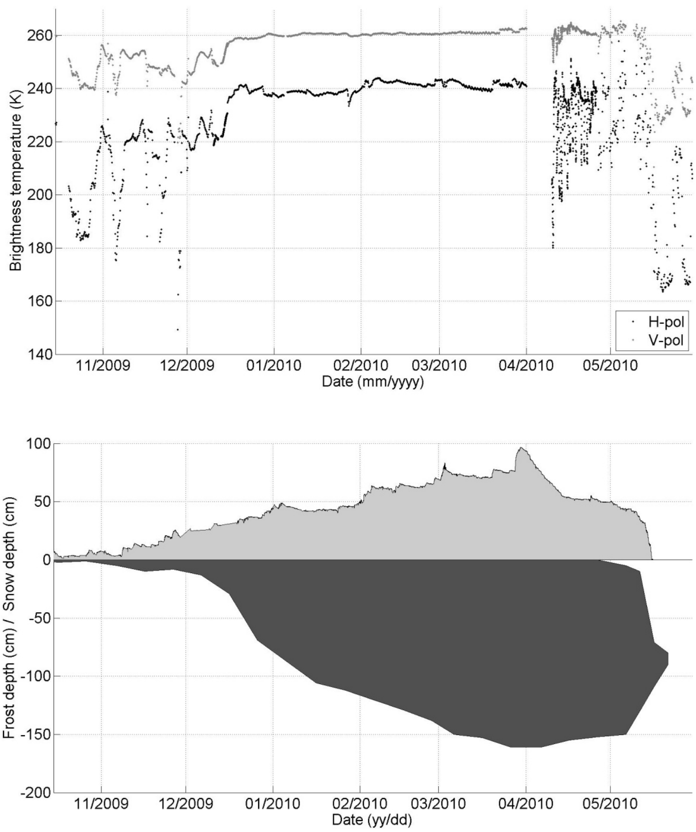

Figure 20: Time series measured brightness temperature from Elbara-II radiometer at H- and V polarizations, 50° incidence angle (a) against observed snow depth and soil frost depth (b). *Rautiainen et al. (2011) [P5]*. © 2011 IEEE.

Of the identified seasonal features in the L-band signal, the strong change in emission signature with autumn soil freezing was seen as having potential also considering coarse-scale satellite observations (i.e. SMOS). It was anticipated, however, that for differing land cover and soil types, the detected range of the change in emission signature would vary. In order to be able to anticipate the possible influence of soil types on the dynamic range of the signal, a simple emission model was formulated. Also, data from an airborne campaign over the study region were used to directly analyse the influence of land cover on the L-band signatures during the freezing period. These results are discussed in the next sections.

6.4.2. Simulation of soil freezing effects at L-band

In [P5], the detected changes L-band brightness temperature during freeze/thaw processes were considered mainly to originate from (a) changes in the dielectric constant of the frozen soil layer, (b) changes in the dielectric constant of unfrozen soil below the frozen soil layer and (c) changes in the snow layer conditions above the ground

An emission model to simulate the effect of soil freezing on emitted brightness temperature was formulated following these considerations. A simplified planar structure to describe the soil freezing process was adopted – the soil was considered to include a discrete layer of frozen soil of varying thickness, covering a quasi-infinite layer of thawed soil (Figure 21).

In the model, the frozen layer was characterized in terms of layer thickness, roughness of the top surface and permittivity. The unfrozen soil beneath was characterized in terms of permittivity and roughness of the interface of frozen and thawed soil. In [P5], an empirical model was applied to calculate the soil permittivity for the thawed portion of the soil following Dobson *et al.* (1985), using *in situ* data on soil moisture and temperature as model inputs. The permittivity of frozen soil was derived by fitting the soil emission model to peak winter season observations. During the cold winter period, the soil was considered frozen beyond the penetration depth of the radiometer (~10 cm) and the model fitting could be performed by considering the entire soil layer to be frozen with a uniform permittivity. Vertically polarized observations were used, due to their smaller sensitivity to layering effects in the snow. The derived dielectric constant varied from $3.3 - j \cdot 0.8$ to $3.8 - j \cdot 0.95$, with an average value of $3.6 - j0.9$.

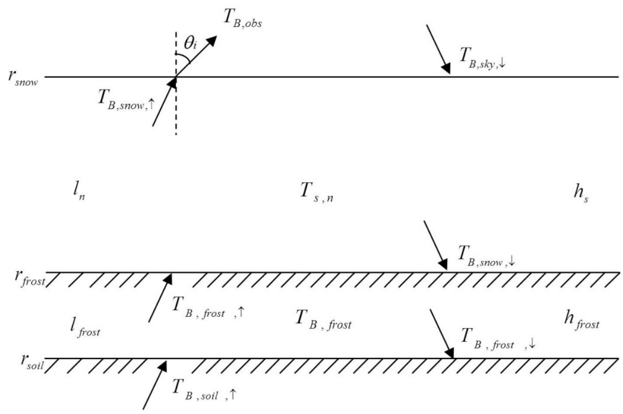

Figure 21: Schematic of applied soil emissivity model. Each layer (snow, frozen soil, thawed soil) is characterized by the reflection coefficient $\boldsymbol{r}_{[\mathbf{medium}]}$, loss factor $\boldsymbol{l}_{[\mathbf{medium}]}$, temperature $\boldsymbol{T}_{\mathbf{0},[\mathbf{medium}]}$ and thickness $\boldsymbol{d}_{[\mathbf{medium}]}$. The resulting up- and downwelling brightness temperatures $\boldsymbol{T}_{\mathbf{B},[\mathbf{medium}],\uparrow}$ and $\boldsymbol{T}_{\mathbf{B},[\mathbf{medium}],\downarrow}$ are applied to solve the observed brightness temperature $\boldsymbol{T}_{\mathbf{B,obs}}$. The model is analogous to the multiple layer adaptation of the HUT snow emission model, presented in section 5.2. *Rautiainen et al. (2011) [P5].* © 2011 IEEE.

Figure 22 presents modelled behaviour against observed brightness temperatures with increase in frost depth. There is a clear analogy between measured values and model estimates. The incoherent two-layer model explains the increasing brightness temperature as a function of soil frost and the saturation of the measured signal. Compared to observations, the model estimates the saturated brightness temperature value well, with brightness temperatures around 240 K and 260 K for H- and V-polarization, respectively. In addition, the simulated dynamic range of brightness temperatures is reasonable, being 15 K (for H-pol.) and 10 K (for V-pol.). However, the modelled brightness temperatures reach their saturation values already with a frost depth of ca. 10 cm, arising from the penetration depth at L-band for frozen ground, whereas the observations would seem to indicate that the saturation occurs only after a frost depth of 30 cm is reached.

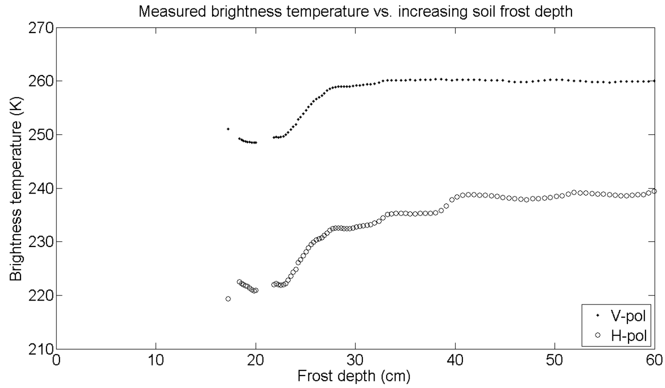

(a)

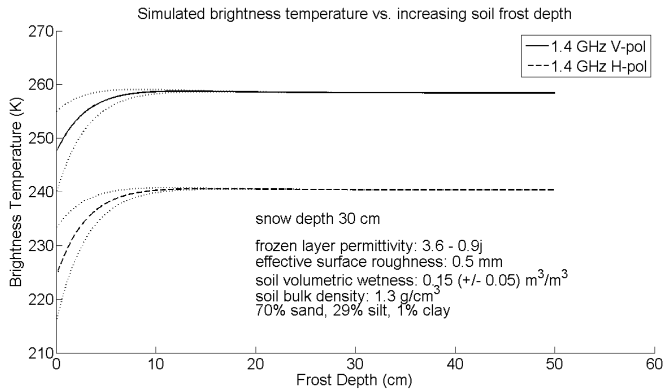

(b)

Figure 22: Measured ELBARA-II brightness temperature as a function of soil frost depth obtained from manual measurements during the rapid freezing period in early winter 2009 (a). Model prediction using in-situ data as input (b). *Rautiainen et al. (2011) [P5].* © 2011 IEEE.

It is acknowledged in [P5] that the emission model applied is a simplification of the freezing process, as the simulation does not account for a transition (tapering) zone. Residual unbound water within the frozen soil (supported by *in situ* observations) results in a transition zone with a mixture of soil in frozen and thawed state (Schwank *et al.*, 2004). Furthermore, radiative transfer within the frozen portion of the soil is considered through absorption only (no volume scattering effects are considered), which is nevertheless a reasonable approximation at L-band frequencies. A further simplification is the omission of an organic layer in the simulation: the frozen portion of soil is considered homogeneous in terms of soil structure and density, thus again decreasing the accuracy of the permittivity calculation.

In addition, the model omits coherent effects possibly arising for layers which are thin compared to the wavelength. Regarding the goals of the study in [P5], this was considered to be a sufficient approximation. Furthermore, it may be difficult to predict the total influence of coherent effects even with a suitable model, as these are also influenced by non-idealities in the layer interfaces (roughness and height variations), which may be significant especially as the observation footprint increases. Indications of such effects have been reported in localized measurements of freezing soils by Schwank *et al.* (2004). However, in that study the penetration of soil frost was less prominent than in the case of the Sodankylä test site.

6.4.3. Considerations of applicability to coarse-scale (SMOS) observations

The study in [P5] implies the usability of L-band in the detection of the onset of soil freezing, and potentially also for the indirect monitoring of soil frost depth. In the experimental dataset, also a clear indication of snow melt-off is seen. However, the soil thawing processes are largely masked out by the effect of melting snow. Considering the applicability of L-band to soil freeze/thaw monitoring on a satellite scale, the coarse spatial resolution of the observations again pose particular problems. The experimental dataset in [P5] was collected over relatively dry mineral soil. As the satellite footprint on the scale of SMOS (~50 km) will include several land cover types, the behavior of the L-band signature should be verified also over these. In particular, lakes and wetlands such as bogs may cause a problem in this respect as the resulting change in emission during freezing may not follow that of dry soil in same area; therefore, the fractional amount of lakes and wetlands in a satellite scene will influence the overall dynamics of the signal, an important aspect considering typical simple change detection algorithms (as the one proposed by Zhang *et al.*, 2001). Also, the freezing process may advance temporally at a differing pace over wetlands and dry soil. The differing spectral response to freezing is confirmed by airborne measurements conducted using the interferometric HUT2D radiometer (Rautiainen *et al.*, 2008) during two flight campaigns over the Sodankylä test site. Figure 23 illustrates the 1st Stokes parameter[10] calculated over several incidence angles over the dominant land cover types of the test area. The measurements were made on Oct 1st and Oct 12th 2009; during the first

[10] $(T_H + T_V)/2$

flight, the top soil of the ground was partially frozen up to a depth of several centimeters, however with patches of thawed soil present. Lakes and bogs were in an unfrozen state. During the second flight, soil freezing was more uniform (albeit the frost depth had not advanced beyond 5 cm) and a shallow snow cover was present. A partial thin ice cover was present over lakes and open bogs. Over the three land cover categories, the detected brightness temperature is increased due to the onset of cold temperatures and subsequent freezing of soil and water surfaces. However, the detected change in terms of absolute brightness temperature is most prominent over lakes (30 K), and the smallest effect is seen over forested dry land (8 K), with bogs exhibiting a level of change between these (22 K). In order to define a change detection algorithm for satellite scale observations, the differing response of land cover should be taken into account; else, the large difference e.g. in the microwave emission of open and frozen lakes and other water bodies is likely to cause an overestimation of the soil freezing process in areas with significant lake cover.

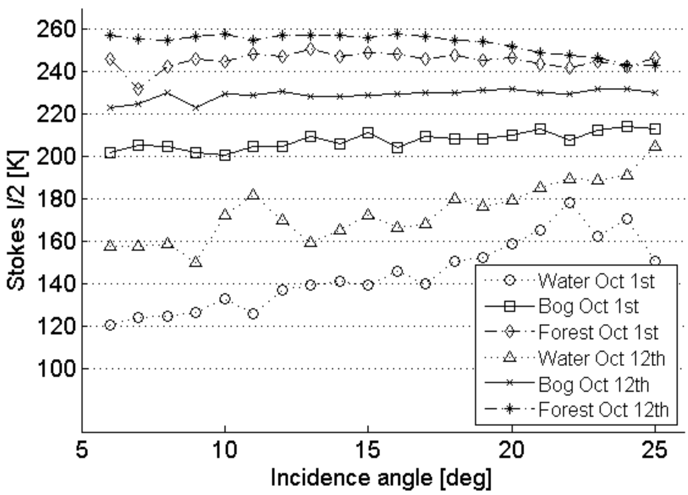

Figure 23. The measured 1st Stokes parameter (divided by 2) for the three main soil types and land cover within the test lines. The results have been averaged for incidence angles from 6 to 25^o (± 0.5°). Standard deviation varied from 20 K to 35 K. *Rautiainen et al. (2011) [P5]*. © 2011 IEEE.

7. Retrieval of snow water equivalent over lake-rich areas

Areas with significant lake cover present a problematic environment for the application of passive microwave instruments for detection of snow cover parameters. The penetration depth of microwaves at wavelengths typically applied for snow cover detection is sufficient for a significant amount of detected emission to originate from beneath the snow cover. Due to the dielectric contrast compared to dry ground, the differing emissivity of lakes and other water surfaces confound the interpretation of the observed emission over heterogeneous scenes. This applies both to inversion algorithms based on linear regression (e.g. Chang *et al.*, 1987, Kelly *et al.*, 2003) and to methods based on inversion of a forward emission model (e.g. Pulliainen and Hallikainen, 2001).

The study in [P4] presents a novel retrieval scheme of snow water equivalent based on inversion of the HUT snow emission model. The general retrieval methodology follows the one introduced by Pulliainen and Hallikainen (2001); however, the forward emission model is updated to include simulation of snow-covered lake ice. The layered emission model, presented in [P2], is adaptable for this purpose. The forward modelling concept for lakes and validation results using the model were presented in section 6.3. The study applies the model in the retrieval scheme, aiming to improve retrieval accuracy of snow water equivalent over lake-rich areas. Ancillary data were used to define some model input parameters, including, for example, the thickness of ice on lakes.

7.1. Revised retrieval method

The retrieval experiment in [P4] follows the statistical model inversion method described in section 5.3, and applied previously in conjunction with the HUT snow emission model by Pulliainen and Hallikainen (2001). However, a revised forward model is applied, in an attempt to compensate for the effect of lakes in the satellite scene. As for the forward modeling experiment, distinctive land cover types μ are accounted for in the simulations so that $f_i(\mathbf{x})$ is a sum of the fractional components of the different land cover types, with the result

$$f_i(\mathbf{x}) = f_i^{tot}(W, d_0) = \sum_{\mu=1}^{M} \beta_\mu f_i\left(W_\mu, d_{0,\mu}\right), \tag{7.1}$$

where W_μ is the snow water equivalent, $d_{0,\mu}$ the reference grain size and β_μ the fractional coverage of land cover type μ. Note that W_μ and $d_{0,\mu}$ can be set to be respective of their land cover types, or assigned as common values. The cost function (see (5.14)) then takes the form

$$\begin{aligned} W_t &= \min_{W,d_0}\left\{\sum_{i=1}^{N}\frac{[y_i - f_i(\mathbf{x})]^2}{\mathrm{var}(\varepsilon_i)} + \frac{d_{0,ref} - d_0}{\mathrm{var}\left(d_{0,ref}\right)}\right\} \\ &= \min_{W,d_0}\left\{\sum_{i=1}^{N}\frac{[y_i - f_i(W_t, d_0)]^2}{\mathrm{var}\left(\varepsilon_{i,t}\right)} + \frac{d_{0,ref} - d_0}{\lambda_{d_{0,ref}}^2}\right\}, \end{aligned} \tag{7.2}$$

where y_i is the observed brightness temperature of channels i, and $f_i(\mathbf{x})$ is the modeled response of the same channels as a function of parameters $\mathbf{x}$. The parameters in $\mathbf{x}$ are W_t (snow water equivalent) and d_0 (grain size). $\varepsilon_{i,t}$ is the sum of model and observation errors, and $\lambda_{d_{0,ref}}^2$ the estimated variance of the reference grain size value.

7.2. Results of SWE retrieval

In [P4], the geographic area of Finland was chosen as a test area for assessing the applicability of the revised retrieval scheme, which takes account of the relatively large amount of lakes, and the ready availability of *in situ* information on snow and lake ice properties. The SWE retrievals were conducted using daily AMSR-E observations of the test area (Knowles *et al.*, 2006) for three winter periods (2005-2006, 2006-2007, 2008-2009). Ancillary data on vegetation properties as well as measured properties of lakes (ice depth) were applied.

7.2.1. A priori settings

The retrieval scheme requires *a priori* information on, for example, snow density, as well as ground, snow and air temperatures. These were derived partly based in available *in situ* data as for the forward model experiment, and partly by using approximated, best-guess values. The kriging interpolated fields of ice thickness were the same as were used in forward modeling (section 6.3.2). Naturally, the snow depth data were not used as this was the object of the inversion process. However, in the iterative inversion, a fixed ratio between snow over land and over lakes was assigned. Based on available *in situ* data, the snow water equivalent over lakes was always considered to be half of that over land. The large difference in SWE is explained by the relatively dense vegetation over land surfaces, which reduces wind effects. For open regions such as tundra, the differences of SWE between snow on lakes compared to dry terrain may be less prominent – for example, Derksen *et al.* (2009) have reported values of 119 mm SWE over land versus 100 mm over lakes in Canadian tundra regions. In the inversion tests the model and observation errors $\varepsilon_{i,t}$ were estimated to be 1 K, and the variance of the effective grain size $\lambda^2_{d_{0,ref}}$ 0.1 mm. The reference effective grain size $d_{0,ref}$ was set to be 1 mm, following a parameter fit performed in the forward modeling experiment. The variance of the reference grain size was in this case a purely arbitrary value; in practice, the set value of 0.1 mm allows the value of the grain size to fluctuate slightly when performing the retrieval. The remaining fixed *a priori* parameters are summarized in Table 7.

TABLE 7: FIXED VALUES USED IN THE SIMULATIONS FOR ALL THE TARGET AREAS. VEGETATION DATA FROM NATIONAL LAND COVER INFORMATION.

Parameter	Value
Grain size	1.0 mm
Snow density on land	0.2 g/cm^3
Snow density on lakes	0.2 g/cm^3
Ice density	0.916 g/cm^3
Snow moisture	0 %
Temperature of ice	-5 °C
Temperature of water	0 °C
Temperature of ground	-5 °C
Temperature of vegetation	-5 °C
Vegetation volume (from	0…142 m^3/ha
Permittivity of frozen soil	6-1j
Rms height variation of	3 mm
Rms height variation of	1 mm
Water salinity (lakes)	0 psu
Ice salinity (lakes)	0 psu

Figure 24 shows an example of SWE estimates obtained over Finland in the two test cases for a single date (Jan 1st, 2006). In Figure 24a, the estimate is performed without accounting for lakes in the forward model simulation, whereas in Figure 24b the influence is included. The depicted SWE value corresponds to the value estimated over dry land (thus not as an average value of SWE over land and lakes). The difference between the two retrievals is portrayed in Figure 24c. A qualitative visual examination of the depicted data would indicate that the presence of large lakes has influenced the retrieval result in Figure 24a, with very low SWE values obtained over areas with significant lake coverage; the largest apparent differences Figure 24c are evident in the lake districts over southern and central Finland as well as over several larger lakes in the north.

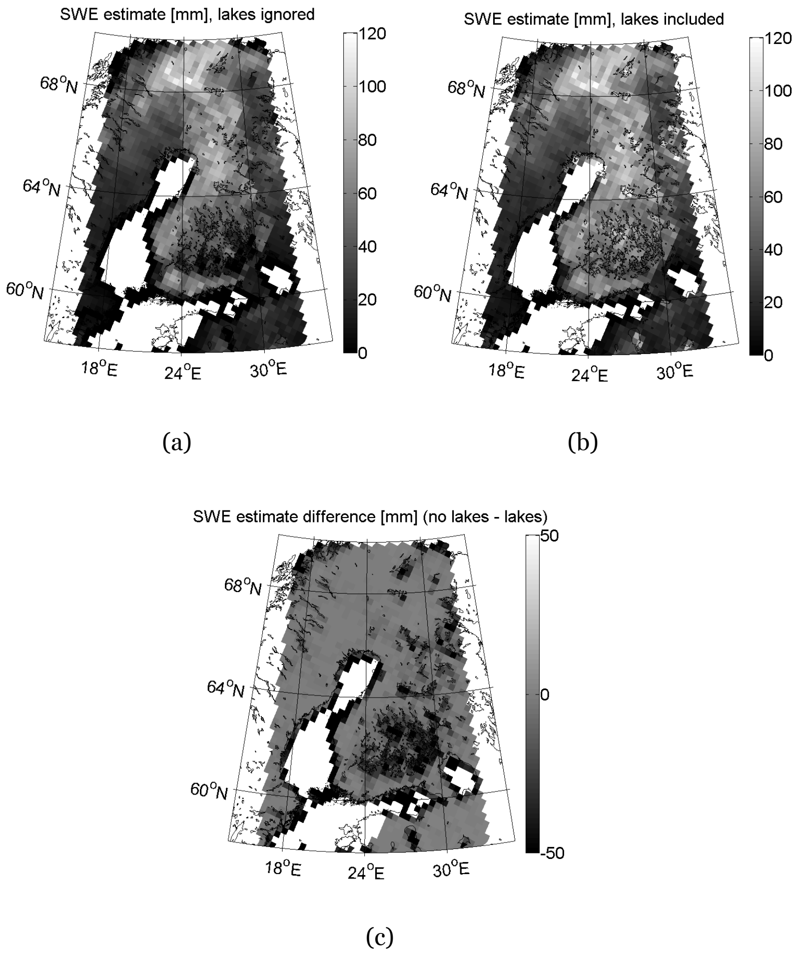

Figure 24. Gridded maps of SWE estimates [mm] for January 1st, 2006, by (a) ignoring lakes in simulations and (b) applying lake simulations in the retrieval algorithm. Difference between estimates in (a) and (b) is depicted in (c). *Lemmetyinen et al. (2011) [P4].*

7.2.2. Validation of revised retrieval scheme

In order to determine whether the retrieval results were improved in the experiment, the retrieved SWE for the three test years was compared to manually measured snow course observations on snow depth and water equivalent. Histograms depicted in Figure 25 show the detected overall improvement of derived SWE estimates, when comparing these to ground measurements in the two test cases. Positive values indicate improvement, while negative values indicate cases where the accuracy of estimates has deteriorated. Figure 25 separates the estimated grid cells into three categories according to their lake cover fraction; those with a lake cover fraction of 5 to 15 %, 15 to 30 % and over 30 %. On average, the retrieval result was improved in all categories, but the improvement was most prominent in the category with the lowest lake cover fraction both in terms of cases of improvement and the average improvement of the bias error in mm. In terms of numbers of cases improved, the least improvement was found in the category with the largest fractional lake cover. This may indicate either the insufficiency of the available *in situ* data driving the forward model, or failings in the modeling approach for lakes. Firstly, the point-wise data used to initialize the lake ice thickness may not be representative over large areas. Secondly, the assumption taken of lakes having half of the water equivalent compared to dry land areas may not be valid beyond the available scarce *in situ* information from the region. Furthermore, complex structures in the lake ice system, such as the presence of a white ice layer and water between the ice and snow layers, complicate the microwave emission especially for larger lakes, which the relatively simple modeling approach is not able to capture.

Regardless of the above shortcomings, the retrieval of water equivalent was seen to improve with the upgraded forward modeling approach. In principle, the approach could be expanded to cover other types of heterogeneous sceneries and naturally layered structures, such as coastlines (sea ice) and other wetland areas, which pose similar problems to coarse scale passive microwave retrieval as do freshwater lakes. The formulation of a forward emission model, and *a priori* initialization of the model inputs, however, may prove to be considerably more challenging than in the case of lake ice.

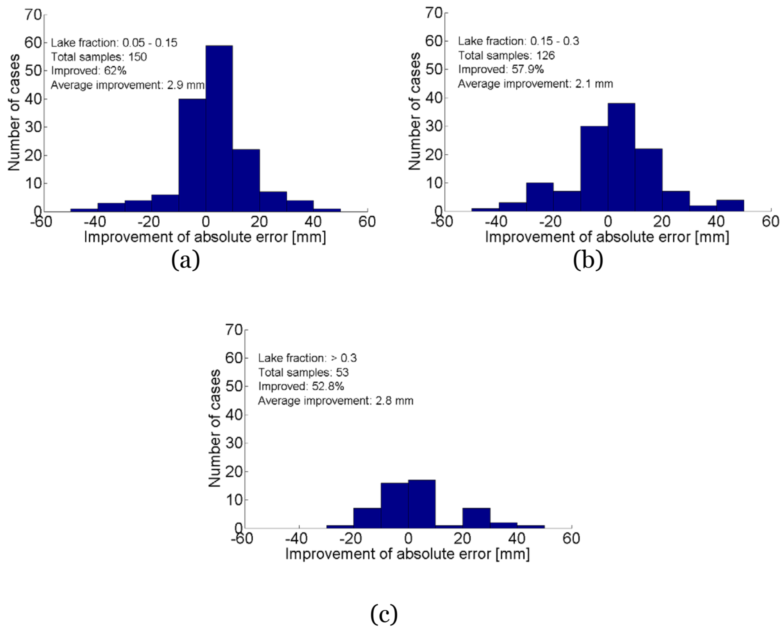

Figure 25. Histograms of the improvement of the SWE estimate in individual grid cells with lake fraction of 5 to 15 % (a), 15 to 30 % (b) and over 30 % (c) for three winter periods (2005 – 2008). Positive value indicates improvement (reduction) of error. *Lemmetyinen et al. (2011) [P4].*

7.3. Considerations for practical applications

The successful use of an emission model to account for lake effects in a practical retrieval scheme requires initialization of the status of lake freezing (freezing date, ice thickness, ice type); the application of *in situ* data in this respect is not practical for global retrieval approaches, as such data are rarely available. Therefore, applying the presented method would require, for example, coupling of the emission model with a thermodynamic model that would give *a priori* information on the lake ice state where required. Lake ice models (e.g. Duguay *et al.*, 2003) have been shown to predict ice growth in freshwater lakes to a good accuracy when adequate forcing data is available (through direct measurements or e.g. atmospheric reanalysis).

In situ data (e.g. Derksen *et al.*, 2008) shows significant differences between snow conditions over lakes compared to land surfaces. The difference is due to wind effects affecting snow distribution, which are more prominent over level ice than even relatively open terrain such as tundra. In order to improve the accuracy of the model inversion, *a priori* knowledge of the relation of snow conditions (in terms of typical snow depth, density and grain size relations) between snow on lakes and snow on dry terrain is needed, as these cannot be separated implicitly from the observations.

One possibility in this respect is the application of high resolution SAR (Rott *et al.*, 2009) for deriving lake ice properties, including lake freeze up, and possibly ice thickness and snow depth on ice. However, for hemispherical applications this would require a large amount of SAR data, which is currently not operationally available at the temporal resolution needed.

8. SMOS calibration subsystem

The SMOS (Soil Moisture and Ocean Salinity) satellite mission of the European Space Agency, successfully launched in 2009, is the first satellite mission deploying an aperture interferometric aperture synthesis radiometer in space. The method had been applied previously in the field of radio astronomy; applying interferometry for remote sensing of the Earth was originally proposed by Ruf *et al.* (1988). The single payload of SMOS, the MIRAS (Microwave Imaging Radiometer Using Aperture Synthesis) instrument, is an L-band aperture synthesis radiometer. As indicated by the name of the mission, the MIRAS specifications and the SMOS measurement configuration are optimized for the detection of sea surface salinity and soil moisture variations from space. Applying the L-band for measuring ocean salinity was originally proposed by Swift *et al.* (1983). In addition, the mission is expected to contribute to cryosphere studies, including detection of shallow sea ice thickness (Kaleschke *et al.*, 2012) and soil freezing and thawing (Rautiainen *et al.*, 2011, [P5]).

Interferometric radiometry presents particular challenges also for instrument calibration. In this chapter, a short overview of the SMOS mission is given, including the calibration principle of MIRAS. Calibration of MIRAS requires the provision of two accurately known signal noise levels to each of the multiple receivers of the interferometer; this is the task of the Calibration subsystem (CAS). A rigorous ground characterization campaign was conducted in order to characterize CAS performance in orbit, including a temperature –dependant model for the output level of the delivered calibration signals. A description of the Calibration subsystem and its characterization are included as a part of this thesis work [P6].

8.1. The SMOS mission

Originally proposed in 1998, SMOS was the second satellite to be developed in the series of Earth Explorer Opportunity missions of the European Space

Agency. The purpose of the mission is to provide global maps of ocean salinity and soil moisture – critical parameters in climate research studies as well as short-term weather forecasts. Soil moisture is a key variable in the hydrological cycle of the Earth, influencing water uptake of vegetation, evaporation and infiltration processes, and the water and energy fluxes between the soil and atmosphere. Ocean salinity, on the other hand, can be used to track ocean circulation processes, which offer further understanding of the behavior of, for example, ocean/atmosphere heat transfer in tropical areas. (Barré *et al.*, 2008).

8.1.1. Mission concept

The SMOS satellite (Figure 26) is positioned in a sun-synchronous orbit with a mean altitude of 750 km and an orbital inclination of 98.4°. In nominal operating mode, this provides an imaging swath width of 1050 km on the Earth surface, with a spatial resolution of 50 km (Barré *et al.*, 2008). Due to the imaging concept, each resolution cell is imaged with a wide range of incidence angles during the satellite overpass. The temporal coverage in the nominal operating mode is 3 days on the equator, with a repetition of the exact same orbit every 149 days.

The mission specifications defined for SMOS called for 4 % volumetric accuracy in the detection of soil moisture (in regions with a biomass of less than 4kg/m^2) at the nominal spatial resolution of the instrument. Similarly, for the detection of ocean salinity variations, the instrument was expected to deliver salinity maps with an accuracy of 3 to 5 psu (practical salinity units) at the nominal spatial resolution. The salinity maps can be aggregated to grid of 200 km at repeat periods of 10 days to provide maps with accuracy better than 0.1 psu (McMullan *et al.*, 2008). A detailed description of the SMOS mission is given by Barré *et al.* (2008).

Figure 26. An artist's conception of the SMOS satellite. Image: ESA.

8.1.2. Payload

The payload of SMOS, MIRAS, is comprised of multiple radiometers operating in the L-band. These are arranged geometrically in a Y-shape to provide a synthetic aperture significantly larger than that of individual antennas (see Figure 27). Each receiver, called LICEF (for Light-Weight Cost eFfective), measures the apparent scene brightness temperature through a wide-beam patch antenna in the frequency band of 1400-1427 MHz. The frequency band was selected due to its sensitivity to both soil moisture and sea surface salinity, as well as for being the lowest protected frequency band (reserved for radio astronomy).

The imaging concept of MIRAS is based on the measurement of cross-correlations of interferometric pairs, or baselines, formed by the multiple receivers. The measured correlations are used to synthesize the so-called visibility function (see section 3.2). An inverse Fourier transform of the visibility function then gives the brightness temperature of the measured scene (Corbella *et al.*, 2004). A comprehensive description of the payload is given by McMullan *et al.* (2008).

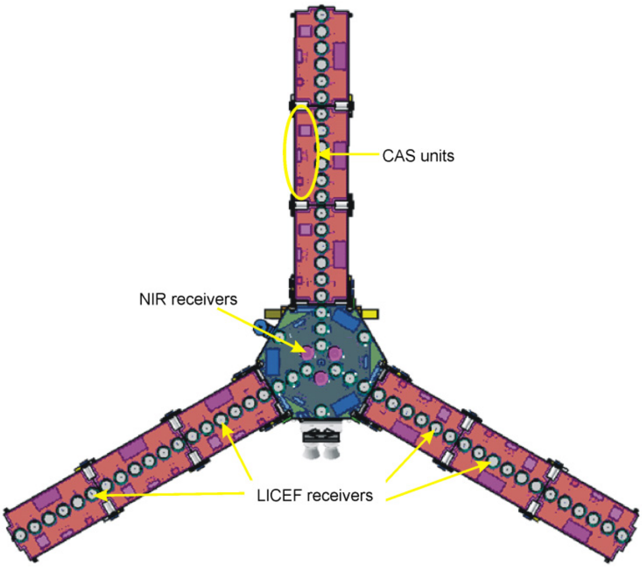

Figure 27. Distribution of LICEF receivers, NIRs and CAS units on MIRAS. Each arm segment includes 6 LICEF receivers, 1 Noise Source unit and 1 Power Divider unit. The hub includes 12 LICEF receivers, 3 NIR receivers, 1 Noise Source unit and 3 Power Divider units. Courtesy of EADS-CASA Espacio.

LICEF receivers

MIRAS houses 66 individual LICEF receivers, distributed in the three arms of the instrument as well as the central hub. The LICEF are Dicke-type receivers with downconversion from the nominal 1400-1427 MHz observation band. The downconverted signal is divided into I (In-phase) and Q (Quadrature) components and digitized at the signal output. The amplitude of the I-branch signal is measured by the LICEF PMS (Power Measurement System), giving the overall level of detected power. The receivers are fed through wide-beam patch antennas at two selective polarizations (termed X and Y). In addition, a front-end switch allows measurements of an internal terminated load (U-load), and a calibration signal of correlated noise (C), delivered by the calibration subsystem.

In addition, three Noise Injection Radiometers (NIR, see below), consisting of two LICEF units coupled to a common antenna, are included in the hub. Thus the total number of radiometers in the satellite is 69, with a total of 72 LICEF receivers.

Noise Injection Radiometers (NIR)

In addition to the standard LICEF units, MIRAS includes three precise Noise Injection Radiometers, housed in the central hub. The main task of the NIR units is to measure the average scene brightness temperature with high precision. As stated above, the NIR units are in fact a combination of two LICEF units coupled to a common antenna; this enables simultaneous measurements on both polarizations.

In the calibration process of MIRAS, the NIR units are used to perform two crucial tasks: 1) to calibrate the absolute brightness temperature of the measured scene and 2) to calibrate the two levels of correlated noise signal delivered by the Calibration subsystem (CAS), which is, in turn, used to calibrate the LICEF receivers. During normal operations, the NIR units act as other LICEF receivers, forming a part of the multiple baselines measured by the instrument. The NIR units themselves are calibrated periodically using the cold sky as reference; during this process, the entire satellite is turned to face the radiometrically cold sky. A comprehensive description of NIR design and operation is given by Colliander *et al.* (2007).

Calibration subsystem (CAS)

The SMOS Calibration subsystem (CAS) is designed to deliver a correlated calibration noise temperature to LICEF receivers at two known power levels (nominally 75 and 1200 K, known as the "warm" and "hot" levels, respectively). This enables a standard two-point calibration of receiver gain and offset. CAS is based on distributed noise injection, comprising of ten Noise Source (NS) units, one in the MIRAS hub (HNS) and three in each arm (ANS), ten 2-to-6 Power Divider (PD) units, and adjacent coaxial cabling. A block diagram of the CAS configuration in the hub and one adjacent arm is shown in Figure 28. During calibration, the absolute level of the CAS output is determined by the three NIR units in the instrument hub (fed by the hub NS unit). The distributed scheme allows tracking of the signal level phase and amplitude throughout the network, as remaining receivers are each connected to two NS units in adjacent segments (with the exception of LICEF units in arm segment 3).

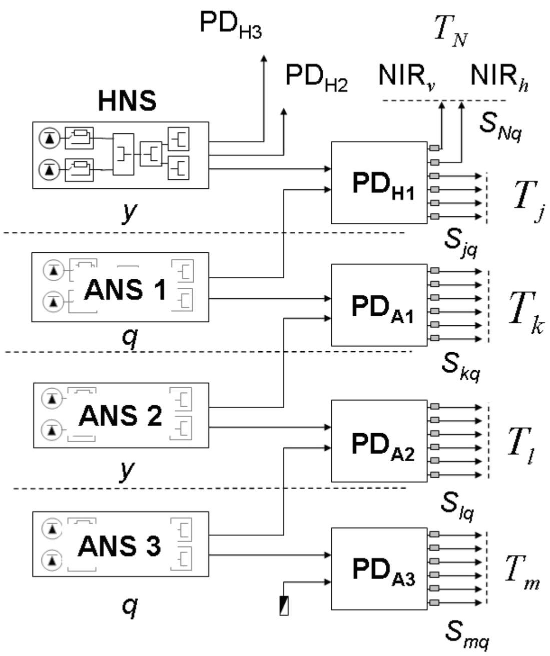

Figure 28. A block diagram of CAS configuration in the MIRAS' hub and one arm. The outputs to MIRAS' receivers are on the right, the NIR reference plane is indicated at the top and the LICEF reference plane to the right. *Kainulainen et al., (2009).* © 2009 IEEE.

8.2. Calibration of the SMOS payload

The calibration scheme of MIRAS relies both on instrument characterization measurements performed before launch (on-ground characterization), and regular calibration measurements performed during mission operations. The aim of the calibration procedure is to produce calibrated visibilities (see section 3.2), enabling later translation of these as brightness temperatures of the apparent scene using image reconstruction (Camps *et al.*, 1997).

The complete calibration scheme of SMOS is described by Brown *et al.* (2008) and Corbella *et al.* (2005). The in-orbit calibration consists of several procedures to calibrate different elements of the system; the frequency of these procedures varies, being a trade-off between the expected stability of the element and other mission requirements (i.e. scientific observation time versus time spent for calibrations). The procedures can be divided into internal and external calibrations. The internal calibration procedures give a regular measure and correction parameters for the instrument's stability during operations, the main parameter affecting stability being the thermal state of the receivers. Internal calibration is performed at the receiver reference plane, thus excluding the effect of antennas. The external calibrations, performed likewise regularly but at less frequent intervals, are used to derive absolute calibration parameters for the instrument.

The in-orbit calibration procedures are divided into five groups (Oliva *et al.*, in press)

- Long calibration procedure (internal calibration):
  - calibration of PMS gain and offset of all receivers;
  - calibration of Fringe-washing functions of baselines;
  - calibration of visibility offsets
- Calibration of only PMS offsets (internal calibration)
- Local oscillator calibrations (internal calibration)
- NIR absolute calibrations (external calibration)
- Flat Target Transformation (external calibration)

For external calibration (i.e. at the antenna reference frame) the satellite is rotated to face the radiometrically cold sky. As the cold sky is the only external calibration target readily available, the process is essentially a one-point calibration, relying on *a priori* knowledge of the sky brightness temperature and characteristics of the instrument derived on-ground. The absolute calibration of NIR and the Flat Target Response (FTR) are measured by this method. The internal noise injection signal of NIR is calibrated using the cold sky and on the other hand, the NIR internal (passive) load as references. The calibrated NIR then serves to act as the absolute reference of the visible brightness temperature scene; it is also used to calibrate the noise signal from the distributed noise injection network (i.e. CAS) during the long internal calibration, which is then used to calibrate the remaining LICEF receivers. Careful on-ground characterization of NIR is required to compensate e.g. for in-orbit temperature effects in the systems parameters (Colliander *et al.*, 2007).

The Flat Target Response is used to correct for non-idealities in the antenna beam patterns (Martin-Neira *et al.*, 2008). In principle, the instrument is used to measure a known flat (homogeneous) target; the non-ideal instrument response is then transferred to all other observations of diverse scenes. The FTR was first measured prior to launch in an anechoic chamber. However, it was noted during the commissioning phase of SMOS that the FTR had changed slightly from the one measured on ground. The change can possibly be attributed to small variations in the beam patterns of LICEF antennas. Therefore, the current calibration procedure calls for a regular update of the FTR.

The long calibration procedure is of most relevance concerning this thesis work, as in this the SMOS Calibration subsystem [P6] is applied. In essence, the purpose of the long calibration is to provide parameters for calibrating the normalized complex correlation coefficients measured by MIRAS, to correspond to the visibility function defined in section 3.2 (Corbella *et al.*, 2005).

From (3.8), it can be seen that in order to retrieve the visibilities V_{kj}, the system noise temperatures and the value of the fringe-washing function at the origin must be known. The system noise temperatures of the receivers can be obtained by calibrating the gain and offset of the PMS in the corresponding receiver; calibration of the fringe-washing function at the origin, in turn, requires knowledge of the phase imbalance between receivers (Corbella *et al.*, 2005). Determining both of these factors is done by injecting two levels of correlated noise to the receivers through the distributed noise injection network. As will be shown in the following sections, the accuracy of the calibration then depends on how accurately the level and phase of the correlated noise delivered to LICEF receivers is known. This, in turn, depends on the accuracy of CAS ground characterization (measurement of S-parameters over temperature), accuracy of temperature measurements of the instrument, and possible drifts after characterization (Corbella *et al.*, 2000).

Calibration of PMS gain and offset

Calibration of the measured visibilities requires knowledge of the system noise temperatures of the receiver pairs; thus, in order to determine $T_{sys,j}$, the gain and offset of the PMS must be calibrated. This is done using correlated noise injection from the calibration network; the four-point calibration scheme proposed by Piironen *et al.*, (2002) is applied. This is an extension of the standard two-point method, allowing the receiver offset to be calibrated independently of the input noise temperatures; this essentially reduces systematic errors of the calibration. The LICEF PMS have an in-built-in selective attenuator, that allow the two-level calibration signal to be further separated into four PMS readings for each receiver, so that four levels of calibration signal can be measured. The receiver offset can then be determined implicitly from measured voltages, without knowledge of the calibration noise injection levels (see [P6] Appendix and Piironen, 2002). For determining the system gain, however, accurate determination of the input noise levels T_C is required. The accuracy at which the calibration noise signals are known effectively determines the accuracy of the PMS calibration, as the measurement of LICEF voltages can be considered to be ideal.

In the first step of the calibration sequence the three NIR units in the hub section measure the level of T_N for the two noise injection levels. NIR, on the other hand, is calibrated at regular intervals using the cold sky as the external calibration reference. A detailed description of the calibration of the CAS noise level is given by Colliander *et al.* (2007). Using the S-parameters of CAS characterized on-ground, the noise level can be calculated to other output planes adjacent to T_N. The PMS gain of the hub section receivers can then be determined from (see [P6])

$$G_j = \frac{v_{j1} - v_{j2}}{\frac{|S_{Ny}|^2}{|S_{jy}|^2}\left(T_{N,j}^{C1} - T_{N,j}^{C2}\right)}, \qquad (8.3)$$

where $T_{N,j}^{C1} - T_{N,j}^{C2}$ is the noise level difference measured by NIR at CAS outputs during hot and warm noise injection, and S_{Ny} and S_{jy} are S-parameter gains of the network from the hub noise diode y to the NIR input plane and the input plane of receivers j, respectively. As pointed out above, the offset can be determined directly from the measured voltages (Piironen, 2002). The system noise temperature at the input plane of receivers j is simply

$$T_{sys,j} = \frac{v_j - v_{off,j}}{G_j}. \tag{8.4}$$

Due to the overlapping nature of the calibration network, the gain of the receivers in the following Arm segment of MIRAS can then be determined with an equation analogous to (8.3).

Calibration of Fringe washing function

Following (3.8), the fringe-washing function at origin must be determined in order to retrieve the visibilities from the correlations measured by MIRAS. Only the value of the fringe washing function at the origin is required; the complete fringe-washing function shape is needed, however, in the image reconstruction process (Corbella *et al.*, 2005). For calibration of the fringe washing function at the origin, it is required to correct for the phase difference of the noise distribution network paths between the two receivers forming the baseline under scrutiny (Corbella *et al.*, 2000). The phase difference of the signal paths is obtained from the ground characterization of CAS.

When measuring the same CAS Noise Source with receivers k and j, the obtained offset and quadrature corrected correlations obtained can be formulated so that ([P6], Corbella *et al.*, 2000):

$$M_{kj} = |M_{kj}|e^{j(\theta'_{kj})} = \tilde{r}_{kj}(0)\frac{|S_{kq}||S_{jq}|T_{Sq}}{\sqrt{T_{sys,k}T_{sys,j}}}e^{j(\theta_{kj}-(\theta_{jq}-\theta_{kq}))}\ , \tag{8.5}$$

where T_{Sq} is the noise temperature of Noise Source q connected to output k, S_{kq} and S_{jq} are the total attenuation from Noise Source q to outputs k and j, respectively, θ_{kq} and θ_{jq} are the arguments of the S-parameters of CAS from Noise Source q to receivers k and j, respectively, and θ'_{kj} is the measured phase of the correlation coefficient between receivers k and j. In the exponential term of (8.5), the actual phase imbalance θ_{kj} between the receiver pair is the parameter requiring calibration. This can be solved using the measured imbalance of the CAS transmission paths from source q, so that:

$$\theta_{kj} = \theta'_{kj} - \left(\theta_{kq} - \theta_{jq}\right). \tag{8.6}$$

Using knowledge of the phase of each signal path of CAS, the phase difference between two paths can be tracked. By this principle the relative phases between all receivers can be solved, allowing calibration of $\tilde{r}_{kj}(0)$ for all baselines.

8.3. On-ground characterization of the SMOS calibration subsystem

Characterization is the measurement of instrument performance and properties in specific conditions. In order for the calibration concept to succeed, the Calibration Subsystem (CAS) of the instrument had to undergo a rigorous on-ground characterization. The purpose of CAS, as explained in section 8.2, is to deliver a correlated noise signal to LICEF receivers for internal calibration. The main purpose of the characterization of CAS was to provide a mathematical model for calculating and correcting for deviations in the signal distribution network, so that the amplitude and phase of the correlated noise signals could be accurately determined at outputs of the network in varying environmental conditions. While in orbit, the characteristics of the network vary mainly due to temperature changes induced by orbital conditions and, for example, spacecraft attitude (Brown *et al.*, 2008). The design and characterization of CAS is described in the following.

8.3.1. CAS components

CAS is a distributed noise injection network formed by noise sources, power dividers and coaxial cabling connecting the CAS units to LICEF receivers (see 8.1.2, Figure 28). A simplified block diagram of the CAS Hub section noise source design is shown in Figure 29. The units in the MIRAS arm segments are otherwise identical, but with only two output connectors.

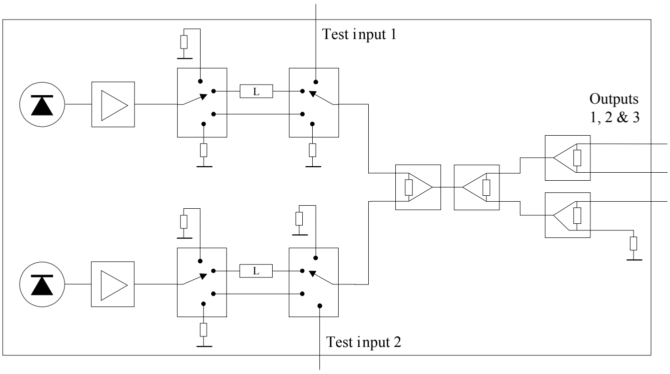

Figure 29. Simplified block diagram of the CAS Hub Noise Source unit. *Lemmetyinen et al. (2007) [P6].* © 2007 IEEE.

Using two RF switches in series, two distinct noise temperature levels can be generated at the NS output; the “hot” and “warm” levels (approx. 65000 and 5000 K, respectively). Reduced to the output of the CAS subsystem (i.e., the input of individual receivers), the correlated hot and warm noise levels (thermal noise subtracted) are approximately 1200 K and 75 K, respectively. In addition to this, the output includes the (uncorrelated) noise of the distribution network itself. A test input was included to allow characterization (i.e. measurement of S-parameters) of the different transmission paths inside the units.

The Power Divider units include a Wilkinson type power combiner followed by three cascaded stages of Wilkinson dividers. This results in $2^3 = 8$ signal outputs; two of the outputs are internally terminated. A 4 dB attenuator is attached to each output port of a PD unit in order to improve isolation between ports. A photograph of one NS and one PD unit is shown in Figure 30.

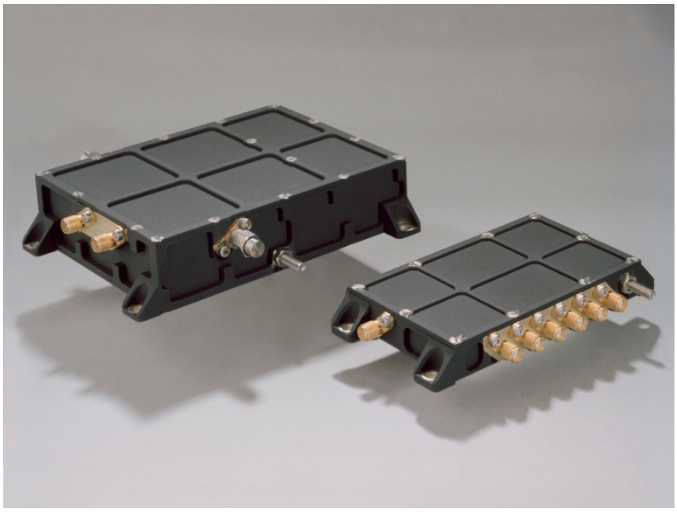

Figure 30. The Arm Noise Source (left) and the Power Divider (right) units of CAS. Photograph: Ylinen Electronics Oyj.

8.3.2. Measurement of S-parameters

The main task of CAS characterization consisted of characterizing the S-parameters of the noise distribution, i.e. defining the transmission and insertion losses and phase shifts in different paths of the network. The network S-parameters had to be characterized over a range of temperatures, as it was anticipated that changes in ambient temperature in orbit would change these from the base values measured at room temperature. The effect was estimated to be the largest in the long connection cables from noise sources to the power divider units, as well as in the cables connecting power dividers to LICEF receivers. Furthermore, it was anticipated temperature gradients could form over the network; i.e. parts of the network would be at differing temperature. As this would form an infinite number of temperature conditions to characterize, segments of the network had to be characterized individually. The goal was to build a mathematical model for calculating an approximation of the total change in S-parameters of CAS, allowing for temperature differences over the network. The characteristics (noise level and relative phase) at the outputs of the whole CAS subsystem were retrieved by combining the characteristics of all individual components in a signal path as a function of temperature, so that

$$S_{kq} = \prod_{n=1}^{N} S_{nq}^{T_{phys}}, \qquad (8.7)$$

where $S_{nq}^{T_{phys}}$ is the transmission S-parameter of unit or cable n at temperature T_{phys}. The total transmission loss is composed of four components: (1) S-parameters of the signal path inside the Noise Source, (2) S-parameters of the cables connecting Noise Source to a Power Divider, (3) S-parameters of the Power Divider, and finally, (4) S-parameters of the cable connecting the Power Divider to a receiver input. In practice, only the relative S-parameters between CAS paths are required (see section 8.2); the value for (1) can thus be acquired directly from the measurement of S-parameters from the NS test input to outputs (see Figure 29) although this does not reflect the entire signal path from the noise diode.

The accuracy of the model was verified at room temperature by comparing the S-parameters of the assembled CAS to those given by (8.7). The Hub noise source unit, one Arm noise source unit and one Power Divider Unit were assembled on a mechanical mock-up of the satellite's Hub and one Arm segment, including interconnecting coaxial cables. Note that the complete CAS was not measured in this way due to the limited amount of connector matings allowed for the system during testing. The S-parameters of the complete noise transmission path were measured from the NS test ports to the LICEF input plane. The measured S-parameters were compared to those predicted by the model based on measurements of individual segments of CAS, taking also into account the physical temperature of the assembled network. The ambient temperature of the network was measured from the PD and NS unit casings; with these readings, it was also possible to estimate the physical temperatures of the connecting cables.

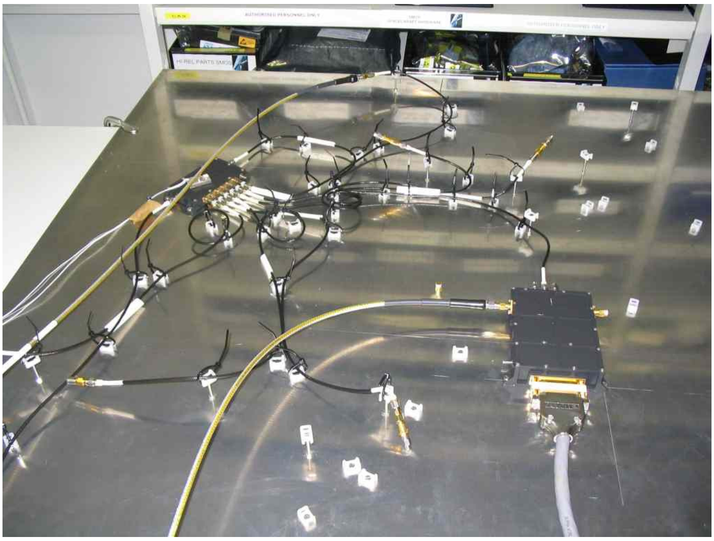

Figure 31. The Hub section Noise Source and Power Divider units and coaxial cabling connected to a mechanical mock-up of MIRAS for measurement of S-parameters. Photograph: Ylinen Electronics Oyj.

The calculated transmission loss (S21) for one CAS signal path as a function of temperature is shown in Figure 32; error bars reflect the expected uncertainty of the calculation.

Based on comparison of the modeled and measured S-parameters of the assembled CAS, it was estimated that any individual baseline can be characterized with an uncertainty of 0.044 dB (1.02%) in relative amplitude and 1.41° in relative phase. The errors arise from non-repeatability of SMA connection matings, bending of the cables during the final assembly of CAS (affecting in particular the phase characteristics), and the calibration error of the vector network analyzer used to measure the parameters. Also, the non-ideality of port input matching causes multiple reflections from cable-to-unit connections; technically, the input matching of unit and cable ports was measured during the test campaign, but applying these in the calculation of system S-parameters in (8.7) did not improve the comparison of modeled and measured S-parameters, and thus these were omitted from the calculations.

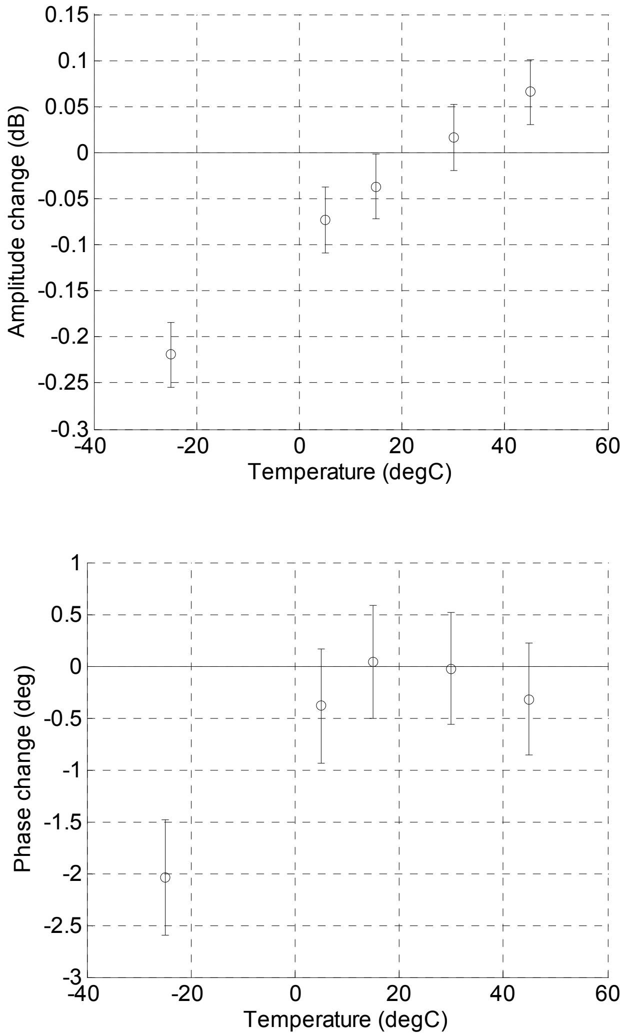

Figure 32. Total calculated change of S_{21} with temperature for amplitude (above) and phase (below) of a typical CAS transmission path, from NS unit's test input to the output of CAS. *Lemmetyinen et al., (2007) [P6].* © 2007 IEEE.

In addition to the characterization of S-parameters over temperature, also the stability of the noise source output noise level over temperature was characterized. This information is not, however, currently required for the calibration process itself as the CAS output is considered stable during the 30-second period between the calibration of the signal level by NIR units and correlated noise injection to the last LICEF units. As a part of the test campaign, CAS also underwent rigorous environmental testing including mechanical vibration and shock tests, thermal vacuum tests and sensitivity to electromagnetic interference.

8.3.3. Propagation and effects of characterization errors

As pointed out in the previous section, the characterization of CAS involves errors in the noise distribution network phase and amplitude originating from the uncertainty of the S-parameter model. These errors induce uncertainties in the calibration of LICEF PMS voltages through (8.3) and definition of the fringe washing factor at origin by using phase differences of CAS signal paths (8.6), which in turn induce errors to the calibrated visibilities of MIRAS. Due to the cascaded nature of the characterization process, this error increases as more measured values (CAS S-parameters) are required to determine the transmission loss and phase of the network, relative to the calibrated value measured by the NIR receivers located in the Hub (see section 8.2). The propagation of the error is analyzed in [P6] and in the follow-on study by Kainulainen *et al.* (2009); a brief summary is given here as this has a major impact on the overall calibration of MIRAS.

In the first phase of the PMS calibration, the calibration noise signal is measured using the NIR receivers. In order to reduce measurement uncertainty, the current calibration protocol uses an average of the temperatures measured by the six receivers housed by the three NIRs. The PMS gain of the four LICEF receivers j in the Hub section (see Figure 28) is then

$$G_j = \frac{v_{j1} - v_{j2}}{\frac{\left|S_{jy}\right|^2}{N} \sum_{n=1}^{N} \frac{\left(T_{N,j}^{C1} - T_{N,j}^{C2}\right)}{\left|S_{ny}\right|^2}}, \qquad (8.8)$$

where N = 6. Similarly to the amplitude calibration, averaging can be used to reduce the accumulation of error when calculating the phase imbalance. Using (8.6), the imbalance of receivers in sections j and l, separated by receivers k, is

$$\theta_{jl} = \frac{1}{N} \sum_{n=1}^{N} \left[\theta'_{kj} - \left(\theta_{knq} - \theta_{jq}\ \right) + \theta'_{kl} - \left(\theta_{kny} - \theta_{ly}\right)\right]. \qquad (8.9)$$

Averaging can be similarly used when measuring the PMS gain of receivers in the following section, now using noise signals measured by the four calibrated LICEF units as a reference. Considering both the NIR-measured system noise temperatures $T_{N,j}$ and the LICEF PMS voltages and internal attenuator transmission losses (υ_{kn} and L_1) to be ideal, and furthermore assuming uncertainties of the measured S-parameter gains to be independent of one another, the uncertainty of G_j can be calculated using the standard propagation of errors (Kainulainen *et al.*, 2009):

$$\Delta G_j = \sqrt{\left(\frac{\partial G_j}{\partial S_{jy}} \Delta S_{jy}\right)^2 + \sum_{N=1}^{6} \left(\frac{\partial G_j}{\partial S_{Ny}} \Delta S_{Ny}\right)^2}. \tag{8.10}$$

Errors in the measurement of G_j thus consist solely of errors caused by the determination of the S-parameters of CAS (ΔS_{jy}, ΔS_{Ny}). Similarly, the phase error is dependent on the errors in measured phases of the two baselines. The uncertainty can again be alleviated using averaging over the common reference receivers k as given by Kainulainen *et al.*, 2009:

$$\Delta \theta_{kp} = \sqrt{\left(\Delta \theta_{jq}\right)^2 + \left(\Delta \theta_{ly}\right)^2 + \frac{\left(\Delta \theta_{knq}\right)^2}{N} + \frac{\left(\Delta \theta_{kny}\right)^2}{N}}. \tag{8.11}$$

However, for the following arm sections the uncertainty of the determination of the gain introduces an error to the determination of $T_{SYS,C}$. Now, an added uncertainty is already present in (8.10), increasing the total error when proceeding towards the last section. Similarly, the uncertainty of the phase is increased when the number of steps required to calculate the relative phases of CAS transmission paths increases.

The impact of the errors on the visibility amplitude and phase calibration was first analyzed numerically; the propagation of error was determined by simulating the calibration of LICEF units in different sections using equations (8.8) and (8.9), using actual measured values for the S-parameters of CAS. Furthermore, a Gaussian distributed error with a variance of 0.05 dB was introduced to measured S_{21} values of CAS signal paths. The resulting uncertainty to T_{sys} was simulated, calculating the sum of squares error between receivers in all MIRAS baselines. The results, plotted on the MIRAS baseline visibility chart are presented in Figure 33. Using a common system noise temperature value of T_{sys} = 300 K, the resulting errors range from less than 1 K in the footprint centre of the chart to 8 K near baselines at the edges.

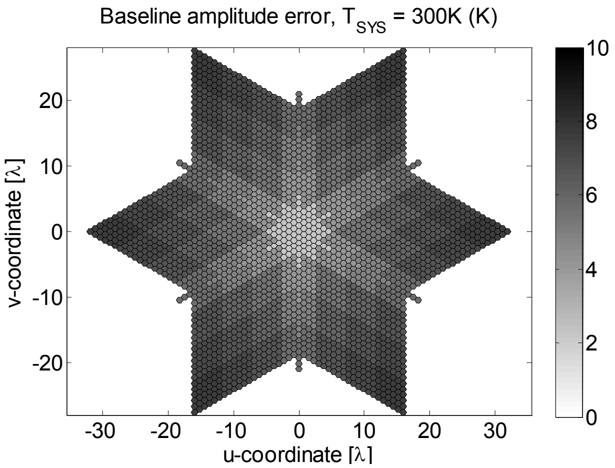

Figure 33. Simulated propagation of error in system noise temperature on MIRAS baseline chart. *Lemmetyinen et al., (2007) [P6].* © 2007 IEEE.

The accumulated error of the calibrated phase was simulated similarly to the amplitude error, by introducing a Gaussian distributed error with 1° variance to all measured values of the phase of CAS' signal path when calculating the calibrating the phase difference of receivers analogously to (8.9). The resulting error plotted on the MIRAS footprint chart is shown in Figure 34. The smallest errors of 1.4° are located in the center of the footprint, increasing to close to 2° near the edges.

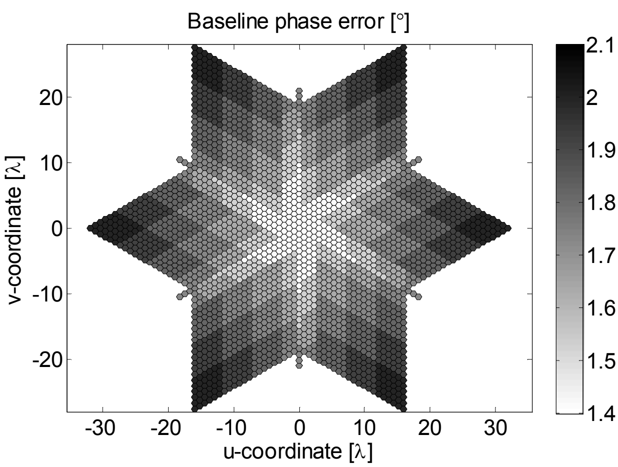

Figure 34. Simulated propagation of error in CAS phase correction on MIRAS baseline chart. *Lemmetyinen et al. (2007) [P6].* © 2007 IEEE.

In a follow-on study to [P6], an analytical method for analysing the propagation of the errors induced by CAS was presented by Kainulainen *et al.* (2009).

Figure 35 demonstrates the calculated propagation of error by baselines between receivers in different sections (see Figure 28). As a percentage of the visibility amplitude, the errors range from 0.8 % for the shortest baselines (i.e. receivers in the same sections) to 1.3 % for receivers in the same arms but at the last segment. It is notable that these errors were estimated to be larger than those induced by CAS for receivers at the ends of opposing arms. This is due to receivers in one arm being subject to a common bias, originating from the first PMS gain calibration. Similarly, subsequent calibrations add to the error in the same direction for each receiver. However, receivers in opposing arms are subject to differing errors, as the first and subsequent PMS calibrations differ. Thus these biases accumulate quadratically, and the resulting total error is smaller than for receivers situated in the same arm (Kainulainen *et al.*, 2009).

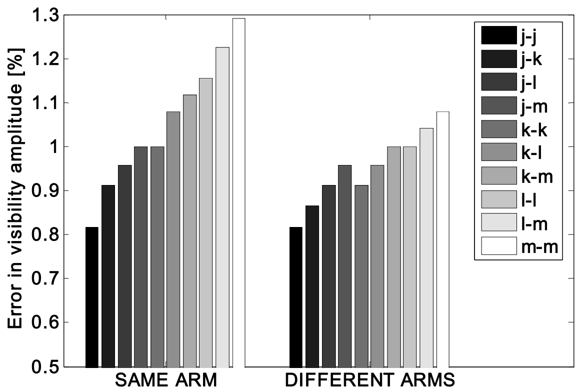

Figure 35. Calculated propagation of error of the visibility amplitude. Error bars at the left side shows the case of receivers located in the same arm of the instrument, and the bars at the right the case of receivers located in different arms of the instrument. *Kainulainen et al. (2009).* © 2009 IEEE.

A similar chart for the propagation of visibility phase error is shown in Figure 36. Now, most baselines in the same arm of the instrument can be seen to match the value of 1.41° (quadratic sum of 1° errors, assumed for single baseline). This result is intuitive, as baselines in the same arm can be related to one another via a maximum of two adjacent baselines. For receivers at end segments *m* of opposing arms, however, a maximum of seven adjacent baseline calculations are required.

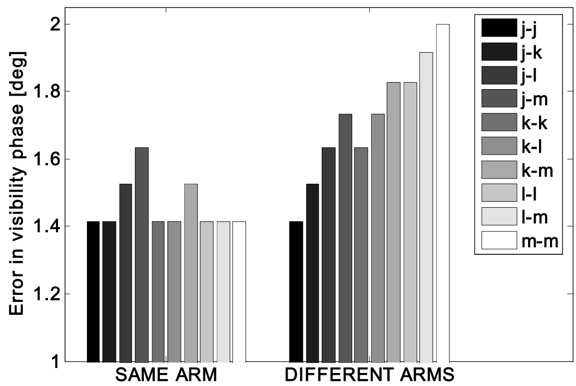

Figure 36. Calculated propagation of visibility phase error. Error bars at the left side shows the case of receivers located in the same arm of the instrument, and the bars at the right the case of receivers located in different arms of the instrument. *Kainulainen et al.(2009)*. © 2009 IEEE.

In [P6] and the follow-on study by Kainulainen *et al.* (2009) the final impact of the CAS characterization errors on MIRAS visibilities was analyzed using the SMOS End-to-End Simulator, SEPS (Camps *et al.*, 2003). SEPS was first applied to simulate visibilities considering an ideal characterization of CAS and other parts of the instrument for several scenes (a homogeneous sea surface, a homogeneous land surface, and two mixed land/ocean scenes). The visibilities, in turn, were inverted into ideal brightness temperature scenes, or snapshots. Next, a set of visibility amplitude errors was created, following the statistical probability of errors over different baselines as depicted in Figure 35 and 36. Errors were created separately for amplitude and phase characterization errors of CAS. Lastly, these errors were added to the ideal visibilities, and the image inverted to brightness temperatures using SEPS. The resulting images were then compared to the ideal images, allowing some insight into the effect of CAS characterization uncertainty on the obtained brightness temperature images.

Figure 37 (from Kainulainen *et al.*, 2009) shows SEPS simulations for two of the scenes, an open sea scenario and a scenario of mixed land and ocean signatures. The top row displays the brightness temperatures as would be measured by an ideal instrument, including an ideally characterized CAS. In the middle row images, an error is introduced to the CAS amplitude characterization following the methodology described above. The displayed images depict the difference between the ideal image and the obtained “erroneous” brightness temperature map. Similar error maps for the phase characterization uncertainty are shown in the bottom row of Figure 37. For both scenarios, the resulting standard deviation of errors is less than 0.5 K for the impact of amplitude errors, and less than 0.8 K for the impact of phase errors. The amplitude uncertainty introduces a positive bias ranging from 0.02 to 0.61 K depending on the test scenario, while the phase uncertainty introduces a small negative bias error (under 0.1 K in all cases, Kainulainen *et al.*, 2009, Table IV). The flat ocean signature exhibits, in general, smaller errors than do the mixed scenes. Also, a clear qualitative correlation can be found between the brightness temperature contrasts of the mixed scenery map (Figure 37 top row) and the distribution of phase and amplitude errors, indicating the strong dependence of the errors on the measured scene.

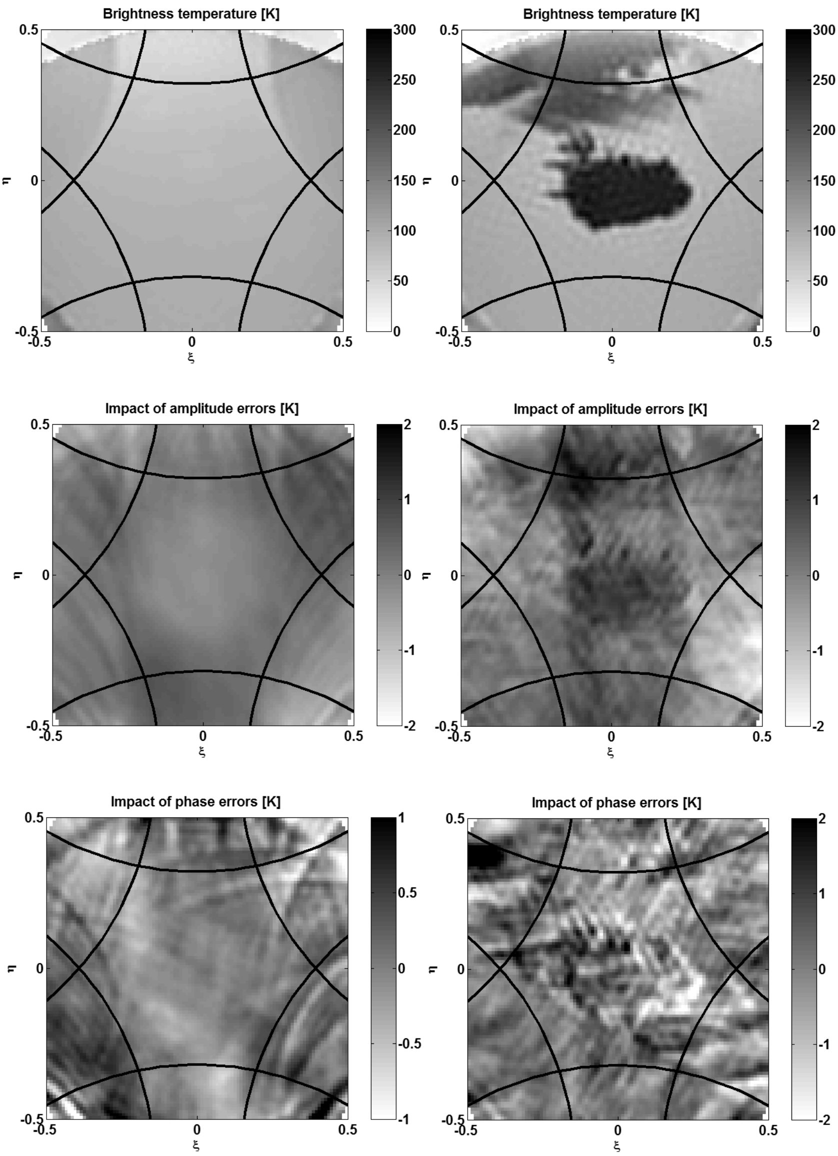

Figure 37. Simulated test scenarios of MIRAS brightness temperatures using SEPS, including effect of CAS characterization errors. Open sea scenario (left column) and mixed land/ocean scenario (right column). Top row images simulated using an ideal instrument, including an ideally characterized CAS. Middle row: Error introduced by the CAS' S-parameter gain uncertainty in ground characterization (1% per signal path). Bottom row: Error introduced by the CAS' S-parameter phase uncertainty in ground characterization (1° per signal path). Limits of alias-free field of view indicated with black arcs. *Kainulainen et al.*, 2009. © 2009 IEEE.

9. Conclusions

This thesis work brings together several studies concerning remote sensing methods of the cryosphere by applying microwave remote sensing. The presented studies contribute to the understanding of microwave signatures of complex natural environments through extensive experimental datasets over the Northern Hemisphere, including tundra, boreal forests, wetlands and lake ice ([P1], [P2], [P3]). This is necessary in order to explore ways to improve the accuracy of current retrieval methods of snow parameters from spatially coarse radiometer observations (e.g. Kelly *et al.*, 2003, Takala *et al.*, 2011). Moreover, the study looks into the calibration method devised for a novel type of radiometer instrument, an imaging interferometric radiometer using aperture synthesis.

9.1. Contribution of work to remote sensing of the cryosphere

The modeling of microwave emission is an important aspect in attempting to understand the factors affecting the detected signatures. This thesis work presents extensive modeling efforts for various aspects of the cryosphere, including snow-covered terrain ([P1]), lake ice ([P1], [P3], [P4], and the effects of soil freezing and thawing ([P5]). The work included the revising of an existing snow emission model (Pulliainen *et al.*, 1999) to simulate the emission from vertically stacked layers of snow and ice.

The work also indicates possibilities for the application of the revised forward model in the retrieval of snow characteristics from space-borne radiometer observations. The study in [P4] demonstrates an increase of retrieval accuracy using the revised model, by means of a method compensating for the deteriorating effect of water bodies in the satellite scene. The method can be applied to potentially improve the accuracy of present retrieval algorithms based on inversion of physical forward models (e.g. Takala *et al.*, 2011).

Furthermore, the study presented in [P5] indicates interesting possibilities for the monitoring of soil freeze/thaw processing using L-band microwave remote sensing. Methods based on existing operational satellites with higher frequency channels have been presented in the literature (e.g. using SSM/I channels at 10.65, 19 and 37 GHz in Zhang *et al.*, 2001), but the L-band offers in this case the unique opportunity of being relatively insensitive to the presence of dry snow cover. With the launch of the SMOS satellite in 2009, L-band observations are now also available globally at regular intervals.

9.2. Contribution of work to the SMOS mission

The study presented in [P6] represents a major effort in the design, development and characterization of the SMOS calibration subsystem, CAS. The characterization test campaign of CAS was a particularly important aspect, as careful characterization was a prerequisite for the calibration of MIRAS to within mission requirements. The main goal of the characterization, i.e. the ability to calculate the effect of the CAS network on the correlated noise signals delivered to LICEF receivers was met; the relative phases and amplitudes of different signal paths can also be determined over a range of possible in-orbit temperatures. The analysis presented of the effects of CAS errors was significant in broadening the understanding of the impact of characterization errors on the final brightness temperature product given by MIRAS; this aids to further determine the overall uncertainty of the MIRAS observation, and also contributes to the design of possible future instruments. The matter of error propagation was further explored in a continuation study by Kainulainen *et al.* (2009); in the study, the impact of CAS characterization uncertainties was confirmed to be strongly dependant on the observation baseline, i.e. the physical location of the receiver pair. After launch, the calibration subsystem, as well as the MIRAS radiometer as a whole, has been proven to function to within specifications (Corbella *et al.*, 2011; Oliva *et al.*, in press).

References

Adams, W. P., and D. C. Lasenby, 1978. The role of ice and snow in lake heat budgets. *Limnol. Oceanogr.*, 23(5), 1025–1028.

Adams, W. P., and D. C. Lasenby, 1985. The roles of snow, lake ice and lake water in the distribution of major ions in the ice cover of a lake. *Ann. Glaciol.,* 7, 202–207.

Andreadis K., D. Liang, L. Tsang, D. P. Lettenmaier, and E. Josberger, 2008. Characterization of errors in a coupled snow hydrology-microwave emission model. *J. Hydrometeorol.*, 9(1), 149–164.

Atkinson, P. M. and R. E. J. Kelly, 1997. Scaling-up point snow depth data in the U.K. for comparison with SSM/I imagery. *Int. J. Remote Sens.*, 18, 437–443.

Barnett, T., J. Adam and D. Lettenmaier, 2005. Potential impacts of a warming climate on water availability in snow-dominated regions. *Nature*, 438, 303-309.

Barré, H. M. J., B.Duesmann, and Y. Kerr, 2008. SMOS: The mission and the system. *IEEE Trans. Geosci. Remote Sens.*, 46(3), 587-593.

Born, M. and E. Wolf, 1999. Principles of Optics: Electromagnetic Theory of Propagation, Interference, and Diffraction of Light. 7th ed., Cambridge, England: Cambridge University Press.

Boyarskii D. A. and V. V. Tikhonov, 2000. The influence of stratigraphy on microwave radiation from natural snow cover. *J. Electromagn. Waves Appl.*, 14(9), 1265–1285.

Brasnett, B., 1999. A global analysis of snow depth for numerical weather prediction. *J. Appl. Meteorol.,* 38: 726-740.

Brown, M. A., F. Torres, I. Corbella, A. Colliander, 2008. SMOS calibration. *IEEE Trans. Geosci. Remote Sens.*, 46(3), 646-658.

Brown, R. D., and R. O. Braaten, 1998. Spatial and temporal variability of Canadian monthly snow depths, 1946– 1995, *Atmos. Ocean*, 36, 37– 45.

Brun, E., E. Martin, V. Simon, C. Gendre, and C. Coleou, 1989. An energy and mass balance model of snow cover suitable for operational avalanche forecasting. *J. Glaciol.*, 35(121), 333–342.

Cagnati, A., A. Crepaz, G. Macelloni, P. Pampaloni, R. Ranzi, M. Tedesco, M. Tomirotti, and M. Valt, 2004. Study of the snow melt-freeze cycle using multi-sensor data and snow modelling. *J. Glaciol.*, 50(170), 419-426.

Camps, A., I. Corbella, M. Vall-llossera, N. Duffo, F. Marcos, F.Martinez-Fadrique, and M. Greiner, 2003. The SMOS End-to-end Performance Simulator: description and scientific applications. *Proc. 2003 IGARSS*, 13-15.

Camps, A., J. Bara, I. Corbella, and F. Torres, 1997. The processing of hexagonally sampled signals with standard rectangular techniques: Application to 2-D large aperture synthesis interferometric radiometers. *IEEE Trans. Geosci. Remote Sens.*, 35(1), 183–190.

Chang, A., J. Foster, and D. Hall, 1987. Nimbus-7 SMMR derived global snow cover parameters. *Ann. Glaciol.*, 9, 39-44.

Choudhury, B. J., T. J. Schmugge, R. W. Newton, and A. Chang, 1979. Effect of surface roughness on the microwave emission from soils. *J. Geophys. Res.*, 84, 5699–5706.

Clark, M.P., M.C. Serreze, and D.A. Robinson, 1999. Atmospheric controls on Eurasian snow extent. *Int. J. Climatol.*, 19, 27–40.

Colbeck, S., 1991. The layered character of snow covers. *Rev. Geophys.*, 29(1), 81–96.

Colliander, A., L. Ruokokoski, J. Suomela, K. Veijola, J. Kettunen, V. Kangas, A. Aalto, M. Levander, H. Greus, M.T. Hallikainen, and J. Lahtinen, 2007. Development and calibration of SMOS reference radiometer. *IEEE Trans. Geosci. Remote Sens.*, 45(7), 1967-1977.

Comiso, J.C., J. D. Cavalieri, C. L. Parkinson, P. Gloersen, 1997. Passive microwave algorithms for sea ice concentration: A comparison of two techniques, *Remote Sens. Environ.*, 60(3), 357-384.

Corbella, I., A. Camps, F. Torres, and J. Bara, 2000. Analysis of noise-injection networks for interferometric-radiometer calibration. *IEEE Trans. Microw. Theory Tech.*, 48(4), 545–552.

Corbella, I., F. Torres, A. Camps, A. Colliander, M. Martin-Neira, S. Ribo, K. Rautiainen, N. Duffo, M. Vall-llossera, 2005. MIRAS end-to-end calibration: application to SMOS L1 processor *IEEE Trans. Geosci. Remote Sens.*, 43(5), 1126- 1134.

Corbella, I., F. Torres, N. Duffo, V. González-Gambau, M. Pablos, I. Duran, M. Martín-Neira, 2011. MIRAS calibration and performance: results from the SMOS in-orbit commissioning phase. *IEEE Trans. Geosci. Remote Sens.*, 49(9), 3147-3155.

Corbella, I., N. Duffo, M. Vall-llossera, A. Camps, F. Torres, 2004. The visibility function in interferometric aperture synthesis radiometry. *IEEE Trans. Geosci. Remote Sens.,* 42(8). 1677- 1682.

De Roo, R., A. Chang, and A. England, 2007. Radiobrightness at 6.7-, 19-, and 37-GHz downwelling from mature evergreen trees observed during the Cold Land Processes Experiment in Colorado. *IEEE Trans. Geosci. Remote Sens.,* 45(10), 3224-3229.

Derksen C., A. Walker, E. LeDrew, and B. Goodison, 2002. Time series analysis of passive microwave derived central North American snow water equivalent imagery. *Ann. Glaciol.*, 34, 1-7.

Derksen, C., 2008. The contribution of AMSR-E 18.7 and 10.7 GHz measurements to improved boreal forest snow water equivalent retrievals. *Remote Sensing Environ.,* 112(5), 2701–2710.

Derksen, C., A. Walker, and B. Goodison. 2003. A comparison of 18 winter seasons of in situ and passive microwave derived snow water equivalent estimates in Western Canada. *Remote Sens. Environ.*, 88(3), 271-282.

Derksen, C., P. Toose, A. Rees, L. Wang, M. English, A. Walker, and M. Sturm, 2010. Development of a tundra-specific snow water equivalent retrieval algorithm for satellite passive microwave data. *Remote Sens. Environ.,* 114, 1699-1709.

Derksen, C., Sturm, M., Liston, G., Holmgren, J., Huntington, H., Silis, A., *et al.*, 2009. Northwest Territories and Nunavut snow characteristics from a sub-Arctic traverse: Implications for passive microwave remote sensing. *J. Hydrometeorol.,* 10(2), 448–463.

Dicke, R. H., 1946. The measurement of thermal radiation at microwave frequencies. *Rev. Sci. Instr.*, 17, 268-275.

Dobson, M. C., F. T. Ulaby, M. T. Hallikainen, and M. A. El-Rayes,1985. Microwave dielectric behavior of wet soil—Part II: Dielectric mixing models. *IEEE Trans. Geosci. Remote Sens.*, GRS-23, (1), 35–46.

Duguay, C., G. Flato, M. Jeffries, P. Menard, K. Morris, and W. Rouse, 2003. Ice-cover variability on shallow lakes at high latitudes: model simulations and observations. *Hydrol. Processes,* 17, 3465-3483.

Durand, M., E. J. Kim and S. A. Marguilis, 2008. Quantifying uncertainty in modeling snow microwave radiance for a mountain snowpack at the point-scale, including stratigraphic effects. *IEEE Trans. Geosci. Remote Sens.,* 46(6), 1753 – 1767.

Dyer, J., and T. Mote, 2006. Spatial variability and trends in observed snow depth over North America. *Geophys. Res. Lett.*, 33, L16503, 6 pp.

Fitzharris, B.B., *et al.*, 1996. The cryosphere: changes and their impacts. In: Climate Change 1995: Impacts, Adaptations and Mitigation of Climate Change: Scientific-Technical Analyses, Contribution of Working Group II to the Second Assessment Report of the Intergovernmental Panel on Climate Change (IPCC). R.T. Watson, M.C. Zinyowera, R.H. Moss and D.J. Dokken (eds.), Cambridge University Press, Cambridge, UK.

Font, J., A. Camps, A. Borges, M. Martin-Neira, J. Boutin, N. Reul, Y. Kerr, A. Hahne, S. Mecklenburg, 2010. SMOS: The challenging sea surface salinity measurement from space. *Proc. IEEE*, 98(5), 649-665.

Foster, J. A. Chang, D. Hall, 1997. Comparison of snow mass estimates from a prototype passive microwave snow algorithm, a revised algorithm and a snow depth climatology. *Remote Sens. Environ.,* 62: 132-142.

Foster, J. L., A. Rango, D. K. Hall, A. T. C. Chang, L. J. Allison, and B. C. Diesen, 1980. Snowpack monitoring in North America and Eurasia using passive microwave satellite data. *Remote Sens. Environ.,* 10, 285-298.

Foster, J., A. Chang, D. Hall, and A. Rango, 1991. Derivation of snow water equivalent in boreal forests using microwave radiometry. *Arctic*, 44, 147-152.

Foster, J., C. Sun, J. P.Walker, R. Kelly, A. Chang, J. Dong, and H. Powell, 2005. Quantifying the uncertainty in passive microwave snow water equivalent observations. *Remote Sens. Environ.*, 94(2), 187–203.

Fox, N., and A.J. Illingworth, 1997. The potential of space borne cloud radar for the detection of stratocumulus clouds. *J. Appl. Meteorol.,* 36, 676-687.

Gloersen P., F. T. Barath, 1977. A scanning multichannel microwave radiometer for Nimbus-G and Seasat-A. *IEEE J. Oceanic Eng.,* 2, 172-178.

Goggins, W. B., 1967. A microwave feedback radiometer. *IEEE Trans. Micro Theory and Tech.*, MTT-29, 344-347.

Goita, K., A. Walker, and B. Goodison, 2003. Algorithm development for the estimation of snow water equivalent in the boreal forest using passive microwave data. *Int. J. Remote Sens.*, 24(5), 1097-1102.

Goodison, B., and A. Walker, 1995. Canadian development and use of snow cover information from passive microwave satellite data. In: Choudhury, B., Y. Kerr, E.Njoku, and P. Pampaloni (eds.). Passive Microwave Remote Sensing of Land-Atmosphere Interactions. VSP BV, Utrecht, Netherlands, 245-262.

Grandell, J., J. Pulliainen, and M. Hallikainen, 1998. Sub-pixel land use classification and retrieval of forest stem volume in the boreal forest zone by employing SSM/I data. *Remote Sens. Environ.,* 63(2), 140-154.

Groisman, P. Ya, T.R. Karl, and R.W. Knight, 1994: Observed impact of snow cover on the heat balance and the rise of continental spring temperatures. *Science*, 263, 198–200.

Hall, D. K., 1987. Influence of depth hoar on microwave emission from snow in Northern Alaska. *Cold Regions Sci. Technol.*, 13, 225–231.

Hallikainen, M. T. and P. A. Jolma, 1992. Comparison of algorithms for retrieval of snow water equivalent from Nimbus-7 SMMR data in Finland. *IEEE Trans. Geosci. Remote Sens.*, 30, 124–131.

Hallikainen, M. T., 1984. Retrieval of snow water equivalent from Nimbus-7 SMMR data: effect of land-cover categories and weather conditions. *IEEE J. Oceanic Eng.,* OE-9, 372-376.

Hallikainen, M. T., F. Ulaby, and M. Abdelrazik, 1986. Dielectric properties of snow in the 3 to 37 GHz range. *IEEE Trans. Antennas Propagat.,* AP-34, 1329–1340.

Hallikainen, M. T., F. Ulaby, and T. Deventer. 1987. Extinction behavior of dry snow in the 18- to 90-GHz range. *IEEE Trans. Geosci. Remote Sens.*, GE-25, 737–745.

Hallikainen, M. T., P. A. Jolma, 1986. Retrieval of the water equivalent of snow cover in Finland by satellite microwave radiometry. *IEEE Trans. Geosci. Remote Sens.*, GE-24(6), 855-862.

Hallikainen, M. T., P. A: Jolma, and J. M. Hyyppä, 1988. Satellite microwave radiometry of forest and surface types in Finland. *IEEE Trans. Geosci. Remote Sens.*, GE-26, 622-628.

Han, Y., and E. R. Westwater, 2000. Analysis and improvement of tipping calibration for ground-based microwave radiometers. *IEEE Trans. Geosci. Rem. Sens.,* 38 (3), 1260-1276.

Hardy, W. N., K. W. Gray, and A. W. Love, 1974. An S-band radiometer design with high absolute precision. *IEEE Trans. Micro. Theory and Tech.,* MTT-22, 382-390.

Hoer, C. A., K. C. Roe, and C. M. Allred, 1976. Measuring and minimizing diode detector nonlinearity. *IEEE Trans. Instrum. Meas.*, IM- 25(4), 324 pp.

Hollinger, J., Peirce, J., and Poe, G, 1990. SSM/I instrument evaluation. *IEEE Trans. Geosci. Remote Sens.* 28, 781–790.

Imaoka, K., M. Kachi, M. Kasahara, N. Ito, K. Nakagawa, and T. Oki, 2010. Instrument Performance and calibration of AMSR-E and AMSR2. *International Archives of the Photogrammetry, Remote Sensing and Spatial Information Science,* XXXVIII, 13-16.

Isaaks, E., and Srivastava, M.. 1989. An introduction to Applied Geostatistics. Oxford University Press. 592p.

Ishimaru, 1978. Wave Propagation and Scattering in Random Media. New York: Academic, vols. I/II.

Jiang, L. J. Shi, S. Tjuatja, J. Dozier, K. Chen, and L. Zhan, 2007. A parameterized multiple-scattering model for microwave emission from dry snow. *Remote Sens. Environ.*, 111, 357–366.

Jonas, T., C. Marty, and J. Magnusson, 2009. Estimating the snow water equivalent from snow depth measurements in the Swiss Alps. *J. Hydrol.*, 378, 161–167.

Joseph, J. H., W. J. Wiscombe, and J. A. Weinman, 1976. The delta-Eddington approximation for radiative flux transfer. *J. Atmos. Sci.,* 33, 2452–2459.

Kainulainen, J., J. Lemmetyinen, K. Rautiainen, A. Colliander, J. Uusitalo, and J. Lahtinen, 2009. Error propagation in calibration networks of synthetic aperture radiometers. *IEEE Trans. Geosci. Remote Sens.*, 47(9), 3140-3150.

Kaleschke, L., X. Tian-Kunze, N. Maaß, M. Mäkynen, and M. Drusch, 2012. Sea ice thickness retrieval from SMOS brightness temperatures during the Arctic freeze-up period. *Geophys. Res. Lett.*, 39, L05501, DOI: 10.1029/2012GL050916.

Kelly, R., A. Chang, L.Tsang, and J. Foster, 2003. A prototype AMSR-E global snow area and snow depth algorithm *IEEE T. Geosci. Remote Sens.*, 41(2), 230-242.

Kerr, Y.H., Waldteufel, P., Wigneron, J.-P., Delwart, S., Cabot, F., Boutin, J., Escorihuela, M.-J., Font, J., Reul, N., Gruhier, C., Juglea, S.E., Drinkwater, M.R., Hahne, A., Martín-Neira, M., Mecklenburg, S., 2010. The SMOS mission: new tool for monitoring key elements of the global water cycle. *Proc. IEEE*, 98(5), 666-687.

Knowles, K. W., M. H. Savoie, R. L. Armstrong, and M. J. Brodzik, 2006. AMSR-E/aqua daily EASE-grid brightness temperatures, 2005–2008. Boulder, Colorado USA: National Snow and Ice Data Center Digital media (updated 2010).

Kontu, A., S. Kemppainen, J. Lemmetyinen, J. Pulliainen, and M. Hallikainen, 2008. Determination of snow emission on lake ice from airborne passive microwave measurements. Geoscience and remote sensing symposium, 2008, IGARSS 2008. IEEE International, 4. (pp. 1046–1049) 4, Paper.

Kruopis, N., J. Praks, A. Arslan, H. Alasalmi, J. Koskinen and M. Hallikainen, 1999. Passive microwave measurements of snow-covered forests in EMAC'95. *IEEE Trans. Geosci. Remote Sensing,* 37, 2699-2705.

Kurvonen, L., and M. Hallikainen, 1997. Influence of land-cover category on brightness temperature of snow. *IEEE Trans. Geosci. Remote Sens.*, 35(2), 367-377.

Künzi, K. F., S. Patil, and H. Rott, 1982. Snow-cover parameters retrieved from Nimbus-7 Scanning Multichannel Microwave Radiometer (SMMR) data. *IEEE Trans. Geosci. Remote Sens.*, GE-20, 452-467.

Lahtinen, J., J. Pihlflyckt, I. Mononen, S. Tauriainen, M. Kemppinen, and M. Hallikainen, 2003. Fully polarimetric microwave radiometer for remote sensing. *IEEE Trans. Geosci. Rem. Sens.*, 41 (8), 1869-1878.

Lahtinen, J., M. Hallikainen, 2003. HUT fully polarimetric calibration standard for microwave radiometry. *IEEE Trans. Geosci. Rem. Sens.*, 41 (3), 603-611.

Lemke, P., J. Ren, R. B. Alley, I. Allison, J. Carrasco, G. Flato, G., *et al.*, 2007. Observations:Changes in snow, ice and frozen ground. In S. Solomon, D. Qin, M. Manning, Z. Chen, M. Marquis, K. B. Averyt, M. Tignor, & H. L. Miller (Eds.), Climate change 2007: The physical science basis. Contribution of working group I to the fourth assessment report of the intergovernmental panel on climate change. Cambridge, United Kingdom and New York, NY, USA: Cambridge University Press.

Lemmetyinen, J., J. Pulliainen, A. Rees, A. Kontu, Y. Qiu, and C. Derksen, 2010. Multiple layer adaptation of the HUT snow emission model: comparison with experimental data. *IEEE Trans. Geosci. Remote Sens.,* 48, 2781-2794.

Macelloni, G., S. Paloscia, P. Pampaloni, M. Brogioni, R. Ranzi, and A. Crepaz, 2005. Monitoring of melting refreezing cycles of snow with microwave radiometers: The Microwave Alpine Snow Melting Experiment (MASMEx 2002-2003). *IEEE Trans. Geosci. Remote Sens.*, 43(11), 2431-2442.

Machin, K. E., M. Ryle, and D. D. Vonberg, 1952. The design of equipment for measuring small radio-frequency noise powers, *Proc. IEE*, 99, 127-134.

Martín-Neira M., M. Suess, J. Kainulainen, F. Martín-Porqueras, 2008. The Flat Target Transformation. *IEEE Trans. Geosci. Remote Sens.*, 46(3), 613-620.

Maxwell, J. C., 1865. A dynamical theory of the electromagnetic field. *Philosophical Transactions of the Royal Society of London* 155, 459-512.

McMullan, K.D., K.A. Brown, M. Martin-Neira, W. Rits, S. Ekholm, J. Marti, and J. Lemanczyk, 2008. SMOS: The payload. *IEEE Trans. Geosci. Remote Sens.,* 46(3) 594-605.

Mills P., and G. Heygster, 2010. Retrieving sea ice concentration from SMOS. *IEEE Trans. Geosci. Remote Sens.,* 8 (2), 283-287.

Mognard, N., and E. Josberger, 2002. Seasonal evolution of snowpack parameters, northern Great Plains. *Ann. Glaciol.*, 34, 15-23.

Moreno-Galbis, P. J. Kainulainen, M. Martin-Neira, 2007. Experimental demonstration of the Corbella equation for aperture synthesis microwave radiometry. *IEEE Trans. Geosci. Remote Sens.*, 45 (4), 945-957.

Mätzler, C., 1987. Applications of the interaction of microwaves with the natural snow cover. *Remote Sens. Rev.,* 2, 259–387.

Mätzler, C., 1994. Passive microwave signatures of landscapes in winter. *Meteorol. Atmos. Phys.,* 54(1–4), 241–260.

Mätzler, C., E. Schanda, and W. Good, 1982. Towards the definition of optimum sensor specifications for microwave remote sensing of snow. *IEEE Trans. Geosci. Remote Sens.*, GE-20, 57-66.

Njoku, E.G., T.J. Jackson, V. Lakshmi, T.K. Chan, S.V. Nghiem, 2003. Soil moisture retrieval from AMSR-E. *IEEE Trans. Geosci. Remote Sens.*, 41(2), 215- 229.

Njoku, E.G and J. A. Kong, 1977. Theory for passive microwave sensing of near-surface soil moisture. *J. Geophys. Res.,* 82, 3108-3118.

Oliva, R., M. Martin-Neira, I. Corbella, F. Torres, J. Kainulainen, J. E. Tenerelli, F. Cabot, F. Martin-Porqueras, 2012 (in press). SMOS calibration and instrument performance after one year in orbit. *IEEE Trans. Geosci. Remote Sens.*

Orhaug, T., and W. Waltman, 1962. A switched load radiometer. *Publ. Natl. Radio Astron. Obs.*, 1, 179-204.

Piironen, P., 2002. PMS offset determination using an IF attenuator. ESA/ESTEC, Holland, The Netherlands, Tech. Note 14629/00/NL/SF.

Planck, M., 1901. On the law of distribution of energy in the normal spectrum. *Annalen der Physik*, 4, 553 ff.

Pulliainen, J., 2006. Mapping of snow water equivalent and snow depth in boreal and sub-arctic zones by assimilating space-borne microwave radiometer data and ground-based observations. *Remote Sens. Environ.*, 101, 257-269.

Pulliainen, J., and M. T. Hallikainen, 2001. Retrieval of regional snow water equivalent from space-borne passive microwave observations. *Remote Sens. Environ.*, 75, 76–85.

Pulliainen, J., J. Grandell, and M. T. Hallikainen, 1999. HUT snow emission model and its applicability to snow water equivalent retrieval. *IEEE Trans. Geosci. Remote Sens.,* 37, 1378–1390.

Rango, A., Chang, A. T. C., and Foster, J. L., 1979. The utilisation of space-borne microwave radiometers for monitoring snowpack properties. *Nord. Hydrol.,* 10, 25–40.

Rautiainen K, J. Lemmetyinen, J. Pulliainen, J. Vehviläinen, M. Drusch, A. Kontu, J. Kainulainen, and J. Seppänen, 2011. L-Band radiometer observations of soil processes in boreal and subarctic environments *IEEE Trans. Geosci. Remote Sens.*, DOI: 10.1109/TGRS.2011.2167755

Rautiainen, K., J. Kainulainen, T. Auer, J. Pihlflyckt, J. Kettunen, and M. Hallikainen, 2008. Helsinki University of Technology L-band airborne synthetic aperture radiometer. *IEEE Trans. Geosci. Remote Sens.*, 46, 717-726.

Rees, A., J. Lemmetyinen, C. Derksen, J. Pulliainen, and M. English. 2010. Observed and modelled effects of ice lens formation on passive microwave estimates of snow water equivalent. *Remote Sens. Environ.*, 114, 116-126.

Reul, N., S. Saux-Picart, B. Chapron, D. Vandemark, J. Tournadre, and J. Salisbury, 2009. Demonstration of ocean surface salinity microwave measurements from space using AMSR-E data over the Amazon plume. *Geophys. Res. Lett.,* 36, L13607.

Robinson, D.A., F.T. Keimig, and K.F. Dewey, 1993. Recent variations in Northern Hemisphere snow cover. In: *Proc. Fifteenth Annual Climate Diagnostics Workshop*. NOAA, 219-224.

Rott, H., C. Duguay, R. Essery, C. Haas, G. Macelloni, E. Malnes, *et al.*, 2009. ESA SP-1313/3 candidate Earth Explorer Core missions report for assessment: CoReH2o — Cold regions hydrology high resolution observatory. ESA Communication Production Office (pp. 114).

Roy, V., K. Goita, A. Royer, A. Walker, and B. Goodison, 2004. Snow water equivalent retrieval in a Canadian boreal environment from microwave measurements using the HUT snow emission model. *IEEE Trans. Geosci. Remote Sens.*, 42(9) 1850–1859.

Ruf, C. S., C. T. Swift, A. B. Tanner, and D. M. Le Vine, 1988. Interferometric synthetic aperture microwave radiometry for remote sensing of the Earth. *IEEE Trans. Geosci. Remote Sens.*, 26(5), 597–611.

Schwank M., A. Wiesmann, C. Werner, C. Mätzler, D. Weber, A. Murk, I. Völksch, U. Wegmüller, 2010. ELBARA II, an L-band radiometer system for soil moisture research. *Sensors*, 10(1), 584-612.

Schwank, M., M. Stähli, H. Wydler, J. Leuenberger, C. Mätzler, H. Flühler. 2004. Microwave L-band emission of freezing soil. *IEEE Trans. Geosci. Remote Sens.*, 42(6), 1252-1261.

Sharkov, E.A., 2009. Passive microwave remote sensing of the Earth: physical foundations. Springer.

Skogland, T., Lomeland, S. and Goksoyr, J. 1988. Respiratory burst after freezing and thawing of soil: experiments with soil bacteria. *Soil Biol. Biochem.*, 20: 851–856.

Skou, N. and D. M. Le Vine, 2006. Microwave radiometer systems: design and analysis. Artech House, 2nd ed.

Smith, S., and J. Brown, 2009. Permafrost. Permafrost and seasonally frozen ground. Assessment of the status of the development of standards for the terrestrial essential climate variables. *Global Terrestrial Observing System*, 22 pp., version 13, 8 May 2009, Rome, 2009.

Sobjaerg, S., N., Skou, J. E. Balling, 2009. Measurements of active cold loads for radiometer calibration. *IEEE Trans. Geosci. Rem. Sens.*, 47 (9), 3134-3139.

Solheim, F., J. Godwin, E.R. Westwater, Y. Han, S. Keihm, K. Marsh, and R.Ware, 1998. Radiometric profiling of temperature, water vapor and cloud liquid water using various inversion methods. *Radio Sci.*, 33, 393-404.

Spreen, G., L. Kaleschke and G. Heygster, 2008. Sea ice remote sensing using AMSR-E 89 GHz channels. *J. Geophys. Res.*, 113, C02S03, doi:10.1029/2005JC003384.

Strogyn, A., 1986. A study of the microwave brightness temperature of snow from the point of view of strong fluctuation theory. *IEEE Trans. Geosci. Remote Sens.,* GE-24, 220-231.

Sturm, M. and C. S. Benson, 2004. Scales of spatial heterogeneity for perennial and seasonal snow layers. *Ann. Glaciol.,* 38, 253-260.

Sturm, M., J. Holmgren, and G. Liston, 1995. A seasonal snow cover classification system for local to global applications. *J. Climate,* 8, 1261–1283.

Sun, S., J. Jin, and Y. Xue, 1999. A simple snow-atmosphere-soil transfer model. *J. Geophys. Res.,* 104(D16), 19 587–19 597.

Swift, C. T. and R.E. McIntosh, 1983. Considerations for microwave remote sensing of ocean-surface salinity. *IEEE Trans. Geosci. Remote Sens.,* GE-21(4), 480-491.

Tait, A. 1998. Estimation of snow water equivalent using passive microwave radiation data, *Remote Sens. Environ. 64*, 286–291.

Takala M, K. Luojus, J. Pulliainen, C. Derksen, J. Lemmetyinen, J-P. Kärnä, J. Koskinen, and B. Bojkov, 2011. Estimating northern hemisphere snow water equivalent for climate research through assimilation of space-borne radiometer data and ground-based measurements. *Remote Sens. Environ.,* 115(12), 3517-3529.

Takala, M., J. Pulliainen, S. Metsämäki, and J. Koskinen, 2009. Detection of snowmelt using spaceborne microwave radiometer data in Eurasia from 1979 to 2007. *IEEE Trans. Geosci. Remote Sens.,* 47(9), 2996-3007.

Tedesco, M. and E. J. Kim. 2006b. Intercomparison of electromagnetic models for passive microwave remote sensing of snow. *IEEE Trans. Geosci. Remote Sens.,* 44(10), 2654–2666.

Tedesco, M., and J. R. Wang, 2006a. Atmospheric correction of AMSR-E brightness temperatures for dry snow cover mapping. *IEEE Geosci. Remote Sens. Lett.,* 3(3), 320–324.

Tiuri, M., and M. Hallikainen, 1981. Remote sensing of snow depth by passive microwave satellite observations. *Proceedings of the 11th European Microwave Conference,* Amsterdam, September 1981, 233-238.

Tsang, L. J. Pan, D. Liang, Z. Li, D. Cline, and Y. Tan, 2007. Modeling active microwave remote sensing of snow using dense media radiative transfer (DMRT) theory with multiple-scattering effects. *IEEE Trans. Geosci. Remote Sens*., 45(4), 990-1004.

Tsang, L., C.-T. Chen, A. T. C. Chang, J. Guo, and K.-H. Ding, 2000. Dense media radiative transfer theory based on quasi-crystalline approximation with applications to microwave remote sensing of snow. *Radio Sci*., 35(3), 731 - 749.

Tsang, L., J. A. Kong, and R. T. Shin, 1985. Theory of Microwave Remote Sensing. New York: Wiley.

Ulaby, F. T., R. K. Moore, and A.K. Fung, Microwave Remote Sensing: Active and Passive, Volume II - Radar Remote Sensing and Surface Scattering and Emission Theory. Addison- Wesley Publishing Company, 609 p.

Ulaby, F.T., Moore, R. K., Fung, A. K., 1981. Microwave Remote Sensing: Active and Passive, Volume I, Fundamentals and Radiometry. Addison-Wesley Publishing Company, 456 p.

Wegmüller, U., and C. Mätzler, 1999. Rough bare soil reflectivity model. *IEEE Trans. Geosci. Remote Sens.*, 37, 1391–1395.

Weise, T., 1996. Radiometric and structural measurements of snow. Ph.D. dissertation, Inst. Appl. Phys., Univ. of Bern, Switzerland.

Wiesmann, A., and C. Mätzler, 1999. Microwave emission model of layered snowpacks. *Remote Sens. Environ.*, 70(3) 307 - 316.

Wiesmann, A., C. Mätzler, and T. Weise, 1998. Radiometric and structural measurements of snow samples. *Radio Sci.*, 33(2), 273-289.

Willis, W.O., C.W. Carlson, J. Alessi, and H.J. Hass, 1961. Depth of freezing and spring runoff as related to fall soilmoisture level. *Soil Sci. Society of America J.*, 41, 115-123.

Ye, H., H. R. Cho, and P. E. Gustafson, 1998. The changes in Russian winter snow accumulation during 1936– 83 and its spatial patterns. *J. Clim.,* 11(5), 856 - 863.

Zhang, T. and R. L. Armstrong, 2001. Soil freeze/thaw cycles over snow-free land detected by passive microwave remote sensing. *Geophys. Res.Lett.*, (28)5, 763 - 766.

Zhang, T., 2005. Influence of the seasonal snow cover on the ground thermal regime: An overview. *Rev. Geophys.*, 43, RG4002, doi:10.1029/ 2004RG000157.

Zhang, T., R. G. Barry, K. Knowles, F. Ling and R.L. Armstrong, 2003. Distribution of seasonally and perennially frozen ground in the Northern Hemisphere. In: Proceedings of the 8th International Conference on Permafrost, 21-25 July 2003, Zurich, Switzerland [Phillips, M., S.M. Springman, and L.U. Arenson (eds.)].A.A. Balkema, Lisse, the Netherlands, 1289 - 1294.

Zhang, T., R. G. Barry, K. Knowles, J. A. Heginbottom and J. Brown, 1999. Statistics and characteristics of permafrost and ground-ice distribution in the Northern Hemisphere. *Polar Geogr.,* 23(2), 132 - 154.

Summary of appended papers

[P1]

The study compares microwave signatures of snow covered terrain in the boreal forest regions of Finland and Northern Canada. The study makes use of an extensive dataset of airborne microwave radiometer observations in the two regions, comparing these with *in situ* measurements of snow properties. The main goals of the study were to (1) compare snowpack physical properties in the boreal forest zones of Finland and Canada (2) Indentify the influence of land cover and vegetation effects on the microwave signature ion the two regions (3) asses the quality of a forward emission model in detecting these variations. The study underlines the effects of diverse land cover on the microwave signature, specifically the differing signatures from snow covered lake ice and other wetlands when compared to surrounding dry terrain.

[P2]

This paper describes a modification to an existing snow emission model, accounting for the influence of multiple horizontal layers of snow, each with differing dielectric properties. The study presents the theoretical background of the model, and analyses the influence of snow layering through simulation. Available experimental datasets are then applied to test the model performance, comparing also to the original model configuration simulating the snowpack as a homogeneous single layer. The study shows forward modeling results can be improved by applying the layered model, in particular in the case of clear dielectric contrasts in the snowpack, such as ice lenses. The developed model also allows the simulation of e.g. snow covered lake ice, which is applied in [P3].

[P3]

The paper presents an analysis of simulations performed using the modified emission model developed in [P2], compared to airborne observations over frozen lakes in Canada. The model simulations are supported by extensive *in situ* information on lake ice properties; reference observational data are available over a range of frequencies. The effect of different *a priori* assumptions of lake ice and snow properties on modeling accuracy is analyzed. The study shows that microwave emission from lake ice can be simulated with reasonable accuracy using the applied forward model; however some discrepancies in the lower frequency spectrum are noted.

[P4]

The study presents a technique to mitigate for the influence of snow covered lakes in snow parameter retrieval applications relying on passive microwave observations. The effect of lakes and other wetlands on the microwave signature was noted in [P1], and the forward model allowing the simulation of these was developed in [P2]. The paper first presents a forward modeling experiment, where available *in situ* information on snow, land cover and lake ice properties are used to simulate whole sceneries as observed from a space-borne radiometer. Two model configurations are compared, first in the default configuration of ignoring the differing emission from lakes, and secondly by introducing lakes in the simulation. Next, an inversion technique to retrieve snow information from satellite observations is applied using the same forward model configurations. The improvement of estimate accuracy is analyzed using independent reference data on snow properties.

[P5]

The study concerns the monitoring of soil freeze/thaw processes using microwave radiometry. The brightness temperature signatures of soil processes are analyzed by applying a season-long experimental dataset of L-band radiometer observations and related reference *in situ* information on soil and snow cover properties. A simple emission model to predict the effect of progress of soil freezing on the detected emission is presented, and the model estimates are compared to observations. The experimental dataset is also compared to available airborne L-band passive microwave data from the region, as well as the first available data from the SMOS satellite.

[P6]

This paper presents the design, testing and performance analysis of a distributed calibration network system for the Soil Moisture and Ocean Salinity (SMOS) satellite mission, launched in 2009. The purpose of the network was to provide an accurate calibration reference signal for the different receivers of the SMOS payload, the MIRAS (Microwave Imaging Radiometer using Aperture Synthesis) instrument. In the paper, the operating principle and design of the network are presented. The paper describes characterization tests performed on the system, as well as analyses the effect of characterization inaccuracies on the final performance of the MIRAS instrument.

Cover: aerial photograph of a frozen lake in Saariselkä, Inari. T. Casal, ESA, 2011.

Aalto-DD 142/2012

ISBN 978-952-60-4843-7
ISBN 978-952-60-4844-4 (pdf)
ISSN-L 1799-4934
ISSN 1799-4934
ISSN 1799-4942 (pdf)

Aalto University
School of Electrical Engineering
Department of Radio Science and Engineering
www.aalto.fi

BUSINESS +
ECONOMY

ART +
DESIGN +
ARCHITECTURE

SCIENCE +
TECHNOLOGY

CROSSOVER

DOCTORAL
DISSERTATIONS